2007-09

Characterization, optimization, and test of the NPSATI MEMS 3-axis sensor suite for use in small satellite attitude control

Pugsley, Thomas S.

Monterey, California. Naval Postgraduate School

NAVAL POSTGRADUATE SCHOOL

MONTEREY, CALIFORNIA

THESIS

CHARACTERIZATION, OPTIMIZATION, AND TEST OF THE NPSAT1 MEMS 3-AXIS RATE SENSOR SUITE FOR USE IN SMALL SATELLITE ATTITUDE CONTROL

by

Thomas S. Pugsley

September 2007

Thesis Advisor:	James H. Newman
Second Reader:	Daniel J. Sakoda

THIS PAGE INTENTIONALLY LEFT BLANK

REPORT DOCUMENTATION PAGE		Form Approved OMB No. 0704-0188

1. AGENCY USE ONLY *(Leave blank)*	2. REPORT DATE	3. REPORT TYPE AND DATES COVERED
	September 2007	Master's Thesis

4. TITLE AND SUBTITLE: Characterization, Optimization, and Test of the NPSAT1 MEMS 3-Axis Rate Sensor Suite for use in Small Satellite Attitude Control.	5. FUNDING NUMBERS
6. AUTHOR(S) Thomas S. Pugsley	
7. PERFORMING ORGANIZATION NAME(S) AND ADDRESS(ES) Naval Postgraduate School Monterey, CA 93943-5000	8. PERFORMING ORGANIZATION REPORT NUMBER
9. SPONSORING /MONITORING AGENCY NAME(S) AND ADDRESS(ES) N/A	10. SPONSORING/MONITORING AGENCY REPORT NUMBER

11. SUPPLEMENTARY NOTES The views expressed in this thesis are those of the author and do not reflect the official policy or position of the Department of Defense or the U.S. Government.

12a. DISTRIBUTION / AVAILABILITY STATEMENT	12b. DISTRIBUTION CODE
Approved for public release; distribution is unlimited.	

13. ABSTRACT (maximum 200 words)

The NPSAT1 project is a Naval Postgraduate School (NPS) educational small satellite combining student education in satellite systems and operations, institutional research, and sponsored experiments with the objective of testing technologies for applications in space flight. The micro-electro-mechanical system (MEMS) rate sensor is one of these experimental technologies. Packaging three of these MEMS sensors together makes a 3-axis rate sensor suite. The MEMS experiment was originally conceived of as a low-cost, low-mass augmentation to the magnetometer for use by the Attitude Control System (ACS). The experiment is to test the sensor suite's ability to measure NPSAT1 rates, comparing these rates to those determined by using a magnetometer and GPS. Operationally, the goal is to perform a space-flight demonstration of the MEMS sensor.

This thesis includes two phases of research and development. First, the MEMS 3-axis rate sensor suite is fully tested and characterized. Experimental testing proves the sensor suite's effectiveness as a low-cost, low-mass augmentation to the magnetometer for satellite rate determination, as well as its ability to measure very low rates. Second, we adapt the original design and operations to maximize the accuracy and utility of the sensor suite. Finally, a complete flight-like subsystem is built and tested.

.

14. SUBJECT TERMS MEMS, 3-Axis Rate Sensor, Rate Sensor, Attitude Control, Spacecraft, Micro-electromechanical, NPSAT1, low rate, ACS Subsystem.	15. NUMBER OF PAGES 227
	16. PRICE CODE

17. SECURITY CLASSIFICATION OF REPORT	18. SECURITY CLASSIFICATION OF THIS PAGE	19. SECURITY CLASSIFICATION OF ABSTRACT	20. LIMITATION OF ABSTRACT
Unclassified	Unclassified	Unclassified	UU

NSN 7540-01-280-5500

Standard Form 298 (Rev. 2-89)
Prescribed by ANSI Std. 239-18

THIS PAGE INTENTIONALLY LEFT BLANK

Approved for public release; distribution is unlimited.

CHARACTERIZATION, OPTIMIZATION, AND TEST OF THE NPSAT1 MEMS 3-AXIS RATE SENSOR SUITE FOR USE IN SMALL SATELLITE ATTITUDE CONTROL

Thomas S. Pugsley
Major, United States Army
B.S., Illinois Institute of Technology, 1997
M.B.A, Touro University International, 2004

Submitted in partial fulfillment of the
requirements for the degree of

MASTER OF SCIENCE IN SPACE SYSTEMS OPERATIONS

from the

NAVAL POSTGRADUATE SCHOOL
September 2007

Author: Thomas S. Pugsley

Approved by: Dr. James H. Newman
Thesis Advisor

Daniel J. Sakoda
Second Reader

Dr. Rudolf Panholzer
Chairman, Space Systems Academic Group

THIS PAGE INTENTIONALLY LEFT BLANK

ABSTRACT

The NPSAT1 project is a Naval Postgraduate School (NPS) educational small satellite combining student education in satellite systems and operations, institutional research, and sponsored experiments with the objective of testing technologies for applications in space flight. The micro-electro-mechanical system (MEMS) rate sensor is one of these experimental technologies. Packaging three of these MEMS sensors together makes a 3-axis rate sensor suite. The MEMS experiment was originally conceived of as a low-cost, low-mass augmentation to the magnetometer for use by the Attitude Control System (ACS). The experiment is to test the sensor suite's ability to measure NPSAT1 rates, comparing these rates to those determined by using a magnetometer and GPS. Operationally, the goal is to perform a space-flight demonstration of the MEMS sensor.

This thesis includes two phases of research and development. First, the MEMS 3-axis rate sensor suite is fully tested and characterized. Experimental testing proves the sensor suite's effectiveness as a low-cost, low-mass augmentation to the magnetometer for satellite rate determination, as well as its ability to measure very low rates. Second, we adapt the original design and operations to maximize the accuracy and utility of the sensor suite. Finally, a complete flight-like subsystem is built and tested.

THIS PAGE INTENTIONALLY LEFT BLANK

TABLE OF CONTENTS

LIST OF FIGURES

LIST OF TABLES

THIS PAGE INTENTIONALLY LEFT BLANK

GLOSSARY OF TERMS

ACS	Attitude Control System
ADC	Analog to Digital Converter
AOCS	Attitude and Orbital Control System
BIT	Built In Test
C&DH	Command and Data Handler
CERTO	Coherent Electromagnetic Radio Beacon Tomography
CFTP	Configurable Fault –Tolerant Processor
COBRAS	Cosmic Background Radiaion Anisotropy Satellite
COTS	Comercial Off-the-Shelf
EDU	Experimental Development Unit
EELV	Expendable Launch Vehicle
EPS	Electrical Power System
ESA	European Space Agency
ESPA	EELV Secondary Payload Adapter
EVA	External Vehicular Activity
FIRST	Far Infrared and Sub-millimeter Telescope
FFT	Fast Fourier Transform
FPGA	Field Programmable Gate Array
IC	Intigrating Contractors
ITAR	International Traffic in Arms Regulations
ITJ	Improved Triple Junction
LDO	Low Drop Out
LEO	Low Earth Orbit
MEMS	Micro-electrical-mechanical
MPE	Maximum Predicted Environment
NPS	Naval Postgraduate School
NPSAT1	NPS Spacecraft Architecture and Technology Demonstration Satellite
NRL PPD	Naval Research Laboratories Plasma Physics Division
PCFB	Power Control and Filter Board
PRCB	Power Regulation and Control Board
RMU	Rate Measurment Unit
SAFER	Simplified Aid for EVA Rescue System
SDI	BEI Systron Donner Innertial
SKLPBF	Sallen Key Low Pass Butterworth Filter
SMS	Solar Cell Measurment System
SSTL	Surrey Satellite Technology Ltd.
STP	Department of Defense Space Test Program
SSAG	Space Systems Academic Group
TRT	HAAS 2-axis Tilt and Rotational Table
TVC	Thermal Vacuum Chamber
UPS	Uninteruptable Power Supply
VISM	Visible Wavelength Imager

THIS PAGE INTENTIONALLY LEFT BLANK

ACKNOWLEDGMENTS

I would like to thank my thesis advisor, Dr. Jim Newman, for his guidance, his continual mentorship, and his love of science. Many of the long days were made brighter by his continual optimism and excitement for the unknown. I would also like to thank the rest of the Space Systems Academic Group, specifically Dan Sakoda, Jim Horning, Ron Phelps, and David Rigmaiden. Without all your help and support I would have progressed endlessly without direction. There is no measure for how much I owe you all, so I will simply say thanks. Thank you for making my work here exciting and fruitful, it has been an honor to work with you all. I would also like to acknowledge the work of my predecessors, CJ Didier, Paul Overstreet, Elizabeth Okano, M. Gruhlke, your hard work laid the foundation from which I was able to build. Thanks.

THIS PAGE INTENTIONALLY LEFT BLANK

I. INTRODUCTION

A. BACKGROUND

The most modern and technologically advanced spacecraft currently under construction will launch with technologies two to three generations old. The research and development life cycle for space flight hardware is simply too slow and expensive to be able to rapidly integrate new technologies. Coupled with the risk adverse requirements levied by insurers and financiers, this process is made even slower. Thus, for many commercial and governmental spacecraft the risk is simply too great to allow the integration of previously unflown technology into spacecraft designs. This induces a very long lead time from technological development to the actual space flight implementation of new technologies. Launching a spacecraft for the sole purpose of testing new technologies is typically not feasible for most commercial and governmental agencies due to cost and risk. Operating under tight financial restrictions can often limit the amount of non-flight critical testing an organization can do, and though optimization of systems is preferred, it is often waived for overall cost savings. So how do new technologies ever get tested and qualified for space flight? For many companies and governmental organizations, this can be accomplished through collaboration with and sponsorship of university research.

Universities can provide commercial and governmental organizations a very low cost alternative to their own space flight testing. University research is often subsidized through numerous governmental programs as well as through other commercial and governmental sponsorships. This spreads the overall cost of the research out over numerous organizations and universities, depending on their involvement level. In addition to the obvious cost savings, university sponsorship offers other incentives as well. Mainly, a university is a huge concentration of academic professionals, with experts in almost every technological field available. Universities also provide eager young students at all levels to the project, supplying fresh and innovative ideas. Sponsoring organizations will get access to these pools of resources for "pennies on the dollar". Though university research programs and space flight demonstration

experiments typically operate on longer time lines than commercial or private sector programs, they are far less expensive, making university spacecraft potential platforms for space qualifying new technology.

B. NPSAT1

The NPS Spacecraft Architecture and Technology Demonstration Satellite (NPSAT1) project is at this writing, the culmination of over seven years of institutional research and sponsored experiments with the purpose of testing new technologies for applications in space flight. It is also meant to educate officer students on full life cycle design, development, testing, integration, and operations of space systems. The project is a joint venture between the Naval Postgraduate School (NPS), the National Reconnaissance Office (NRO), the DoD Space Test Program (STP), and numerous other sponsoring agencies. The spacecraft itself is a low-cost architecture and technology demonstration satellite, housing a number of technology demonstrations and sponsored experiments, all varying in purpose across a wide range of technologies [1]. An expanded view of the NPSAT1 spacecraft can be seen below in Figure 1, as well as the respective experiment locations.

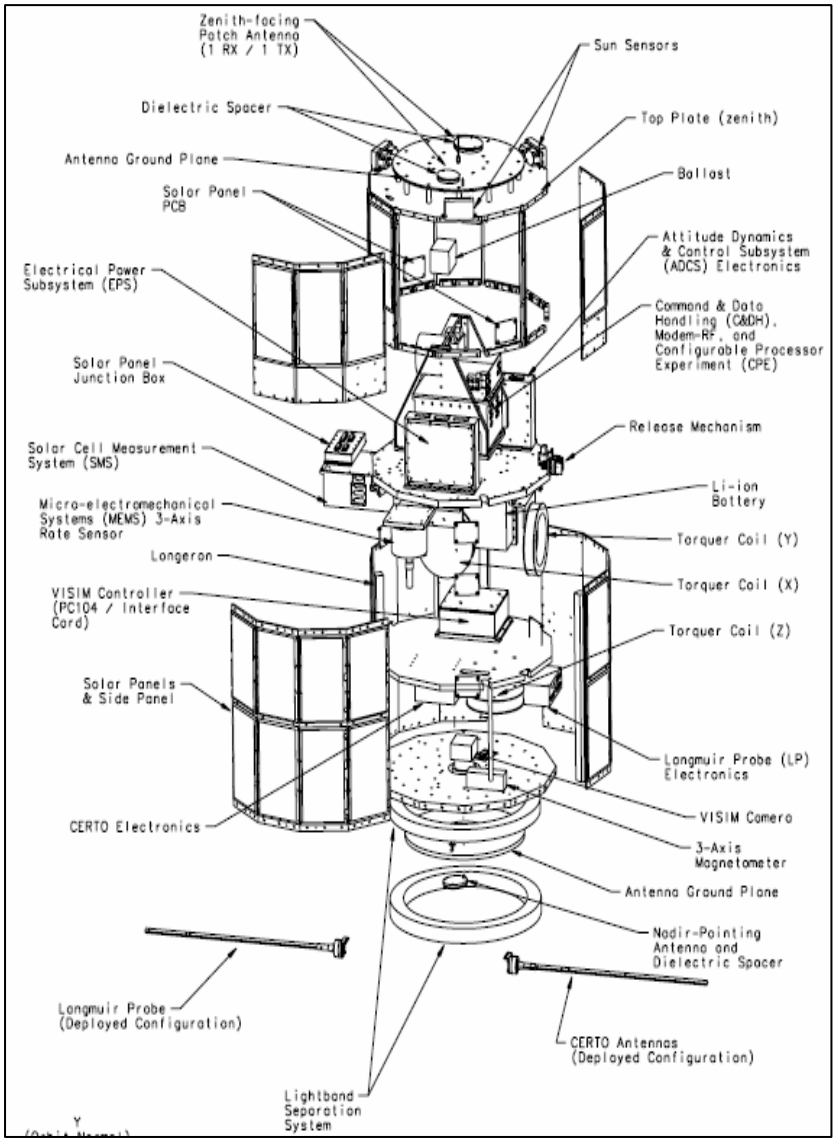

Figure 1. Expanded view of the NPSAT1 Spacecraft.

NPSAT1 is a 12-sided spacecraft, weighing approximately 82 kg (180 lbs), with a stowed length of approximately 86 cm (34 inches), and a stowed width of approximately 61 cm (24 inches) [1]. The spacecraft was designed to be a 3-axis stabilized, nadir pointing spacecraft, using a 3-axis magnetometer and three torquer coils for stabilization. The spacecraft's Lithium-Ion battery has a battery capacity of 225 Whrs, and provides the bus with a full charge voltage of 29.4 Volts. This power is generated using thirty-six solar panels, placed uniformly on three solar panel rings around the exterior circumference of the spacecraft. Twenty-four of these panels are commercial-off-the-

shelf (COTS) triple junction cells, while the remaining twelve panels use experimental triple-junction cells. Altogether, these cells are expected to generate 45 W of peak power during sunlight.

Due to its roots as an educational tool for graduate students, as well as a technology demonstration satellite for the university and its sponsoring organizations, NPSAT1 has a much higher level of risk than most other types of spacecraft. Because of this, the spacecraft is classified as a Class D spacecraft from the NPR 8705.4 Appendix A, seen below in Table 1, and is considered to be a low-priority, high-risk spacecraft [1, 2]. This is typical for most university and private research satellites. While the risk of such spacecraft may indeed be high, the advantages they bring may well be worth the risks for many organizations that are looking to get their newest technologies space-flight-demonstrated at a minimum cost, even with such a high risk. This is where the university spacecraft can play a vital role, providing higher risk test platforms at a premium price. Although NPS is a military university, there is still competition for financial resources, and sponsoring organizations still fund the majority of research and experiments.

Characterization	Class A	Class B	Class C	Class D
Priority (Criticality to Agency Strategic Plan) and Acceptable Risk Level	High priority, very low (minimized) risk	High priority, low risk	Medium priority, medium risk	Low priority, high risk
National significance	Very high	High	Medium	Low to medium
Complexity	Very high to high	High to medium	Medium to low	Medium to low
Mission Lifetime (Primary Baseline Mission)	Long, >5years	Medium, 2-5 years	Short, <2 years	Short < 2 years
Cost	High	High to medium	Medium to low	Low
Launch Constraints	Critical	Medium	Few	Few to none
In-Flight Maintenance	N/A	Not feasible or difficult	Maybe feasible	May be feasible and planned
Alternative Research Opportunities or Re-flight Opportunities	No alternative or re-flight opportunities	Few or no alternative or re-flight opportunities	Some or few alternative or re-flight opportunities	Significant alternative or re-flight opportunities
Achievement of Mission Success Criteria	All practical measures are taken to achieve minimum risk to mission success. The highest assurance standards are used.	Stringent assurance standards with only minor compromises in application to maintain a low risk to mission success.	Medium risk of not achieving mission success may be acceptable. Reduced assurance standards are permitted.	Medium or significant risk of not achieving mission success is permitted. Minimal assurance standards are permitted.

Table 1. Spacecraft Class Characterization (NPR 8705.4 App. A).

NPSAT1 is a fairly advanced spacecraft in terms of university research, with a broad range of internally-sponsored and externally-sponsored experimental payloads. Many experimental payloads are ideal for small university spacecraft because they are small subsystems, easily integrated into the spacecraft bus, and many of these types of experiments can be integrated into a single spacecraft. NPSAT1's payloads include four technology demonstration payloads and six experimental payloads, which will each be described individually below.

1. Technology Demonstrations

When a technology has reached a high level of maturity and users and consumers alike begin to show an interest in this technology, it is often time to plan an on-orbit technology demonstration. The purpose of such demonstrations is two fold: first, to increase the overall acceptance of the technology by consumers and the space community; and second, to validate the technology for use in space flight. Risk drives many organizations to accept only previously flown technologies. Organizationally sponsored university technology demonstration satellites can be a means for achieving this end. Listed below are the four technology demonstration payloads on NPSAT1, as well as a brief overview of the technology demonstration highlights.

a. Improved Triple-Junction Solar Cells

This payload is a combination of two experiments. The first is the sponsored flight demonstration of the Improved Triple-Junction (ITJ) solar cells. The second is a Solar Cell Measurement System (SMS) experiment developed at NPS, designed to perform current-voltage measurements and produce I-V curves for the ITJ solar cells. The twelve ITJ panels are located on the center solar cell ring, located around the center of the spacecraft body. Together the two experiments will investigate the SMS experimental control hardware, as well as provide the sponsor with on-orbit cell performance of this technology [1].

b. COTS Command and Data Handling

This flight demonstration was designed to prove the ability of COTS, PC-compatible and open source technology to be used to build a low-cost, fully flight-qualified Command and Data Handler (C&DH) subsystem for use in space applications [3]. The sponsor for this flight demonstration is the NPS SSAG.

c. Ferroelectric RAM

This flight demonstration was designed to prove the ability of ferroelectic Random Access Memory (RAM) as a viable alternative to currently used RAM in space flight technologies [1]. Functionally, it will serve as a sub-component of the Electrical Power System (EPS) [4]. This will allow the spacecraft to power down without losing configurations. It also allows the spacecraft to upload new operational software to subsystems for re-configuration. The sponsor for this flight demonstration is the NPS SSAG.

d. 3-Axis Stabilization using Torquer Coils and Magnetometer

This flight demonstration was designed to prove the ability of a three-axis magnetometer and in-house (NPS) designed and fabricated torquer coils to provide the space craft with accurate 3-axis stabilization and pointing control [1]. The Attitude Control System (ACS) will use an onboard GPS to determine the spacecraft's location and perform a table lookup to obtain values for the local magnetic field vector. These values are then compared to the magnetometer readings. The ACS will use the torquer coils to try to null the error between the current attitude and the desired attitude. Simulated results yield a pointing accuracy of better than two degrees [1]. The sponsor for this flight demonstration is the NPS SSAG.

2. Experiments

Experiments and technology demonstrations are fundamentally different. While technology demonstrations are the on-orbit demonstration and verification of a new

technology, experiments seek data and may never result in new technology. NPSAT1 has six experimental payloads, which are listed below with brief descriptions.

a. Coherent Electromagnetic Radio Beacon Tomography (CERTO)

This experiment was designed to measure the total electron content (TEC) in the ionosphere in the plane of observation. It will use a three-frequency onboard beacon to transmit a signal through the ionosphere, which would then be received and interpreted at numerous ground stations to measure its phase and amplitude perturbations. The data will be used to develop and test tomographic algorithms for reconstruction of ionosphere irregularities [1]. This has possible applications in fields such as radar, communications, navigation, and surveillance. The sponsor for this experiment is the Naval Research Laboratory Plasma Physics Division (NRL PPD).

b. Langmuir Probe

This experiment was designed to augment the CERTO experiment, and give in-situ measurements of local plasma density at orbital altitudes. The data can be processed for correlation with the ground observations of the CERTO beacon [1]. The sponsor for this experiment is again the NRL PPD.

c. Configurable Fault-tolerant Processor (CFTP)

This experiment was designed to test the use of a Field Programmable Gate Array (FPGA) based processor board to implement a flexible, triple-modular redundant (TMR) computer architecture for reliable computing in space applications [1]. It uses COTS memory cards within the C&DH housing. The experiment has various applications across many fields, to include areas such as triple-modular redundant computers and compression algorithms. The sponsor for this experiment is the NPS SSAG.

d. COTS Visible Wavelength Imager (VISIM)

This experiment was designed to provide students at NPS hands-on experience in the development, testing, and integration of a flight subsystem, as well as developing the operational, control, and tasking interfaces necessary for employment. In addition to this, the experiment is to be used as the primary data generator for the CFTP experiment, and for an educational outreach for kindergarten through 12th grade students to foster interest in aerospace studies [1]. These students would provide taskings for the VISIM through an internet-based user interface. The spacecraft would then take these pictures at its nearest pass, process and down-link them, and they would be made available online. The sponsor for this experiment is the NPS SSAG.

e. Lithium-Ion Battery Experiment

This experiment is designed to evaluate the performance of lithium-ion power cells in long duration space flight, and as a proof of concept. Lithium-ion batteries have become commonplace in many types of ground-based electronics over the past few years, and have significant advantages for use in space. They are inexpensive, have a high capacity, are practical, and require no charging control at the cell level, only at the battery level [5]. This experiment will determine if these advantages can translate to space applications as well. The sponsor for this experiment is the NPS SSAG.

f. COTS Micro-electromechanical 3-axis Rate Sensor Suite

This experiment was originally designed to gain flight experience with Micro-Electro-Mechanical (MEMS) devices, as well as to augment the magnetometer based, 3-axis stabilization demonstration [4]. It could measure the rotational rates of the spacecraft, shortly after tip-off and compare them to the measurements determined by the magnetometer. It could continue to monitor rates until it was unable to measure accurately. It was originally believed that the sensor suite might have low sensitivity to rates at a stable orbit. Rates this low would consist of the satellite's own rotation around the Earth (0.066°/s), as well as the attitude control maneuvers conducted by the ACS to maintain the spacecraft's nadir pointing. These rates would be at or below orbital rate,

and thus it was believed that QRS11 would have limited usefulness in attitude stabilization for nadir pointing in LEO. The sponsor for this experiment is the NPS SSAG.

C. THE MEMS 3-AXIS RATE SENSOR SUITE EXPERIMENT

The original purpose of the MEMS experiment was simple: gain operational flight experience with MEMS components. This could be done by integrating the MEMS sensor into the ACS as a low-cost, low-mass method of measuring the performance and accuracy of the 3-axis stabilization technology demonstration experiment during the relatively high rates of the spacecraft after tip-off, planned to be up to 5°/s, but expected to be less than 1°/s [6, 7]. Early on, there was little knowledge and understanding of MEMS rate sensors other than what was known of its use in aircraft, and what was provided by the manufacturer. It was relatively small, light-weight, and low-cost, and was used widely in aircraft, but had little to no demonstrated use in space applications.

Most MEMS sensors in the year 2001 were designed to operate accurately in rate ranges from 100°/s up to rates as large as 2,500°/s, but almost none of these sensors were designed to measure rates less than a few degrees per second. This made it difficult to determine a suitable sensor for use in NPSAT1. Only specially ordered and manufactured sensors would be able to meet the initial requirements of the experiment, and even these were not optimally designed for the low-rate and low-noise environment desired. At best, such sensors were only able to measure rate ranges of ±5°/s. Even with these specially ordered, low-rate sensors, they would still be attempting to measure rates at the very lowest end of the dynamic range of the sensor, roughly 1.3% of the entire dynamic range at orbital rate. Therefore, their usefulness after tip-off was questionable.

To determine which sensor should be used in NPSAT1, Elizabeth Okano completed a thesis in 2001 entitled “Microelectromechanical Systems for Small Satellites” [8]. This thesis led to the selection of the BEI Systron Donner Inertial Division’s (SDI) QRS11 as the experimental unit for NPSAT1. Four of these sensors were purchased, three for flight and one for testing, and an entire regiment of testing was done to determine the sensors ability to perform its task. The sensors were integrated into

the spacecraft, and the MEMS assembly diagram for this subsystem can be seen below in Figure 2. Her research verified that the sensor should theoretically be able to measure rates from tip-off down to as low as 0.01°/s, but only a single test was conducted and was not very in-depth. She identified issues with uncorrelated divergence, signal reliability, accuracy, and inconsistencies in scale factor at lower rates. She recommended that follow-on research be performed, specifically with bias stability vs. temperature to try to resolve some of these issues. This seemed to confirm that the sensors usefulness at lower rates was at best questionable for the majority of the life cycle of the spacecraft.

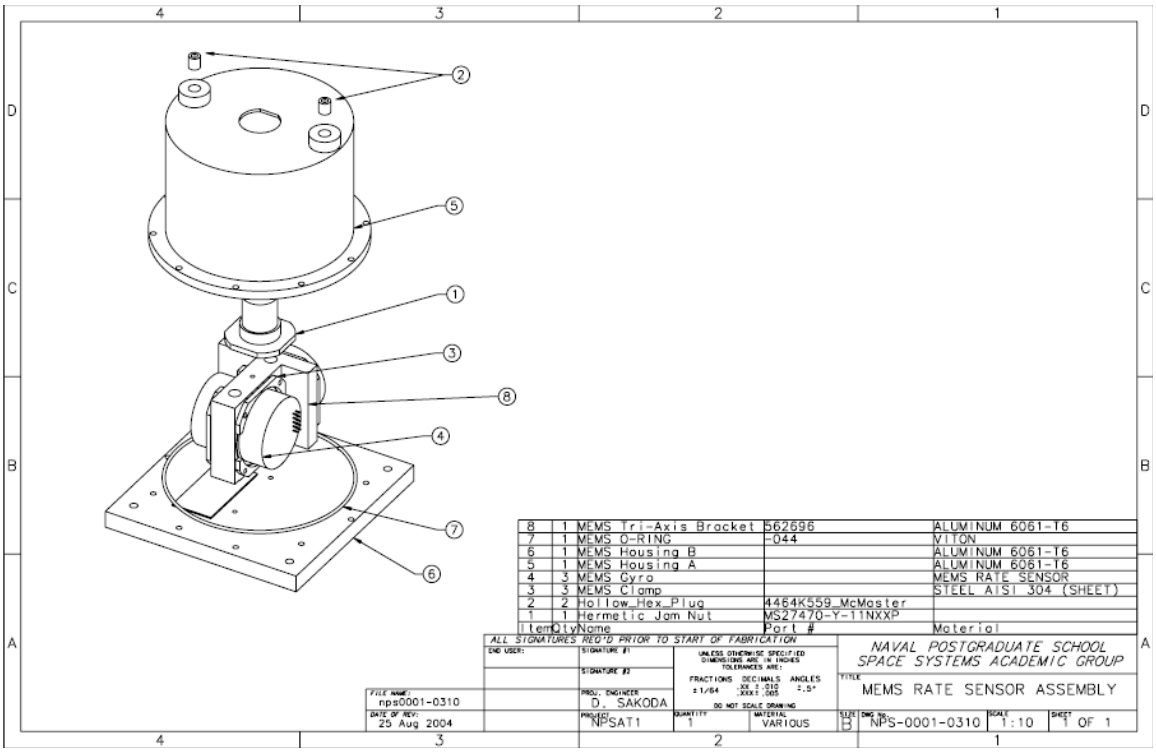

Figure 2. MEMS Assembly.

This belief persisted for a number of years as the project progressed through the stages of spacecraft research, design and development, and the MEMS experiment slipped into obscurity. It was not until recently that the MEMS experiment was re-addressed, and a decision was made to re-investigate the MEMS sensor experiment for possible modification prior to integration. It was not known that this research endeavor

would lead to major revelations into the operations and characterization of the MEMS sensors. This thesis shows that a solid understanding of the performance characteristics of the sensor allows optimization of the variables affecting its performance. It now appears that the QRS11 rate sensors can be optimized to perform accurately in rate environments well below their design limits. Not only are these sensors capable of accurately measuring orbital rate (0.066°/s), but they can accurately measure rates as low as 1/7 orbital rate (0.001°/s), and are even capable of measuring the Earth's rotation rate (0.004°/s). This shift in the understanding improves the potential utility of this sensor in numerous ways. This thesis shows quantitatively how these MEMS sensors perform at very low rates.

D. MEMS RATE SENSOR PERFORMANCE REQUIREMENTS

To optimize and characterize the performance of the MEMS 3-Axis Rate Sensor Suite, a solid understanding of its performance requirements is first needed. This is paramount to the overall success of the experiments, as it will give us a solid experimental reference and developmental benchmark.

1. Rate Performance Requirements

The original operations plan for the MEMS sensor called for it to be used later in flight during experimental attitude control measurements to measure angular rates. This plan was later expanded to include experiments using the sensor that included monitoring the spacecraft's rotational rates in all 3-axes shortly after tip-off, while the ACS used its B-dot damping method to reduce the rates of the spacecraft down to twice orbital rate, called 2Ω, which is approximately 0.132°/s [6]. It was also planned to be used periodically during orbital operations to monitor rates of the spacecraft during routine attitude control. Yet at these rates, believed to be at the lowest end of the sensor's dynamic range, it was thought that the MEMS sensor data would become unreliable. Thus, the sensor would be primarily used experimentally during B-dot damping and during experimental attitude control maneuvers, and would need to be able to meet the performance requirements for this environment.

B-dot damping refers to a rate damping scheme using magnetometers to measure the B-field and magnetic torquers to try to align the spacecraft with the local B-field. B-dot damping requires a relatively short period of time, about 1,000 seconds, and is commanded from the ground to de-spin the spacecraft. B-dot dampening uses the magnetometer to take differential readings at set intervals, calculates the delta, and then applies force through the torquer coils to counteract the change. This is a brute force method, repetitively executed every two seconds by the ACS in the following way: one second of measurement, a half second of torqing and a half second for the torquer's magnetic field to relax and not interfere with the magnetometer's measurement of the Earth's B-field. This quickly reduces the rates of the spacecraft down to more manageable rates, where a more complex and accurate attitude control algorithm will replace the B-dot procedures.

For the MEMS to be useful it will need to produce accurate measurements within this cycle, continuously supplying the ACS with accurate rate data. This will allow the ACS to use accurate rate data on the same cycle as its magnetometer measurements, and disregard data that is obtained while the torquer coils are being used. Setting a benchmark for initial testing, it was decided that the accuracy of the rate data should be within ±5% of the actual rate. At an orbital rate of 0.066°/s (33 mV output), this translates to about ±1.65 mV.

2. Temperature Performance Requirements

The original operations plan of the MEMS subsystem did not require the use of a temperature output. This thesis shows how important the temperature of the QRS11 is, and the impact it has on the accuracy of the rate output. While the temperature is not directly related to the attitude control of the spacecraft, it is directly related to the accuracy of the MEMS rate output, and therefore it will need to be continually accessible by the ACS, and be sampled at the same time as the rate outputs.

The temperature output of the MEMS sensor suite has a much smaller dynamic range (-0.3 V to 0.1 V) than that of the rate output (±2.5 V). This corresponds to a temperature range of -40°C to 55°C. But the anticipated operational temperature range

the sensor will be exposed to is much smaller. Martin Gruhlke completed a thesis in 2003 entitled "Computer Aided Thermal Analysis of a Technology Demonstration Satellite." He determined that the expected temperature range for the MEMS sensor was -11°C to 9°C [9]. This translates to a dynamic output range of about -0.15 V to -0.08 V. Again, setting a benchmark for initial testing, it was decided that the accuracy of the temperature data should be slightly more than the rate data due to its limited dynamic range, within ±2% of the actual temperature, which translates to about ±1.40 mV.

3. BIT Performance Requirements

The BIT output from the MEMS sensors has a very limited purpose. It reports the operational status of the sensor, telling the ACS the operational state of the MEMS subsystem, and whether or not to use data. If the sensor is operating correctly, it will have a BIT output of ≥ 2.4 V. If the sensor is not operating correctly, the BIT output will read ≤ 0.8 V. Greater than 2.4 V represents a TTL logical true, or operational, and less than 0.8 V represents the logical false, or non-operational. Thus, we can sample this data much less frequently than we do the sensor rates and temperatures, perhaps as little as once a second. This will free up sampling resources of the ACS, potentially allowing additional sampling of the more important rate and temperature data, which could improve signal accuracy.

E. MEMS RATE SENSOR OPERATIONAL REQUIREMENTS

The MEMS 3-Axis Rate Sensor Suite must be able to survive the harsh environment of both launch and space. If the sensor suite is unable to survive the launch and space environments, or if it is not compatible with the spacecraft bus and other subsystems, the overall sensor suite becomes useless. Therefore, understanding the environment in which the MEMS hardware must exist and operate is necessary to properly test and qualify the final flight assembly.

1. The Launch Environment

Physically, the launch environment is the most structurally dynamic time that a spacecraft will experience. Launch stresses, while great, have been well documented and

are fairly well understood. These stresses are directly related to the individual launch vehicle, with each launch vehicle having a specific launch profile, much like a signature. Careful evaluation of these launch profiles needs to be completed prior to launch, and their effects on the spacecraft and individual subsystems analyzed.

a. Vibrational Requirements

The QRS11 sensor must be able to survive the launch vibrational profile expected during its ride to orbit. NPSAT1 was initially scheduled to launch with the STP-1 mission aboard an Atlas V in December 2006, and was designed to interface with the Expendable Launch Vehicle (EELV) Secondary Payload Adapter (ESPA). Though NPSAT1 was unable to meet this launch window, the program will continue to test to this launch profile until a new launch opportunity arises, and a new launch vehicle is selected. The booster launch profile for an Atlas V was provided to the NPSAT1 program office by the Integrating Contractors (IC) at Boeing. The NPSAT1 Experimental Development Unit (EDU) then underwent qualification testing of this profile on a vibrational table in all 3-axes by NRL in September 2005 [1]. The test included burst testing for static loads simulating 15 g peaks in each axis, followed by random vibration testing to +6 db above the Maximum Predicted Environment (MPE) of the launch vehicle, or 14.2 g(rms) [4]. Accelerometers were placed at specific locations on each deck of the EDU, resulting in individual launch profiles with a factor of margin for all four of the spacecraft decks.

Each spacecraft subsystem is required to meet the vibrational profile of the deck to which it is mounted. The MEMS subsystem is located on deck three of the spacecraft, thus all dynamic testing of the MEMS will be based on the EDU vibrational test results from deck three. The QRS11 is specified to survive 20 g(rms) at 20 Hz to 2000 Hz random for five minutes per axis, and operate at 8 g(rms), with a max shock of 200 g in any axis. The final MEMS rate subsystem must be vibrational tested to the Deck 3 qualification level, as shown in Figure 3.

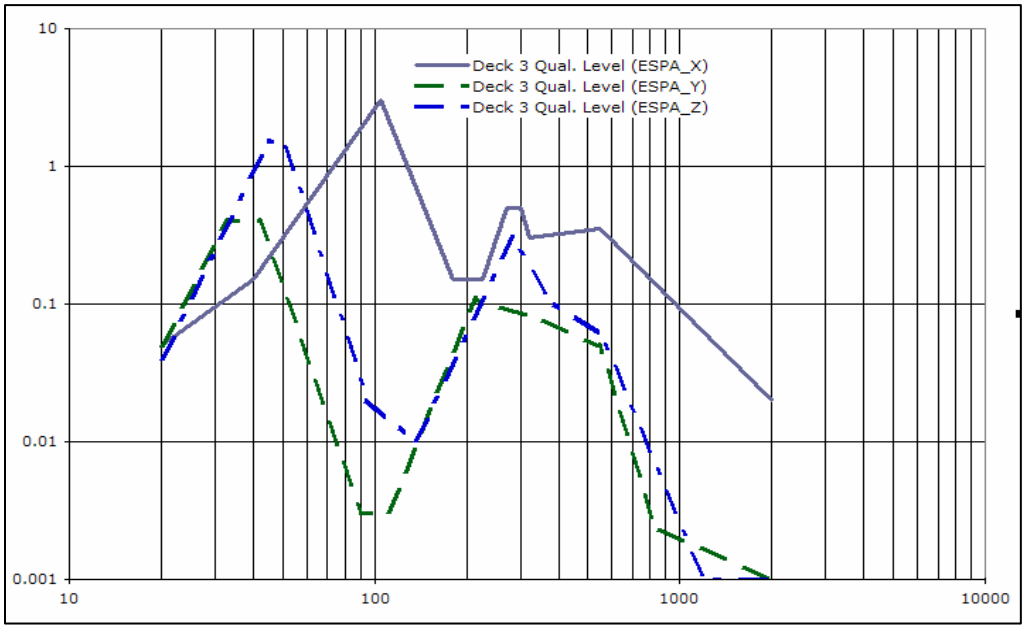

Figure 3. Deck Three Launch Profile (Vibrational).

2. The Operational Environment

Space is an unforgiving and harsh environment. To be able to operate a spacecraft successfully in it requires a firm understanding of the space environment, its effects on spacecraft, as well as procedures to minimize the impact of these hazards on the spacecraft and its mission. The major hazards of the space environment include radiation, spacecraft charging, debris, surface effects, and thermal cycling [10]. Because the MEMS sensor suite is pressurized at one atmosphere and is housed inside of the NPSAT1 spacecraft, we consider the risks of spacecraft charging, debris, and surface effects as negligible, and will focus on the primary threat of thermal cycling, as well as radiation.

a. Thermal Requirements

The sensor must be able to operate in the broad thermal environment of space. In Low Earth Orbit (LEO), the spacecraft can expect to go through a hot and cold cycle every ninety minutes, with approximately sixty minutes of this being in the sun, and thirty minutes in eclipse. This type of thermal cycling can be very stressful on subsystems, and it is thus necessary to understand the thermal environment that the

spacecraft and its subsystems will be exposed. The QRS11 sensor was designed to operate between -40°C and +80°C, but we will most likely see a much smaller temperature range during operations. Martin Gruhlke examined four separate thermal cases, which included a worst-case hot in normal and low power modes, and a worst-case cold in normal and low power modes. A combination of the results showed that the MEMS subsystem would have a maximum expected face temperature of between -11°C and 9°C [9]. Due to the thermal mass of the MEMS housing he anticipated that the actual MEMS sensor temperature will remain fairly constant at around 5°C. This will be due to the slow oscillation of thermal cycles through the subsystem, as well as the heat produced while the MEMS and Power Control and Filter Boards (PCFB) are powered.

The anticipated temperature range is based on a model, and like all models, it is subject to analytical errors. Also, the spacecraft is no longer manifested to any specific launch and thus has an unknown orbital altitude, inclination, and thermal environment. This makes it important to add margin to the expected operational temperature range of the subsystems. Once a new launch opportunity arises, a more accurate thermal analysis can be done and these margins can be reduced. For these reasons, we chose an operational temperature range of ±20°C for the purpose of this thesis. This is the temperature range that the MEMS will be tested to during its characterization testing. For flight acceptance and qualification, the temperature requirements were determined by the launch vehicle safety officers and the IC. For this launch, the temperature range for acceptance and qualification of a non-operating flight unit is -29°C through 66°C [4]. This requirement says that all subsystems must be tested to this temperature range and survive with no catastrophic failures.

b. Radiation Requirements

Radiation is a serious hazard of the space environment, and a major issue to contend with when designing spacecraft. Space contains large numbers of high-speed particles and energetic photons. Any object placed in space will be impacted by these particles and photons, and depending on circumstances, varying degrees of radiation damage will result [10]. Unfortunately, the QRS11 sensor was not designed for use in

space. It was originally designed for missile guidance and control, and although it has been recently shown to operate well in the space environment, there is no quantitative data available on the radiation performance of the QRS11 from the manufacturer. However, due to its recent use in a few spacecraft mentioned in the next chapter, space radiation tests have been performed on the standard QRS11 by one of SDI's customers, and these results were forwarded to SDI for distribution.

The testing by this customer included total dose (Cobalt 60, increments up to 80 Krad), and heavy particle (californium 252 to a fluence of 1.9×10^6 particles/cm^2). The complete sensor, as a component, was also tested for total dose. For the heavy particle tests, the metallic cover of the QRS11 was removed for direct application of the radiation to the ceramic package containing the semi-conductor on the power board. These radiation exposure levels were program requirements of the customer, and do not necessarily mean that the QRS11 cannot survive higher levels of exposure [11]. The QRS11 inputs and outputs were monitored during all the radiation tests for performance changes and single event upsets. No effects due to radiation exposures were noted during or after the tests. Therefore, these results, and considering the additional shielding around the MEMS sensor suite, suggest that the risks from on-orbit radiation are negligible.

3. Spacecraft Interface

After the MEMS subsystem is successfully developed, tested, and determined to be able to withstand the harsh environments of both launch and space, it must also be able to successfully interface with the spacecraft bus. Careful planning and procedures need to be developed to ensure that the links between the MEMS, the wiring harness, and the spacecraft buss induce little to no additional noise into the outputs. The most obvious errors in interfacing can often be attributed to grounding, cabling, and connector errors, as well as differences in expected data flow and data packaging.

a. Input Requirements

The spacecraft's bus will be providing the MEMS sensor suite with ±6 VDC, as well as a common return through three pins of a 15-pin connector linking the MEMS wiring harness to the ACS. The QRS11 sensors require an input of ±5 VDC, with a tolerance of ±3%. The manufacturer states that the QRS11 is sensitive to power line noise and so a voltage regulator and power filter will need to be integrated into the MEMS subsystem in the form of a Power Regulation and Control Board (PRCB). The steps for the testing and building of this board will be found later in Chapter V of this thesis.

b. Output Requirements

The MEMS must provide the ACS with rate, temperature, BIT, and signal ground data for all 3-axes using the single 15-pin connector allocated to the MEMS device. Other than meeting the performance requirements noted earlier in this chapter, the only output requirements that must be meet deal with the interfacing of the wiring harnesses. For the most accurate data to be obtained, the ACS 12-bit Analog to Digital Converter (ADC) will need to ensure that the rate, temperature, and BIT outputs from each axis are measured with respect to the signal ground of each axis. Failure to do this could result in possible induced noise into the measurements.

II. MEMS RATE SENSORS

A. MEMS TECHNOLOGY

Over the last two decades there has been a surge of interest in the use of MEMS components in almost every technological field. Since the first use of MEMS components in a space mission in the mid-90's, the technology has quickly begun to gain acceptance by the space community. While the idea of solid state gyros has been around for quite a while, it has only been in the last fifteen years that the technology has become mature enough to foster its development into functioning systems. MEMS technology is well suited to space applications. MEMS sensors are smaller, weigh less, are less complicated, have few failure modes, and are less expensive. For a spacecraft designer, these attributes provide significant advantages over mechanical sensors, and have direct benefits to the overall spacecraft, and are important in spacecraft design.

B. THE SYSTRON DONNER INERTIAL QRS11 RATE SENSOR

When the QRS11 was selected for use in NPSAT1 in 2001, it was considered one of the best MEMS angular rate sensors available. SDI is a pioneering force in the field of MEMS development and manufacturing, and the QRS11 was a mature product in high volume production since 1991 [12]. At the time, SDI had fielded thousands of units for applications in stabilization, control, guidance, instrumentation, and navigation across numerous fields such as aircraft attitude control, missile guidance, and automobiles: yet it had had very little exposure to space applications. The QRS11's well established and documented capabilities, and its reasonable price, prompted the NPSAT1 program team to select it for use as the MEMS experiment on NPSAT1. The QRS11 can be seen below in Figure 5.

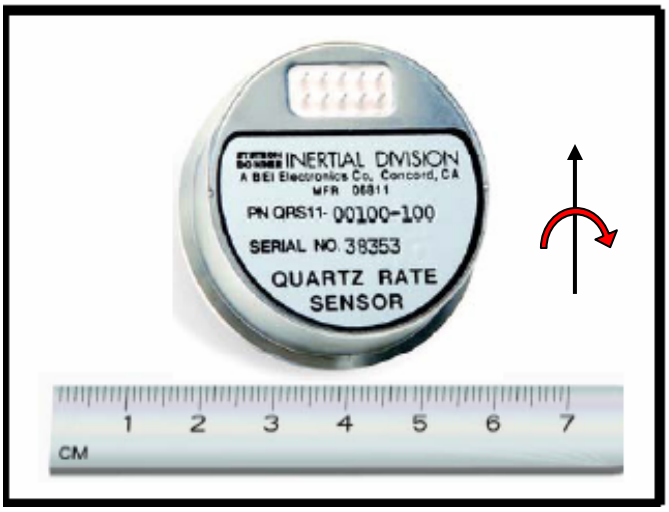

Figure 4. QRS11 Sensor.

The QRS11 is an innovative micro-miniature solid-state gyroscope that utilizes a double-ended quartz tuning fork as its sensing element to sense angular velocity. These components are all fabricated chemically from a single wafer of pure mono-crystalline piezoelectric quartz [13]. Unlike traditional mechanical gyroscopes which are mechanically complex, containing hundreds of individual precision parts and having a limited life, SDI's quartz sensors feature a monolithic sensing element with no known modes of wear out [13]. The pin layout of the QRS11 can be seen below in Figure 5.

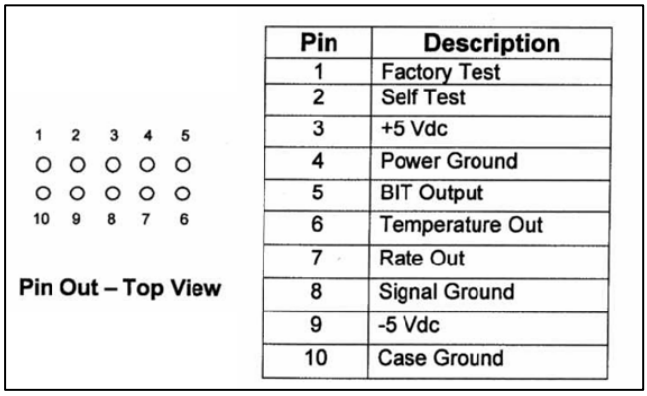

Pin	Description
1	Factory Test
2	Self Test
3	+5 Vdc
4	Power Ground
5	BIT Output
6	Temperature Out
7	Rate Out
8	Signal Ground
9	-5 Vdc
10	Case Ground

Figure 5. QRS11 Pin Layout.

The basic working principle of a rate gyroscope is founded on the generation and detection of a coriolis acceleration. A rotational motion about the sensor's input axis produces a DC voltage proportional to the rate of rotation. This voltage is output from the sensor, along with sensor temperature and BIT voltages to a measurement device, and can be used to determine angular rates very accurately. The sensing element operations diagram can be seen below in Figure 6.

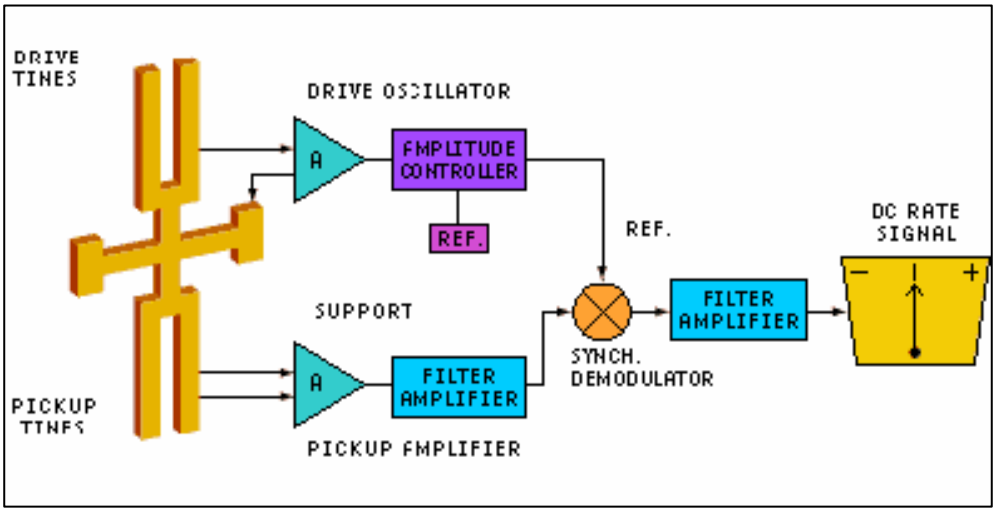

Figure 6. QRS11 Sensing Element Operations.

1. Capabilities

To determine the feasibility of an individual sensor for use in the MEMS experiment, factors including the dynamic rate range, operating temperature range, output noise, bias variation over temperature and time, cost, and vibrational range were considered. The QRS11 Specifications Sheet can be seen below in Table 2.

PARAMETER	SUMMARY SPECIFICATIONS		
Part Number	QRS11-00100-100	QRS11-00100-101	QRS11-00005-565
Performance Level	Standard	High	High
Power Requirements			
Input Voltage	+ and – 5 Vdc ±3% regulation		
Input Current	≤80 mA (each supply)		
Input Power Noise Limits	<10 mV_{rms} wideband, except at 8.7 ±0.5 kHz, <1 mV_{rms}		
Performance			
Standard Range Full Scale	± 100°/sec.		±5°/sec
Full Scale Output (Nominal)	±2.5 Vdc		
Scale Factor Calibration (at 22°C Typical)	≤1% of value		
Scale Factor over Temperature (Dev. from 22°C Typical)	≤0.03%/°C		
Bias Calibration (at 22°C Typical)	≤2.0°/sec.*	≤0.5°/sec.*	0.131°/sec
Bias Variation over Temperature (Dev. from 22°C)	≤1.80°/sec.*	≤0.35°/sec.*	0.117°/sec
Short Term Bias Stability (100 sec at const. temp)	<0.01°/sec, typical*		
Long Term Bias Stability (1 year)	≤0.2°/sec.*		
G Sensitivity (Typical)	≤0.02°/sec/g		
Start-Up Time (Typical)	< 1 sec.		
Bandwidth (-90°)	>60 Hz		
Non-Linearity (Typical) % Full Range	≤0.05%		
Threshold/Resolution	≤0.004°/sec.*		
Output Noise (DC to 100 Hz)	≤0.01°/sec./√Hz*		0.004°/sec/√Hz
Environments			
Operating Temperature	-40°C to +80°C		
Storage Temperature	-55°C to +100°C		
Vibration Operating	8 g_{rms} 20 Hz to 2 kHz Random (Consult factory for other vibration level requirements)		
Vibration Survival	20 g_{rms} 20 Hz to 2 kHz random 5 minutes/axis		
Shock	200g, any axis		
Weight	≤60 grams		
AVAILABLE OPTIONS			
• Special Non-Standard Ranges <±100°/sec. and >±100°/sec., Consult Factory • Extended Bandwidth • Low Noise • Extended Temperature Range • Flying Leads			
*Values indicated are for ±100°/sec. range			

Table 2. QRS11 Specification Table (Standard Version).

As can be seen from the standard QRS11 performance specifications table, the standard package has shortcomings in two important areas. First of all, the dynamic range of the standard sensor at ±100°/s, is at least twenty times greater than what is desired. This could lead to significant resolution degradation when making measurements at the lowest of the anticipated rates. Likewise, the specifications for bias over temperature and output noise are so high that accurate measurements at very low rates would be quite difficult. Therefore, the following options were selected and purchased with the QRS11 sensors: The high-performance option (-101), a non-standard

rate range option (±5°/s max rate), and the low-noise option (-565). The total price came to $3,472.00 per sensor in 2001. The high-performance option provided better bias calibration at ambient temperature and better bias over temperature range than the standard performance version. The non-standard rate range option brings the dynamic range of the standard version down from ±100°/s to ±5°/s, and the low noise option reduces the output noise to about 50% of that of the standard version. These options are necessary to maximize the utility of the sensors in the experimental environment in which they are to be used. Although the expectations for the MEMS experiment were not particularly high, maximizing the sensor's ability to take accurate measurements at the lowest of rates increases the likelihood of positive experimental results.

2. Space Use of the QRS11 as of 2007

In 2001, when the QRS11 angular rate sensor was chosen for integration into the NPSAT1 mission as a 3-axis sensor suite, the sensor had only been flown in space in limited roles. One of the primary goals of the MEMS experiment was not only to verify rates from the magnetometer, but to gain flight experience with MEMS devices for possible implementation into future missions. NPS was not alone in its curiosity about MEMS sensors, and numerous other organizations were also beginning to recognize their overall utility and potential advantages in space flight. Since the selection of the QRS11 angular rate sensor for use with NPSAT1 in 2001, the QRS11 has been used in a number of space missions. Below is a list and description of the QRS11 space flight experience.

a. NASA, STS-64, SAFER Experiment, September 1994

This is the first use of the Standard off-the-shelf version of the QRS11 in space. In this mission, a tri-axial configuration of the QRS11 sensor served as the inertial reference unit for the space station and space shuttle astronaut Extra-Vehicular-Activity (EVA) safety backpacks [11]. The backpacks are called the Simplified Aid for EVA Rescue (SAFER) system. The system uses a cold gas propellant that provides the astronaut the chance to return to the spacecraft if he "falls off" during an EVA. The rate ranges of these sensors are ±100°/s in all 3-axes, with the anticipated rates being up to

10°/s. Although this experiment proved the ability of the sensor to operate in space, the high rate as well as the low-accuracy requirements did not prove the sensors' ability to perform at low rates, specifically for spacecraft rate determination.

b. NASA, Mars Rover Mission, Sojourner, December 1996

In this mission a single Standard off-the-shelf version of the QRS11 sensor was used to provide the rover's onboard computer with inertial heading references for its navigation on the surface of Mars. The rate range of a standard sensor is ±100°/s in yaw, with a short-term bias stability of <0.01°/s [12]. To overcome this characteristic bias, the channel was updated by a zeroing circuit that was switched on when the vehicle was not moving [11]. While not a qualification for space flight, the use of the sensor on another planet did help prove its capability in harsh environments.

c. NASA, STS-87, AERcam Experiment, November 1997

This is the second use of the Standard off-the-shelf version of the QRS11 sensor in space. Expanding on what was learned from the use of the QRS11 sensor in the SAFER units, NASA developed the Autonomous EVA Robotic Camera, and used a tri-axial configuration of the QRS11 sensor (±100°/s) to provide the inertial reference and stabilization unit for the drone [11]. It was a free-flying, cold gas powered, 35 centimeter diameter sphere carrying TV cameras. It was controlled by a radio from inside the orbiter, and was used to perform inspections outside the orbiter. The stability and pointing accuracy of the inertial reference system and resulting TV images were reported as being "extremely precise" by the astronauts [11]. This is the first use of the QRS11 sensor to provide a high level of precision and pointing accuracy, and the sensor performed well enough to be taken seriously as a potential source of inertial navigation for spacecraft requiring high pointing accuracy.

d. Surrey Satellite Technology Ltd (SSTL), UoSat12, April 1999

This is the first use of a low rate version (±5°/s) of the QRS11 sensor in a tri-axial configuration to serve in the ACS for a satellite [11, 14]. The satellite carried a

number of imaging payloads, as well as a propulsion system designed for orbital housekeeping experimentation. The imaging cameras included a Kodak panchromatic Earth imaging camera, capable of 10 m resolution, as well as a multi-spectral camera, capable of 40 m resolution.

e. ESA, Integral Spacecraft, October 2002

The European Space Agency's (ESA) International Gamma-Ray Astrophysics Laboratory was designed to detect some of the most energetic radiation that comes from space, and is the most sensitive gamma-ray observatory ever launched [15]. The spacecraft is over five meters long, 3.7 meters in diameter, and weighs over four metric tons. The QRS11 was used as a component of the Rate Measurement Unit (RMU), and successfully passed boost and orbital environmental testing, as well as space radiation tests [11]. This was the first time the QRS11 sensor was tested and qualified for radiation exposure in space. Although the sensor suite was used successfully in the RMU to stabilize the spacecraft, it was not used for pointing.

f. ESA, Smart 1, September 2003

The European Space Agency's SMART-1 mission was designed to test solar electric propulsion and other deep-space technologies, while performing scientific observations of the Moon [16]. Among other investigations, mission data would help provide answers to questions on the origin of the Moon and to search for ice in the craters at the Moon's South Pole. The QRS11 was used as part of the Spacecraft System Unit, developed by the Swedish Space Corporation specifically for SMART-1. Five QRS11's were used in conjunction with four reaction wheels to provide primary and redundant attitude control. The mission ended on September 3, 2006, when the spacecraft impacted the lunar surface.

g. ESA, GIOVA-A Spacecraft, December 2005

The European Space Agency's Galileo In-Orbit Validation Element A was the first of two experimental spacecraft designed to validate technology prior to the

fielding of the Galileo Positioning System. The four major mission goals were to protect the frequency filing prior to expiration, the validation of key payload technologies, the measurement of the orbital radiation environment, and capturing satellite-to-ground link performance measurements [17]. The High Performance (±50°/s) version of the QRS11 was used in two tri-axial configurations in the Attitude and Orbit Control Subsystem (AOCS), and was chosen for GIOVE-A due to cost constraints and because of the relatively relaxed mission rate-sensor requirements [17]. The QRS11 sensors provided rate information to perform missions including de-tumbling, sun acquisition, and sun acquisition mode with coning.

h. ESA, Planck Probe, Planned for July 2008

The European Space Agency's Plank Surveyor, previously named the COsmic Background Radiation Anisotropy Satellite / SAtellite to Measure Background Anisotropies (COBRAS/SAMBA), was designed with the primary goal of producing high sensitivity, high angular resolution maps of the microwave sky, and thus the cosmic microwave background [18]. The QRS11 was used in two tri-axial configurations for redundancy in the Attitude and Orbit Control Subsystem (AOCS). The satellite is spin-stabilized at one rpm about the longitudinal axis, with a pointing error of 16.9 arcsec [18].

i. ESA, Herschel Space Observatory, Planned for July 2008

The European Space Agency's Herschel Space Observatory, previously named the Far Infrared and Sub-millimeter Telescope (FIRST), was designed to be the first astronomical satellite to study the cold universe at far-infrared and sub-millimeter wavelengths. Its main goal is to look at the origins of stars and galaxies, reaching back to when the universe was only one third of its current age. The QRS11 was used in two tri-axial configurations for redundancy in the AOCS. The satellite is 3-axis stabilized, with a pointing error of 2.12 arcsec [18].

C. CURRENT STATE-OF-THE-ART MEMS RATE SENSORS

Over the last decade, MEMS technology has quickly worked its way into almost every facet of industry and science. Since the selection of the QRS11 in 2001 for use on NPSAT1, there have been some significant technological advancements throughout the industry. Not only has the technology of the MEMS components improved, but the manufacturing technology has improved as well. This, coupled with the ever increasing acceptance of MEMS technology, has lead to an increasing demand for MEMS components in almost every market. And as the demand for MEMS components grows, so does the number of companies producing them. Asked to re-assess the options and re-select a MEMS angular rate sensor based on what is available today, would the QRS11 be selected? Clearly the QRS11 Standard Version has been proven flight-qualified. For the purpose of a flight experiment today, would a new, more advanced sensor be selected?

For the purpose of comparison, certain criteria will be used to compare the current state-of-the-art MEMS angular rate sensors to the QRS11. These criteria include rate range, temperature range, power supply requirements, noise output, vibration tolerance, cost, bias over temperature, BIT capability, and if the sensor provides a temperature output. In addition to these, the overall advantages, disadvantages, and potential for each sensor will be addressed. Each sensor's description includes a table that graphically depicts the selection criteria mentioned above, as well as a color-coded value assignment. These value assignments carry the following weight: a black code indicates failure to meet basic requirements; a red code indicates lower performance than the QRS11; a yellow code represents equivalent performance; and a green code represents improved performance.

1. BEI Systron Donner QRS100

The QRS100 is the next generation of MEMS single-axis angular rate sensor technology for SDI. It is the product of years of research and state-of-the-art fabrication processes, yielding significantly lower noise and better vibration performance. Compared to the QRS11, the QRS100 has two major improvements. First, the specified

output noise of the sensor was reduced from ≤ 0.01 °/s/√Hz, to ≤ 0.0035 °/s/√Hz, a three-fold improvement. Secondly, the sensor was optimized for tougher vibration and shock environments. The QRS100 increases the vibrational range of the QRS11 from 8 g(rms) to 20 g(rms), and the maximum shock survival from 200 g any axis to 1,000 g any axis [19]. This makes this sensor ideal for use in environments where the reduction of noise is crucial, or where high vibration forces are expected.

In addition to these advancements, the QRS100 has one other advantage which must be mentioned: it is physically identical to the QRS11. This gives this sensor a significant advantage over other potential replacements as little or no system and subsystem re-design will be needed. The QRS11 could literally be swapped out with the QRS100, and after some simple characterization tests for temperature dependant bias, should be fully functional. The only disadvantage this sensor has is the fact that it has been temporarily discontinued due to an ongoing export control investigation, but it is expected to be available within the next year.

Rate Range	± 100 °/s, with options as low as ±5 °/s	
Temperature Range	-40 °C to +80 °C	
Power Supply	± 5V ±3% @ 0.06 amps each (0.9 W)	
Noise Output	< 0.0035 °/s/√Hz	
Vibrational Range	20g(rms)	
Cost	$ 3060.00 (US)	
Bias Variation over Temperature	< 0.35 °/s (High Performance)	

Table 3. QRS100 Performance Criteria.

2. Memsense TriRate

The Memsense TriRate is a Tri-axial MEMS angular rate sensor capable of measuring angular rates in all 3-axes in a single, small, and lightweight package. The package is half the size of a single QRS11, which could make this sensor ideal for smaller spacecraft [20]. Like the QRS11, the TriRate sensor has a temperature output, but unfortunately does not have a BIT output. This is just one of several disadvantages. First of all, the sensor's specific noise output is five times greater than the QRS11. Likewise, the smallest rate range available in the TriRate is ±150°/s, thirty times larger

than that of the QRS11. These facts have the potential to cause significant measurement and resolution errors at very low rates, which at LEO (approximately 0.07°/s) represent less than 0.05% of the entire dynamic range of the sensor.

Interestingly, Memsence makes another model of sensor called the MAG3 ($1,005.00). This sensor incorporates a tri-axial magnetometer, accelerometer, and angular rate sensor, in a single, self contained, all-in-one package [20]. Though the sensor's characteristics are similar to the TriRate, and thus not ideal, it has the potential for use as a stand alone attitude control system for use with smaller satellites.

Rate Range	± 150 °/s	
Temperature Range	-40 °C to +85 °C	
Power Supply	4.75 to 5.25 V Single Supply @ 0.018 amps (0.1 W)	
Noise Output	≤ 0.05 °/s/√Hz	
Vibrational Range	20g(rms)	
Cost	$729.00 (US) Total	
Bias Variation over Temperature	Unknown	

Table 4. Memsence Performance Criteria.

3. Silicon Sensing CRS03

The SILICON Sensing CRS03 is a single-axis angular rate sensor that is very similar in size, shape, and operation as the QRS11. Unlike the QRS11, this sensor is not based on a MEMS quartz tuning fork, but rather a MEMS silicon ring. This, coupled with closed loop electronics, gives the sensor very stable performance over time and temperature, overcoming the mount sensitivity problems sometimes experienced with tuning fork based sensors [21]. Unfortunately, these benefits do not seem to translate to low rate applications, leaving this sensor with some drawbacks.

The sensor only has three pin leads, two for power and the third for the rate output. Thus, no temperature data is available, unless external components are added, making it difficult to compensate for temperature, often a key parameter in the characterization of sensors, and for the removal of temperature dependant bias. There is also no BIT output, which allows health and status of the sensor to be monitored. Next, the sensor's noise output is five times greater than the QRS11. Likewise, the smallest

rate range available in the CRS03 is sixteen times larger than that of the QRS11, and the specified bias variation over temperature is twelve times larger. Lastly, the sensor lists a vibrational tolerance range of only 2 g(rms), which is four times less than that of the QRS11. These factors contribute to making this sensor a poor choice as a potential replacement.

Rate Range	± 80 °/s	
Temperature Range	-40 °C to +85 °C	
Power Supply	4.75 to 5.25 V @ 0.035 amps each (0.5W)	
Noise Output	≤ 0.1 °/s/√Hz	
Vibrational Range	2g(rms)	
Cost	$250.00 (US) each (Total of $750.00)	
Bias Variation over Temperature	≤ 4 °/s	

Table 5. CRS03 Performance Criteria.

4. Gladiator Technologies G10

The Gladiator Technologies G10 is a single-axis angular rate sensor that is operationally very similar to the QRS11. Like the QRS11, the G10 provides both a temperature output as well as BIT output, which are crucial for accurate bias compensation and rate measurements [22]. Compared to the QRS11, the G10 is only 1/3 the size and 1/6 the weight, and is much cheaper at only a fraction of the cost. Additionally, the G10 has a slightly broader thermal range. Unfortunately, these advantages are dwarfed by its disadvantages. First of all, the sensor's specified noise output is five times greater than the QRS11. Likewise, even with the smallest custom rate range available, the rate range of the G10 is six times larger than that of the QRS11, and the bias variation over temperature is just under two times greater. These characteristics will contribute to measurement and resolution errors at very low rates, at LEO this represents less than 0.2% of the dynamic range of the sensor.

Rate Range	± 75 °/s (Custom to ± 30 °/s)	
Temperature Range	-40 °C to +85 °C	
Power Supply	4.75 to 5.25 V @ 0.008 amps each (0.12 W)	
Noise Output	< 0.05 °/s/√Hz	
Vibratinal Range	6g(rms)	
Cost	$225.00 (US) each (Total of $675.00)	
Bias Variation over Temperature	< 0.5 °/s	

Table 6. G10 Performance Criteria.

5. Honeywell GG1178

The Honeywell GG1178 is a single-axis angular rate sensor capable of providing low noise output signals with excellent performance over a large temperature range [23]. The GG1178 is about one quarter the size of the QRS11, and provides a BIT output for monitoring sensor health and status, but does not provide a temperature output. The only advantage this sensor has over the QRS11 is its increased temperature range, which is outside the benchmark range for this experiment, and therefore unnecessary, as well as it's extremely low cost. Yet this sensor does have some significant disadvantages. First of all, the sensor's specified noise output is ten times greater than the QRS11. Likewise, the smallest rate range available for the GG1178 is ten times larger than that of the QRS11, and the bias variation over temperature is three times higher than the QRS11. In addition to this, the vibration operational range is 2.5 times less than that of the QRS11.

Rate Range	±50 °/s	
Temperature Range	-40 °C to +125 °C	
Power Supply	4.75 to 5.25 V Single Supply @ 0.035 amps each (0.5 W)	
Noise Output	< 0.1 °/s/√Hz	
Vibrational Range	3.2 g(rms)	
Cost	$49.00 (US) for a total ($147.00)	
Bias Variation over Temperature	1 °/s	

Table 7. GG1178 Performance Criteria.

6. Melexis MLX90609-N2

The Melexis MLX90609-N2 angular rate sensor is a full gyroscopic system packaged in a single surface mount device, containing a high-performance silicon MEMS sensor and signal conditioning circuitry, capable of providing high resolution and low

output drift signals [24]. Like the QRS11, the MLX provides a temperature output, but it does not provide a BIT output. Compared to the QRS11, the MLX is much smaller, about one quarter the size. Like the Honeywell sensor, the only advantage of this sensor over the QRS11 is in its expanded temperature range, which is of limited utility. These characteristics do not compensate for the disadvantages of this sensor. The sensor's noise output is three times greater than the QRS11. Likewise, the smallest rate range available for the MLX is fifteen times larger than that of the QRS11, and the bias variation over temperature is fifteen times greater.

Rate Range	±75 °/s	
Temperature Range	-40 °C to +85 °C	
Power Supply	4.75 to 5.25 V Single Supply @ 0.025 amps each (0.4W)	
Noise Output	≤ 0.03 °/s/√Hz	
Vibrational Range	Unknown	
Cost	$76.43 (US)	
Bias Variation over Temperature	5 °/s	

Table 8. MLX90609-N2 Performance Criteria.

D. COMPARISON OF CAPABILITIES TO REQUIREMENTS

Numerous MEMS angular rate sensors have been investigated and the six sensors with the most apparent potential for possible replacement of the QRS11 were selected for comparison. Each of these candidate sensors where thoroughly researched, including online research as well as phone interviews, to extract all relevant data with regards to the pre-determined and aforementioned selection criteria. In addition to this, the overall advantages, disadvantages, and potential for each sensor to replace the QRS11 were addressed. For the purpose of comparing each of the six potential replacement sensors to the QRS11, each of the criteria was assigned a weight in meeting the requirements of the NPSAT1 mission. These assigned weights were then multiplied by a QRS11 baseline of one, and set as the comparison values for the QRS11.

The criteria values for each of the six replacement sensors were calculated as a function of each criterion's relative performance percentage compared to the QRS11 baseline, multiplied by the assigned weight. That is, if the rate dynamic range of a

replacement sensor is ±10°/s, the relative performance percentage would be ±5°/s divided by ±10°/s, or 0.5. This relative performance percentage is then multiplied by the assigned weight of the rate dynamic range criteria, which is thirty. This yields the criteria value of 15 for that replacement sensor. If a value was unknown, it was assigned a 0.8 value. This value was based on the simple premise that if all things are equal, a new system will provide no utility over the current system. The total value of all nine criteria is then added together for the total value for each sensor. The sensor with the highest overall score is the sensor that has the best overall utility for the NPSAT1 mission. The results of this comparison can be seen below in Table 9.

Criteria	Weight	QRS11	QRS100	TriRate	CRS03	G10	GG1178	MLX
Rate Range	30	30.00	30.00	1.00	1.88	5.00	3.00	2.00
Temperature Range	1	1.00	1.00	1.00	1.00	1.00	1.00	1.00
Power Supply	1	1.00	1.00	1.00	1.00	1.00	1.00	1.00
Noise Output	25	25.00	71.42	5.00	5.00	5.00	2.50	8.33
Vibrational Range	10	10.00	25.00	25.00	2.50	7.50	4.00	8.00
Cost	1	1.00	1.56	14.28	13.88	15.43	70.85	45.09
Bias Variation over Temperature	15	15.00	15.00	12.00	1.25	7.00	5.00	1.00
Temp out	30	30.00	30.00	30.00	0.00	30.00	0.00	30.00
BIT out	15	15.00	15.00	0.00	0.00	15.00	15.00	0.00
Overall Weighted Score		128.00	189.98	89.28	26.51	86.93	102.35	96.42

Table 9. MEMS Comparison Table (Weighted).

As you can see, the QRS100 is the only sensor whose overall weighted score surpassed that of the QRS11, and therefore, it is the only sensor recommended for possible replacement of the QRS11. Yet, there are other sensors here that came close to the QRS11 and therefore warrant further investigation for possible use in future spacecraft. These sensors fell within 35% of the overall weighted score of the QRS11, and include the TriRate, the G10, the GG1178, and the MLX. Unfortunately, this is not a perfect comparison tool, and the reader will notice that the overall weighted scores for both the GG1178 as well as the MLX were heavily dependant on cost. While cost is a criteria for selection, it likely would not drive the overall weighted score. Therefore, we would only recommend the TriRate and the G10 for possible use in future experiments.

E. CONCLUSIONS AND RECOMMENDATIONS

Earlier in this chapter, the technological advancements of MEMS components over the last decade were discussed. Certain trends were observed that highlighted the direction which these technological advancements took. The most apparent advancement of MEMS technology came in the development of more efficient manufacturing processes. Increased production efficiency and competition fostered a significant decrease in relative cost of MEMS angular rate sensors compared to the original price of the QRS11. In 2001 when the sensor was purchased, it sold for $3,472.00. Today, the QRS11 sells for $2,221.00: this is a 36% decrease over seven years. The average price of all current MEMS angular rate sensor compared to the QRS11 has decreased by over 81% in the same period. Another advancement came in the form of unit scaling. The average size of MEMS sensors has also decreased dramatically over the last seven years, making them much smaller, with an average decrease in size of 65%.

In the previous section numerous MEMS angular rate sensors were investigated in order to answer the question; "if asked to re-assess the options, and re-select a MEMS angular rate sensor based on what is available today, would the QRS11 be selected? Or would a new, more advanced sensor be selected?" Our response to this question is "No". The QRS11 has been flown in space, and has been qualified on numerous spacecraft. Very little utility over the basic mission requirements will be gained from its use. The QRS100 has not been space qualified, and far greater knowledge and education could come from its inclusion. Unfortunately, the QRS100 has been temporarily discontinued pending International Traffic in Arms Regulations (ITARs) investigations. Before one decides to purchase it, one should pose the following questions. First of all, can they afford the time to wait up to a year for the sensor to be released? Can they afford the cost to purchase the new sensors? Can they afford the time required to re-verify integration and interoperability, as well as the re-characterization of the sensors? Is the net utility gain of the switch worth the expenditure of time and resources? And lastly, does the switch to a new sensor add any value to its experimental purpose? If the answer to all of these questions is yes, then we would highly recommend replacement of the sensor. If not, then the QRS11 will more than meet the requirements of the experiment.

III. EXPERIMENTAL PREPARATIONS

A. INTRODUCTION

Prior to characterization and experimental testing of the MEMS 3-axes rate sensor suite, the test equipment must first be described, understood, and characterized. Much of this equipment will be used multiple times in the experimental tests conducted during this research, and a separate description for each of these experimental setups would be redundant. Therefore, for the sake of efficiency, it was decided to present the basic function, set up, and operational procedures for this equipment in this chapter, leaving only variations and adjustments of this setup to be addressed during each experimental test.

B. THE TEST EQUIPMENT

Experimental results are only as accurate as the system used to measure them, therefore careful testing is needed to fully understand the test equipment characteristics. NPSAT1's ACS may be able to use the rate information provided by the QRS11 to stabilize the spacecraft in inertial or Earth pointing attitudes. To do so requires accurate measurement of rates on the order of 0.07°/s, called "orbital rate" for a LEO satellite. The QRS11 outputs a voltage equal to half the measured rate, i.e. for a rate of 5°/s the QRS11 outputs 2.5 V. A rate of 0.07°/s produces a 35 mV output. At such low rates it may be difficult to achieve accurate voltage measurements if the test equipment has unknown errors in the form of bias or noise that were not addressed prior to testing. Therefore, to ensure no such errors are introduced, it is very important to take every precaution to limit the noise and bias of the measurement equipment and their interfaces.

1. List of the Test Equipment

To fully understand and characterize the performance and operations of the MEMS sensor suite it was necessary to employ a wide variety of support, test, measurement, and data acquisition equipment. This equipment is listed below in Table 10, and was used in the characterization, experimentation, and testing of the QRS11

MEMS 3-axes rate sensor. This equipment was acquired from numerous sources in the SSAG, and with exception of the Thermal Vacuum Chamber (TVC), was all moved to the solar simulation lab and setup on the test bench in preparation for experimental testing. When experimental testing called for the use of the TVC, the necessary equipment was moved down into the satellite lab and set up on an alternate test bench next to the TVC.

Quantity	Equipment	Serial Number
1	CEC WebDAQ / 100	100A-00019-0004A2
1	Dell Demension C521 Computer	9DXH7C1
1	HP E3603A Triple Output Power Supply	KR34702193
1	HP 3478A Multi-meter	2545A23610
1	HP 6218A Power Supply	006374
1	Agilent Mega Zoom Spectrum Analyzer	SG41000916
1	Digital Multi-meterS (Micronta / Radio Shack)	N/A
1	Tektronix TDS 3012B Oscilloscope	B013082
1	HAAS TRT7 2-Axis Rotation and Tilt Table	Unknown
1	Scintifica Bath and Circulator Model 2067	20688-233
1	Tehnney Space Jr. Thermal Vacuum Chamber	12.494

Table 10. List of Test Equipment.

2. Description of the Test Equipment

Each piece of equipment listed in Table 10 was used numerous times throughout the research conducted during this thesis. While the purpose of this equipment may have changed from test to test, the overall experimental test setup did not. These commonalities will be addressed below, and will include a brief description of the equipment, the experimental setup, and its overall purpose.

a. WebDAQ/100

The WebDAQ is a data acquisition tool used to capture and record data at specific intervals depending on the settings of its user interface window. It is capable of measuring up to 16 individual channels, accepting variable inputs of up to ±10V. Data collected was stored on an internal flash drive, and could be accessed through a network

connection and saved to a computer. The user interface window was also accessed through a network connection, and allowed the user to optimize each channel individually for the signal which it was measuring. These settings controlled the differential input selection, gain, sampling rate, the number of samples averaged together in each data point, and the report formats. The WebDAQ was used in conjunction with a Python interface program that pulled data directly from the WebDAQ and automatically saved it to the test computer in a Comma-Separated-Value (CSV) format, allowing for subsequent processing and interpretation.

b. ***Dell Computer with Acquisition Software***

Many of the experiments conducted throughout this thesis research had long run times in excess of 24 hrs. These tests typically collected data every second. To accommodate the collection and storage of this data by the WebDAQ, a Dell computer was integrated into the test setup on the test bench. This served two purposes. First, the computer allowed immediate and local access to the WebDAQ interface window, where settings could be adjusted and the acquisition of data started or stopped. Secondly, it was used to store and run the Python data acquisition program, allowing the computer to access the WebDAQ directly, saving the acquired data in real time. This allowed access to and processing of data on the computer, while the WebDAQ could begin another test, significantly reducing the downtime of the WebDAQ due to data retrieval and processing. The WebDAQ could then be run continuously, without interruption for data processing.

c. HP Triple Output Power Supply

The HP triple output power supply was used as the primary power source for the QRS11 rate sensors, as well as many of the other experimental test boards and filters on the test bench. It was capable of providing an accurate supply voltage of up to ±20 V, as well as power return and common ground. For most experiments, the power supply was located next to the test interface bracket, and was connected to the power input pins of the bracket in order to provide ±6 V to the MEMS sensor suite. The power

supply was also used to provide power to test boards during the testing of the voltage regulators and filters. A calibrated multi-meter was used in conjunction with the power supply to verify and adjust the output voltage to within ±1 mV.

d. HP 3478A Calibrated Multi-meter

The primary purpose of the calibrated multi-meter was to verify and adjust the outputs of all other test equipment on the test bench. Due to time and financial constraints, it was not possible to calibrate each piece of test equipment. Instead, it was decided to calibrate only the multi-meter and to then use it to adjust the other pieces of equipment, most importantly the power supplies and signal generators. During experimental testing, the multi-meter was placed on the top shelf of the experimental test bench directly above the other test equipment. When needed, it was connected directly to the outputs of each piece of equipment to adjust and verify the output voltages to within 1 mV. The calibration data can be seen in the table below.

Item	Calibration Date	Notes
5	20 Feb. 2007	100mV=99.9mV. at < 60mV it has a -0.2% error

Table 11. Calibration Table.

e. HP 6218A Power Supply (Signal Generator)

The purpose of the HP 6218A power supply was to generate test signals during specific testing, primarily during the filter testing discussed in Chapter V. In addition, it was also used for powering other equipment as needed. The HP 6218A was capable of providing output signals ranging from 0.5 V to 5 V, and like the triple output power supply, it was adjusted and verified using the calibrated multi-meter to within ±1 mV.

f. Agilent Infiniium Digital Spectrum Analyzer

The Agilent Digital Spectrum Analyzer was another piece of data acquisition equipment. Unlike the WebDAQ, the spectrum analyzer is capable of making

precise measurements at sampling rates as high as one Giga-sample per second. This allowed the Agilent to achieve exceptional measurement resolution at the lowest of signal outputs. The Agilent was capable of measuring and displaying up to four individual channels at the same time. Each of these channels could be individually adjusted based on the signal characteristics. Data could be stored internally or saved directly to a flash drive via a USB port. The latter allowed for the transfer of data to the Dell computer for processing. A key feature of the Agilent was its comprehensive library of mathematical analysis functions, which was extremely useful during the calculation of signal Fast Fourier Transforms (FFT) of various signals. The ability of the Agilent scope to display these FFTs on the same screen as the reference signal made experimentation much more efficient.

g. Digital Multi-meter(s)

Although the calibrated multi-meter was often used to verify the accuracy and adjust the other test equipment, it was not the easiest piece of equipment to move around. Thus, it was often more feasible to use a much smaller, hand held multi-meter for many of the more routine measurements. The Micronta and Radio Shack auto-range digital multi-meters used in this research were not calibrated, but when compared to the calibrated multi-meter, they were shown to have an error of less than 1 mV. The digital multi-meters were used for many of the stopgap verifications during experimental setup, specifically for monitoring the MEMS sensor's BIT output for many of the tests, as well as measuring and verifying component values during the build of the PCFBs discussed in Chapter V.

h. Tektronix TDS 3012B Oscilloscope

Although the Agilent Digital Spectrum Analyzer was capable of making very precise measurements, it was not the most user-friendly piece of equipment in the lab. It was complex and required more than a little time to setup. Thus, it was sometimes simpler to use the smaller Tektronix oscilloscope when making measurements where high sampling rates and high precision were not required. This scope had the additional

capability of being able to make simultaneous measurements in conjunction with the Agilent scope. This gave a significant amount of flexibility to the ways data could be captured.

i. HAAS TRT-7 2-Axis Tilt and Rotation Table (TRT)

The HAAS TRT was the primary test platform on which the experiments were conducted, except those requiring the TVC. The table and its control panel were capable of providing very precise angular rates in both the rotational axis, as well as the tilt axis. Although the table was used for only a fraction of the experiments to provide angular rates other than zero, the table was used throughout this research to provide a flat, secure, and stable platform for mounting the MEMS sensor.

j. Thermal Vacuum Chamber

The TVC was the only piece of test equipment not moved to the solar lab. When thermal testing was conducted in the TVC, all required test equipment was moved into the satellite lab, and set up on another test bench located directly in front of the TVC. The TVC is capable of reaching a vacuum state of 10 E-6 Torr, and has a thermal range of -70°C to +100°C. It was primarily used during the collection of bias vs. temperature data during the formulation of the bias compensation values as discussed in Chapter IV. All efforts were made to ensure that the experimental test setup at each location remained as identical as possible. Even so, some modifications to both the internal and external wiring harnesses of the chamber were required between the thermal vacuum chamber and the test interface bracket.

C. INTERFACE AND HARDWARE BUILD

Test hardware needed to be constructed prior to testing and characterization of the sensor. This hardware includes the test MEMS subsystem itself, a flight-like wiring harness, and the test interface bracket which would connect all test hardware to the test equipment. Great effort was made in each of these builds to ensure that the test hardware remained as flight-like as possible.

1. MEMS Test Build

The test MEMS assembly was built in accordance with the MEMS Build Procedures attached in Annex B. Other than the use of flight sensors, flight hardware, or flight PCFBs, the assembly was built as closely as possible to the actual flight unit. Variations from the flight build include the use of a single QRS11 test sensor rather than the tri-axial set of flight sensors, as well as the use of a non-flight base plate and housing. These components were locally fabricated, built to the same specifications as the flight components. In addition, no voltage regulators or filter boards were used to simulate the PCFBs, and the sensor was wired directly to the 13-Pin connector with the use of a QRS11 compatible 10-Pin connector.

The design of some of this flight hardware would change as a result of further experimental research and testing, as well as the build of the MEMS Test assembly. These hardware changes were purely structural and would have no effect on the application of the experimental findings towards the build of the flight unit. The changes to the MEMS Test Build were systematic improvements of the sensor through testing which addressed the ongoing characterization and improvements of the sensor. In this thesis, there were 5 such configurations: 1) Single sensor, wires only. 2) Single sensor, PRCB. 3) Single sensor, breadboard PCFB. 4) Single sensor, internal PCFB. 5) Three flight sensors, three flight PCFBs. These changes are incorporated later at the final flight build of the hardware. The test MEMS assembly configuration 1 can be seen below with the housing removed.

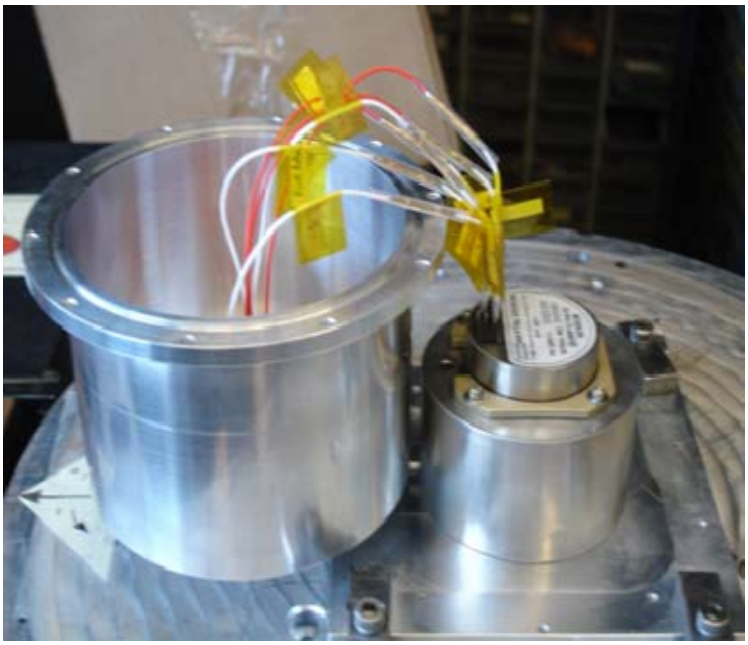

Figure 7. MEMS Test Assembly (Configuration 1).

2. Wiring Harness Build

To connect the MEMS test sensor to the test interface bracket, a flight-like wiring harness was constructed. To gain the maximum utility from the build of this harness, the Wiring Harness Build Procedures in Annex A were used and validated during the build. Utilization of a flight-like harness for testing served two purposes. First, it gave the builder practice in the construction techniques required for the build of the flight wiring harness, allowing the builder yet another opportunity to trouble shoot and optimize the build procedures. Secondly, it ensured that the data gained from the experimental tests would be flight-like.

It is important to note here that this test harness was built in accordance with what was known of the sensor when this research began. Therefore, it was not the most optimal configuration, and would not incorporate the lessons learned from the experimentation conducted in this thesis. Later, in response to these lessons learned, the Wiring Harness Build Procedures would be re-written and updated to incorporate these changes, and are what is now currently seen in Annex A. These incorporated some significant changes from the original wiring harness build.

First, the original test harness did not bring out the temperature outputs from each sensor. Chapter IV will show that temperature has a significant impact on the observed bias of each sensor's rate output, and would be needed to achieve accurate rate outputs. To account for this, a secondary harness would later be incorporated in parallel with the test harness to bring temperature out from the sensor. Secondly, the test harness was not optimized for ease of integration into the spacecraft or the construction. Simply put, the original construction of the harness was physically difficult to integrate into the spacecraft, and was very difficult to construct. To address this, roughly ten changes were made to the build procedures of the wiring harness.

These included shortening the connector back shells to allow more clearance in the spacecraft, wire pairing to reduce the amount of wire in the harness, optimizing connector pin layout making it easier to insert pins from twisted pairs, common grounding techniques that again reduced the number of wires in the harness, and in the changing from solder to crimp pins. All these changes made both the construction as well as the integration of the harness into the spacecraft much easier. A picture of the test harness can be seen below.

Figure 8. Test Harness.

3. Test Interface Bracket Build

For the experimental test equipment to interface with the MEMS and its wiring harness, a test interface bracket was built. This bracket served two purposes. First, it would give the 15-Pin connector of the wiring harness a stable mounting point on the experimental test bench, simulating the connection it would make with the ACS on the spacecraft. Secondly, it would serve as an intermediate wiring harness, allowing easy access to the 15 leads of the wiring harness to make it easier to interface with and route each signal to its respective location in the measurement equipment. A 15-Pin female connector was mounted to the test interface bracket to simulate the ACS connector. 15 wires were cut, three power leads at 12', and 12 output leads at 4'. These wires were crimped with both a male and a female pin, and labeled with their respective signals. The female end of each of these 15 wires was then inserted into the female 15-Pin connector of the test interface bracket according to the 15-Pin Connector diagram seen in Annex 1. The male ends were left free to connect to the WebDAQ and the power supply at a later time. The test interface bracket can be seen below.

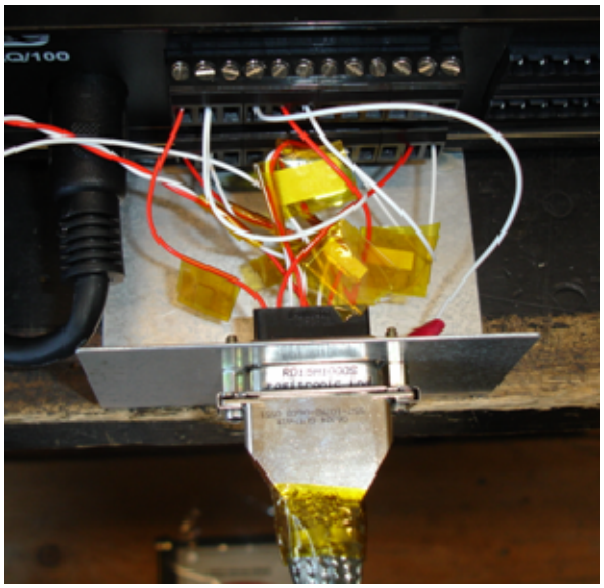

Figure 9. Test Interface Bracket Picture (no WebDAQ).

D. TEST BENCH EXPERIMENTAL SETUP

Once the experimental test equipment was present and the required test hardware and interfacing hardware was built, the experimental test bench was setup in preparation for testing. To establish an efficient and operational test bench setup and to reduce noise pickup from the unshielded wires it is important to minimize the exposed wire. Simply put, to reduce noise in the system the exposed wires needed to be kept as short as possible. To do this the test interface bracket was mounted to the center of the experimental test bench with a C clamp. This bracket would serve as the focal point for the experimental test bench setup, allowing the key pieces of equipment to be positioned near it, minimizing the amount of wire needed to connect them. The experimental test bench setup can be seen below in Figure 10.

Figure 10. Experimental Test Setup Picture.

The HAAS TRT was positioned beneath the experimental test bench, directly beneath the test interface bracket. It was then turned to align its central axis (Tilt) with

true north. A compass and the local declination-constant of 14° 13' E were used to verify this alignment to within a few degrees. When needed, the tilt of the table would be elevated 36.6° to account for the latitude of NPS, truly aligning the sense axis of the sensors with the earth rotation vector. The tables rotational rate accuracy was then verified using a stopwatch and known orientation markings on the device. Three separate rates were verified over a complete rotation, verifying the relative accuracy of the rotational table.

The MEMS test sensor was then mounted to the table, ensuring that the orientation of the –X axis was aligned with the orientation of the zero position of the rotational table. The test wiring harness was then attached, connecting the MEMS to the test interface bracket. Placing the table in this position allowed enough slack in the wiring harness to conduct large rotational and tilt movements without straining the connectors of either the test interface bracket or the wiring harness. The control box of the HAAS TRT was placed on the far left side of the experimental test bench.

The WebDAQ is a measurement sensor and thus it represents a large potential source for induced noise. Its 16 channels directly interface with 12 of the 15 outputs from the test interface bracket as seen in Figure 13, and these interfaces are vulnerable to induced noise. These interfaces include the three output signals from each of the three sensors as well as the signal ground, for a total of twelve connections. To minimize potential for inducing noise here, the WebDAQ was placed on the test bench directly behind the test interface bracket, as close as possible. It was then connected to the network via a LAN cable, and powered by an Uninterruptible Power Supply (UPS) to negate test interruption due to sporadic power fluctuations and outages in the building.

The next most important piece of test equipment is the HP Triple Output Power Supply. It directly interfaces with the remaining three leads from the test interface bracket, and also needs to be placed as close to the test interface bracket as possible. Like the WebDAQ, the length of the leads to the power supply need to be minimized as much as possible to reduce the potential for any induced noise along the exposed wires. For this reason, the power supply was placed on the test bench directly behind the test interface bracket, immediate to the left of the WebDAQ, and as close as possible, and

powered by the UPS. The remaining test equipment has shielded leads and probes of a fixed length. Therefore, this equipment can be placed in any location desired as length of the probes allow. For the purpose of this research, we selected an experimental setup that was conducive to the methodical and repetitive capture of data, over long periods of time. This setup is described below.

The calibrated multimeter was placed on the top shelf of the test bench, above the center of the experimental test bench. It was positioned so that its leads were capable of reaching all the other pieces of test equipment. This would allow it to be able to verify the output signals of every other piece of test equipment on the test bench without moving it. Its leads were connected to the output ports of the triple output power supply for the majority of all testing to verify the output voltage, and its power cord was plugged into the UPS.

The Agilent Digital Spectrum Analyzer was then placed on the experimental test bench, behind and to the left of the WebDAQ and the Triple Output Power Supply. Its four foot probes were easily able to reach the test interface bracket. A USB port extension cable was plugged into the USB port on its back, and routed to the front for easy access during testing. Its power cord was plugged into the UPS. During the characterization of the Agilent scope, we learned that its standard probes were inducing a large amount of noise, often above 35 mV. Therefore, “low-noise” probes were used for the remainder of the research.

The Dell computer and monitor were set up on the far right side of the experimental test bench. Because the computer was not directly interfaced into any of the test equipment it was not required on the experimental test bench, yet having it close to the experimental setup had many advantages. First, it was far easier to be able access the WebDAQ at the test bench, where you could trouble shoot, set up, start, and stop experimental tests. Likewise, to start a test, the Python interfacing program would need to be started from the computer. Having the ability to do this on the experimental test bench was far more efficient than running back and forth between test bench and desk computer trying to get a test to run. Also, having the computer on the test bench made it possible to process experimental data while conducting further testing. The computer

was connected to the network via the internet, and powered by the UPS. The Tektronix scope was also placed on the top shelf of the test bench to the right side of the calibrated multi-meter, above the center of the experimental test bench. Its four foot ft probes were easily able to reach the test interface bracket.

E. WEBDAQ VERIFICATION, WIRING, AND SETUP

With the experimental test bench set up, and all equipment operational, it is now time to prepare the WebDAQ for operation. Prior to integrating the WebDAQ into the test bench set up, we first needed to verify that the WebDAQ will perform as we expect it to, and that it is capable of accurately measuring output rates. Once this is complete, we will then be able to connect the WebDAQ to the test interface bracket and set up the WebDAQ user interface in preparation for our testing.

1. WebDAQ Accuracy Verification

To ensure that the data obtained from the WebDAQ is accurate enough, a simple test was conducted to confirm and characterize the WebDAQ's ability to measure and record voltages. To do this the HP 6218A Power Supply was used to serve as a signal generator, and was connected differentially to the WebDAQ test channel. For this test, channel 8 was selected. The calibrated multi-meter was attached to the power supply to precisely tune the output voltage of the power supply to the desired voltages as seen below in Table 12. The WebDAQ was turned on, and the measurements were taken at 13 different voltage levels across the operational spectrum of the MEMS sensors. These measurements were recorded and referenced to the calibrated power supply in the table below, and comparisons were made between the supplied voltage and the WebDAQ recorded measurements. The results are shown in Table 12.

Power Supply (V)	Cal. Multi-meter (V)	WebDAQ (V)	Δ Voltage (mV)	Δ %
6.00	5.995	5.995	0	0.00
5.00	4.993	4.994	1	0.03
4.00	4.000	4.000	0	0.00
3.00	2.999	2.999	0	0.00
2.00	2.001	2.001	0	0.00
1.00	1.004	1.003	1	0.10
0.50	0.505	0.504	1	0.19
0.40	0.410	0.409	1	0.25
0.20	0.205	0.205	0	0.00
0.10	0.103	0.103	0	0.00
0.05	0.056	0.056	0	0.00
0.01	0.013	0.013	0	0.00
0.00	0.005	0.005	0	0.00

Table 12. WEBDAQ Accuracy Verification.

From this data, we were able to determine the maximum voltage differential between the calibrated voltage output and the recorded WebDAQ data, and recorded this differential in Table 12. From this, it was determined that the maximum error between the calibrated power supply voltage and the WebDAQ measurements was 1 mV at 0.5 V, with an average error of only 0.00029V (0.3 mV). For the purposes of this thesis research this is well within the needs of the experimental measurements, which is based on the both the manufactures worst-case resolution of 2 mV, as well as our desire to make measurements at suborbital rates of approximately 1/20 orbital rate, or 3 mV [25]. Thus the WebDAQ more then meets our accuracy requirements for this thesis research.

Similarly to the test performed above, further verification testing was performed to prove that all nine of the channels being used on the WebDAQ performed similarly to test channel eight results seen above. For this test, three different voltages were used as a representative sampling for the above test. These voltages were +5V, 0V, -5V, and the calibrated input voltage (In) are shown compared to the measured output voltages (Out) for each voltage below in Table 13. These data points represent a single measurement (not averaged).

Channel	In (+5V)	Out (+5V)	In (0V)	Out (0V)	In (-5V)	Out (-5V)	Aver. Δ (mV)
1	5.053	5.054	0.008	0.009	-5.085	-5.085	0.7
2	5.087	5.089	0.007	0.009	-5.085	-5.087	2.0
3	4.994	4.995	0.008	0.009	-5.061	-5.062	1.0
4	5.061	5.062	0.008	0.009	-5.060	-5.062	1.3
5	5.019	5.018	0.007	0.007	-5.034	-5.038	1.7
6	5.034	5.033	0.006	0.005	-4.921	-4.922	1.0
7	4.935	4.935	0.007	0.007	-5.039	-5.042	1.0
13	4.996	4.996	0.007	0.007	-5.016	-5.018	0.7
14	5.015	5.016	0.012	0.012	-5.016	-5.018	1.0

Table 13. Channel Comparison Table.

From this data, we were able to determine that all channels used in the WebDAQ do indeed perform very similarly. It was determined that without averaging, the maximum error per WebDAQ channel was 2 mV, with an average error for all channels of 1.3 mV. At rate voltages nearing 0 V this would equate to a maximum potential error in rate of 22%. This error quickly decreases as the rates increase and with data averaging. Again, for the purposes of this thesis research this level of error is well within the needs of the measurements.

2. WebDAQ Wiring (Original)

Once the WebDAQ was determined to be capable of meeting the required measurement fidelity, it was integrated into the experimental test set up. It is important to note here that the experimental setup and wiring of the WebDAQ went through a series of changes during the course of this research. These changes stemmed from insights gained into the characterization and from understanding of the sensors during the research. As a result, operational and design changes were made to the MEMS sensors and wiring harness.

The WebDAQ wiring setup seen in this section represents the setup used during early research conducted with the MEMS sensor, and was based on its design and operational plan at the time this research began. The setup you see below was the starting point, with research driving the many changes that would come before better understanding and characterization of the sensor was possible.

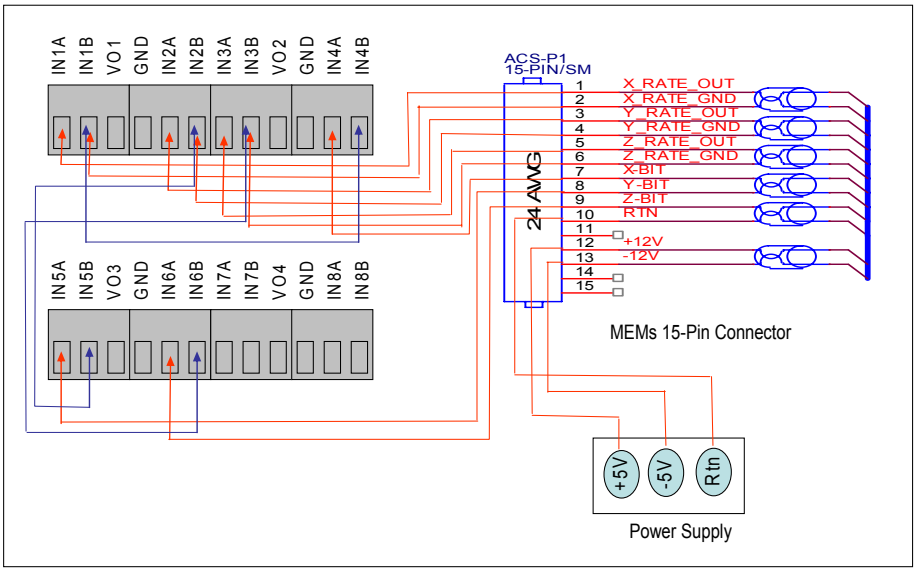

Figure 11. Original WebDAQ Wiring Schematic.

As shown in Figure 11, the original experimental setup did not bring out temperature output from the QRS11 sensors. Later it was realized that temperature plays a critical role in understanding and characterizing the sensor. In response to this, the WebDAQ wiring setup was altered through the addition of an external thermistor circuit based on a standard design used for the NPSAT1 battery monitoring and testing [5]. This circuit can be seen below in Figure 12.

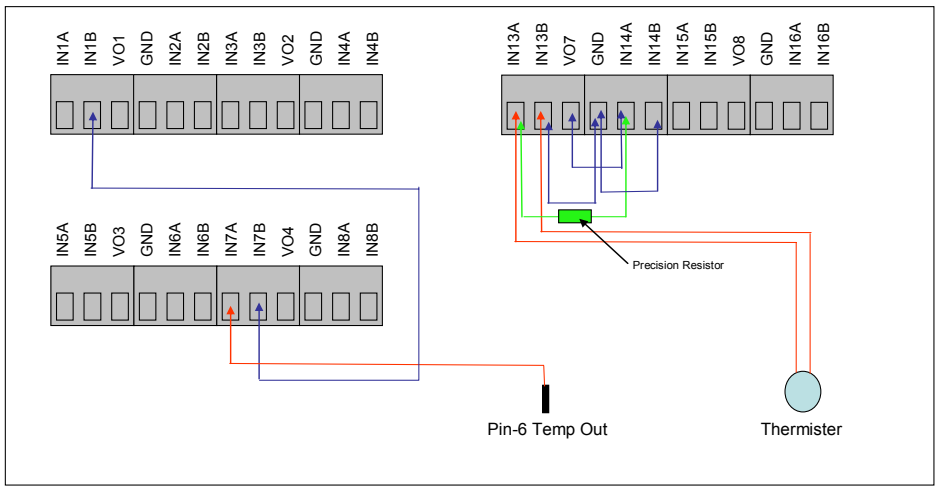

Figure 12. WEBDAQ Wiring Diagram (Thermal).

The MEMS rate sensor is constructed with internal circuitry that provides a voltage output related to temperature for use as a calibration tool. This output is located on pin 6 of the QRS11, and was not expected to be used as the manufacturer indicated that they believed no further improvement in accuracy was possible by including temperature [26]. With the discovery of the dependence of bias on temperature, this output needs to be integrated into the MEMS rate measurement system, including its wiring harness, and the operational plan for the sensor suite in whole would need to be looked at again. To utilize this internal temperature circuitry, it would first need to be calibrated and understood. The thermistor circuit seen above (Figure 12 Right) was used to do this, and integrated into the established WebDAQ wiring diagram seen in Figure 11. A temperature output harness was also integrated (Figure 12 Left), connecting the sensor temperature output into an open channel of the WebDAQ. Eventually, the MEMS flight-unit build procedures, the wiring harness build procedures, and the ACS interface connectors were all updated to enable collection of temperature along with rate data. The final wiring setup can be seen in Figure 13 of the next section, and was used for most of the research presented in Chapters V and VI.

3. WebDAQ Wiring (Updated)

After the understanding gained through the research conducted in Chapter IV, a final WebDAQ wiring setup was obtained. This setup allowed for all relevant outputs from the sensor, and directly interfaced with the newly re-designed wiring harness. To do this the 15 leads of the test interface bracket were attached to their respective locations in the WebDAQ as well as the triple output power supply. In addition to these leads, six wire jumpers were used to daisy chain the reference signal ground from each of the three sensors rates to their respective temperature and BIT outputs as well. This connection diagram can be seen below in Figure 13.

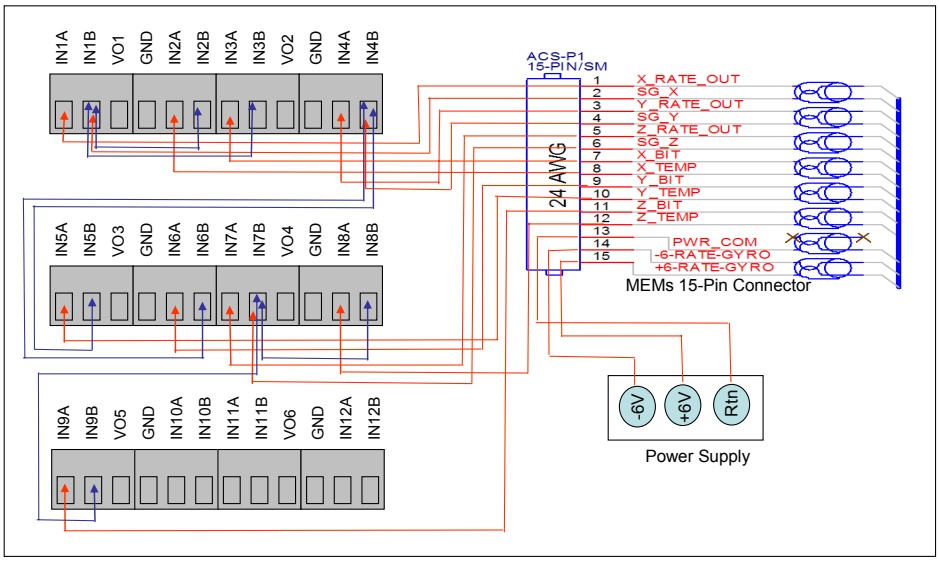

Figure 13. WEBDAQ Wiring Diagram.

It is important to note here that every precaution was taken when attaching these leads. Not only can crossed wires cause inaccurate results, they can also possibly cause damage to the sensors. To avoid this, leads were attached in order, a single sensor axis at a time, ensuring that all leads were properly seated and secured, ensuring that they were not touching, prior to connecting the next set of leads. The complete interface can be seen in Figure 14.

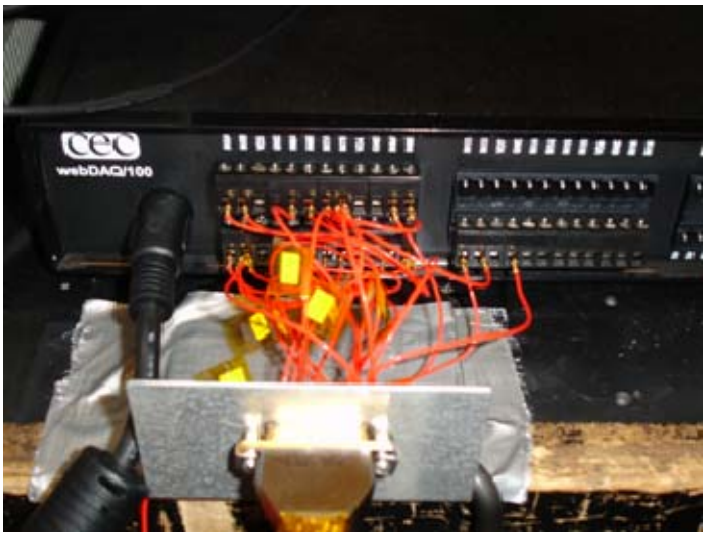

Figure 14. WebDAQ and Test Bracket Interface Picture.

4. WebDAQ User Interface Setup

With the WebDAQ successfully integrated into the experimental test set up, it was now time to assign the various channels of the WebDAQ to their respective outputs and set them to appropriate values for testing. The WebDAQs user interface is only accessible through a network. For the purposes of this research, the WebDAQ was inserted into the local network, and assigned a local IP address. Using the FireFox browser, we connected to the WebDAQ and its user interface window screen was opened, and can be seen below in Figure 15. It is important to note that most common browsers can be used to connect to the WebDAQ, and that user preference was the only factor in the selection of the FireFox browser over other browsers.

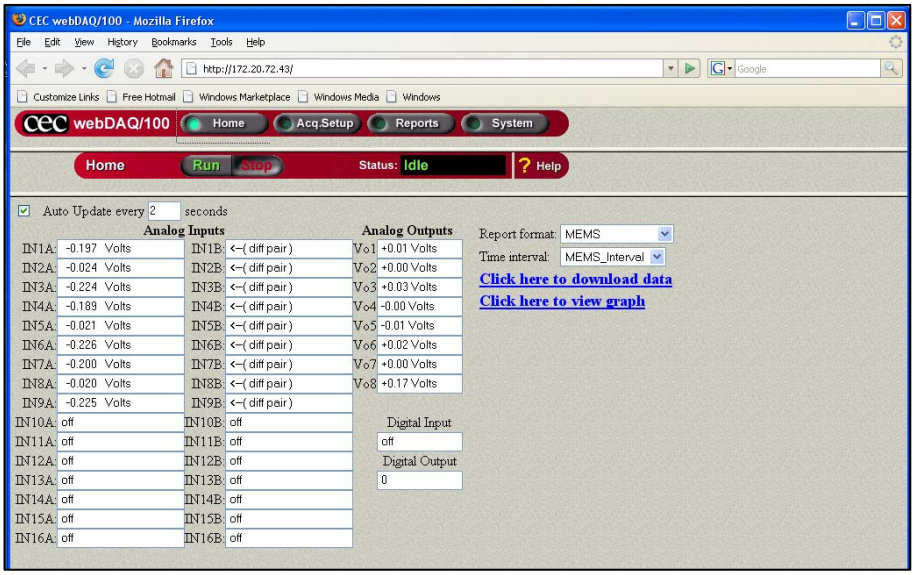

Figure 15. WebDAQ Interface Window.

Figure 15 shows the WebDAQ user interface window. Here, active channels and current test data are displayed, and tests can be started and stopped. To make changes to the method in which this data is being captured, or the organization and setup of each individual channel, the test must be stopped, and the Acquisition Setup tab opened. This user interface can be seen below in Figure 16.

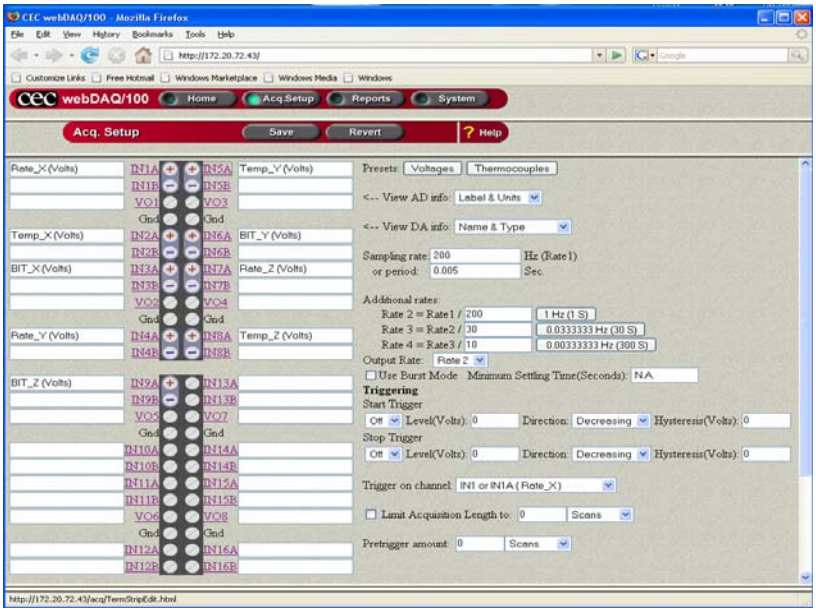

Figure 16. WebDAQ Acquisition Window .

This window allows changes to be made to the sampling rate, as well as the reference rate for the output rates. For the majority of the testing conducted during this research, the normal sampling rate was either 1000 Hz for high fidelity testing, or 200 Hz for flight simulation. Rate 2 was the standard output reference for all testing. This ensured that data output would be as close to the desired frequency as possible, which was typically once every second for short tests, and once every thirty seconds for long duration tests.

To provide accurate readings, we must ensure that the data acquisition system is properly set up, and that all interfaces are properly connected. To do this, each channel being used needed to be set individually to the appropriate settings. This was done by clicking on the appropriate channel; for example, selecting channel IN1A opens the channel settings interface window seen below in Figure 17.

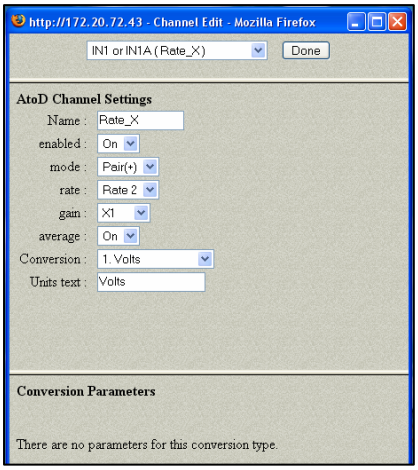

Figure 17. Channel Settings Window.

This interface allows the user to turn on a specific channel and to assign it a name to match its input, change the input type, single or differential pair, assign it a reference rate for outputs, set a gain, turn on averaging, and assign a unit of measure. This was completed for all nine active signals from the MEMS, a rate, BIT, and temperature for each of the three sensors.

F. PYTHON PROGRAMMING AND SOFTWARE SETUP

The python code used to pull data from the WebDAQ and save it to the computer in a predetermined and easily processed format was originally written for the testing of the NPSAT1 flight battery cells [3]. Our measurements were very different from the data being collected on the batteries, therefore, modifications to this code were made in order to meet the needs of the experimental testing. Later on, as the complexity of the experimental testing grew, more modifications were made to incorporate MEMS temperature output data as well as thermistor temperature data. These two individual subroutines would eventually be consolidated into a single, coherent program used to gather experimental data and save it in a usable form for data processing. The finalized code used for all bench testing of the MEMS 3-axis rate sensor can be found in Appendix C.

G. HAAS ROTATION AND TILT TABLE SET UP AND PROCEDURES

As stated earlier, the HAAS TRT was used primarily as a stable platform from which much of the experimentation of the MEMS sensors was conducted. Later, as issues with bias and noise were addressed and compensated for, we began using the table to provide precise rotational rates to test and characterize the sensor under controlled rates. Use of the equipment is fairly straight forward, though the User's Guide is indispensable [27]. For the purpose of this research, amended versions of the procedures were used. These procedures can be seen below in Table 14, and were used for all experiments requiring the HAAS TRT.

1	Power on the HAAS 2-Axis Rotation Table Controller.
2	Press the start button 1 time. This will give the current table position.
3	Ensure the table is properly aligned, and that the tilt and rotation table markers are in line with the reference markers. Press and hold the CLR button for 3 sec.
4	Press the right arrow button, then press and hold the CLR button for 3 sec. This stores the home position of the tilt and rotation table.
5	Press the mode button, verify or enter 91, then press the right arrow button. This puts the system in relative mode. All motion will reference the last position.
6	Enter the tilt angle in degrees, and then press the right arrow.
7	Enter the rotation angle in degrees, and then press the right arrow.
8	Enter the rate in °/s, and then press the right arrow.
9	Press the mode button to finish the program.
10	When ready, press the start button to begin the program. The program will end after the specified movements have been completed. In this mode, all future movements will be from this position.

Table 14. HAAS Start Up and Operations Procedures.

H. THERMAL VACUUM CHAMBER SET UP AND PROCEDURES

The TVC was used for the majority of the bias vs. temperature testing. Although initial temperature testing was done utilizing a cooling plate, tank, pump, and reservoir, the temperature range obtained with this equipment was less than what we were expecting on orbit. Therefore, we decided to move the experimental test setup downstairs, and integrate the experimental setup into the TVC. The necessary equipment was setup on an alternate test bench located next to the TVC in nearly the same manner as was in the solar lab. To successfully interface the MEMS wiring harness with the TVC, two intermediate wiring harnesses were constructed, allowing the internal harness of the chamber to connect with the MEMS wiring harness, as well as an external chamber

harness to connect to the test interface bracket. Before doing this, all fifty pins of the internal chamber wiring harness were traced using a multi-meter to determine which pins from the two external connectors would need to be routed to the test interface bracket connector. These intermediate harnesses can be seen below.

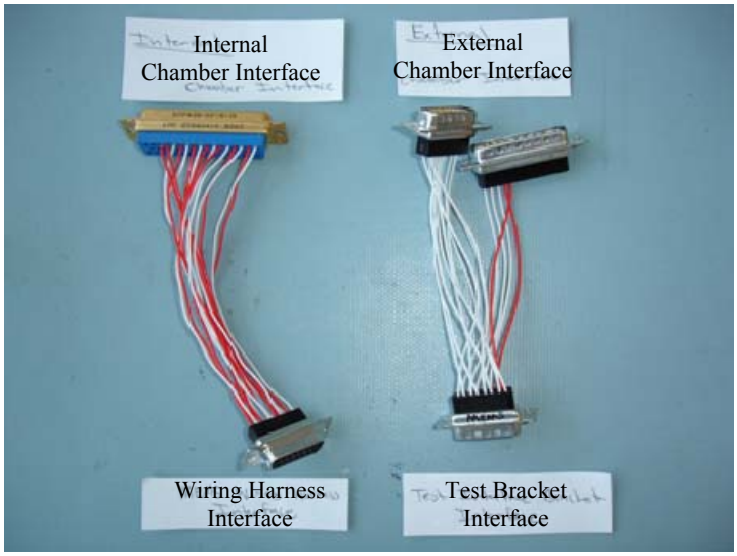

Figure 18. Intermediate Wiring Harnesses.

Once these harnesses were connected, the MEMS assembly and the wiring harness were placed inside the thermal vacuum chamber, and connected to the intermediate wiring harness. Two thermocouples were placed on the top surface of the MEMS housing and under the MEMS base plate. These thermocouples are used to track the thermal gradient of the TVC and help determine when the MEMS sensors had reached the desired temperature. The external intermediate wiring harness was then connected to the test interface bracket. This setup is shown in Figure 19.

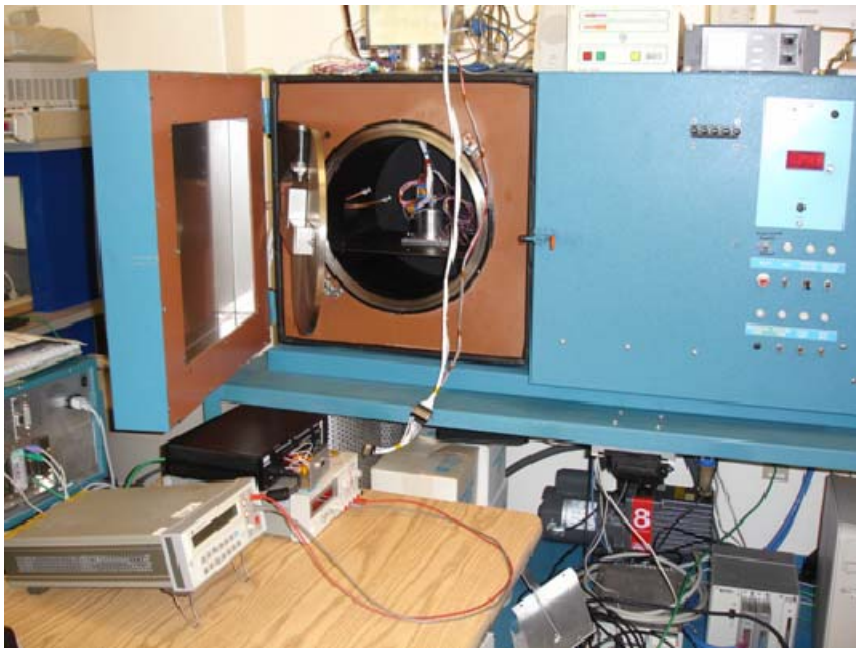

Figure 19. Thermal Vacuum Experimental Setup.

Once the WebDAQ connection was verified, a simple connectivity test was conducted to verify that the WebDAQ was operational, and that the MEMS assembly was operational and interfacing with the WebDAQ properly. Once this was verified, the door of the chamber was closed and sealed, and the procedures in Table 15 were executed to prepare and test with the TVC. Note, steps 3 through 13 only need to be performed once every time the chamber door is closed and sealed, otherwise these steps can be skipped.

1	Switch on the power strip underneath the TVC.
2	Set the power switch located on the front panel of the TVC to the on position.
3	Record the internal pressure measurement as displayed on the pressure panel above the TVC. This will be used later when equalizing the chamber pressure.
4	Close the pressure release valve on the lower right face of the chamber. This will allow the vacuum to purge the TVC.
5	Turn on the vacuum pump located underneath the chamber, and wait for the internal pressure to drop below 1.0 E0 Torr. This will take only a few minutes
6	Turn both Nitrogen tank valves to the on position, then open the pressure release valve on the TVC. This will allow Nitrogen to flow into the TVC.
7	Allow this to run until the pressure in the TVC rises back to around 3.0 E2 Torr. This will take about a minute. Repeat steps 4-7 twice.
10	Turn off the vacuum pump, and allow the Nitrogen to continue to flow into the TVC until the pressure reaches the value recorded in step 3. Close all valves.
12	Open the pressure release valve slightly. This will allow the TVC to completely equalize. This will ensure the TVC door opens later when access is needed.
13	Set the desired temperature with the turn knob on the center face of the panel. To do this, press the knob in, and then rotate.
14	Switch on either the ambient cooling or the heating switch as desired. Sub zero cooling can also be used, but careful monitoring of temperature is needed.
15	Monitor the internal temperatures, cycling the cooling/heating switches on and off, until MEMS base plate thermal couple saturates to the desired temperature.
16	Switch off heating/cooling switch, power off master switch, turn off power strip. Turning off all power will remove the ambient noise of the TVC prior to testing.
17	Start WebDAQ data acquisition, and start the Python Program.

Table 15. Thermal Vacuum Chamber Start Up and Operation Procedures.

It is important to note here that the thermal vacuum chamber has two important features that must be addressed to maximize the utility of the equipment. Firstly, the temperature set function of the chamber only works for the heating cycle. When heating, the chamber will control its internal temperature to match the set temperature. This is not the case for cooling. The chamber will continue to cool while turned on. Therefore, care needs to be taken during cooling cycles, and depending on the time required for the QRS11 sensors to reach temperature, numerous on/off cycles may be needed to ensure that the chamber does not exceed the lower operational temperature of the sensor.

Secondly, when in operation, the chamber is very noisy. Its pumps and fans induced a great deal of vibration in the TVC, especially during cooling. It was discovered that when performing thermal vacuum testing it was best to cycle the chamber to the desired temperature, giving it adequate time to allow the QRS11 sensors to reach the desired temperature. Once achieved, shut off all power to the TVC, including the

power strip, and then begin the testing. This provided a vibration and noise free environment in which to capture bias vs. temperature data.

THIS PAGE INTENTIONALLY LEFT BLANK

IV. EXPERIMENTAL RESEARCH AND TESTING

A. INTRODUCTION

The research presented in this chapter systematically steps the reader along the path of research undertaken with respect to the experimentation conducted on the MEMS rate sensors as we attempted to understand and characterize the operations and capabilities of the sensor. Several hundred individual tests were conducted over the eight months that this research was conducted, with some of these tests ranging in lengths of only a few seconds, while others ran as long as three days. Only relevant data is presented in this thesis, the presentation of which will forego many of the experimental pitfalls encountered, as well as the majority of the repetitive validation testing.

1. Assumptions

The MEMS experiment is just that, an experiment. Thus, a limited amount of effort and research was put into understanding the sensor's capabilities prior to its selection. At that time it was believed that the sensor was only capable of accurately measuring rates as low as 0.5°/s at best. While this had some applications for use at higher tip-off rates, it was assumed that the MEMS sensors would yield unreliable rates when approaching orbital rates and nothing of use below orbital rate. Unfortunately, it was at these rates that the spacecraft would spend almost its entire lifetime and where the MEMS could be the most useful. This thesis research began with the notion that this assumption was wrong and the remainder of this thesis will focus on proving that the QRS11 MEMS angular rate sensor is far more capable than was commonly believed.

2. Error Methodology

As with any electronic sensor, output data can only be as accurate as the inherent error of the system. Unfortunately, other than the basic knowledge of MEMS sensors as a whole, there was very little knowledge of these error types for the QRS11. From the manufacturer, two possible types of error were suggested, and that was in bias and noise [25]. While some suggestions were made to attempt to compensate for these errors,

namely through voltage regulation, reduction of grounding loops, and possible filtering, these suggestions were aimed at minimizing errors at higher operational rates. For the QRS11 these operational rates vary from ±5°/s to as much as ±1000°/s. At these higher rates, precision requirements are far lower than would be needed to achieve the precision needed to measure rates near orbital rate, roughly 0.066°/s. Therefore, a much more detailed investigation into these potential errors will be required in order to maximize the utility of the sensor. To do this, we must first understand the sources of error and then apply techniques to compensate for them.

a. Bias

Bias can be defined as a wide range of potential input errors that result in a signal shift away from the true output of the signal. A sensor with a large bias, say 10 units, will output a signal ten units from the true value of the signal. To achieve the true output value, this bias will need to be understood and then compensated for. Possible bias-inducing-errors include structural vibration, incorrect mounting and mounting vibration, environmental conditions, signal and power grounding errors, as well as sensor cross talk. Each of these potential sources will have very specific characteristics and impact on the overall bias of the signal. A solid understanding of the operations of the sensor is needed to delineate which sources need to be addressed.

b. Noise

Noise can be defined as a wide range of potential errors that result in a random divergence from the absolute output of the signal. This can best be described as the deviation of the recorded signal from the average signal value. A sensor with more noise in the system will be observed to have a far larger range of output than a sensor with no noise. While noise can be significantly reduced through appropriate sampling rates and averaging over longer time periods, this technique is often undesirable for many sensors due to measurement requirements. For these types of sensors it becomes very important to reduce all possible sources of noise prior to sampling and averaging. Possible noise sources include power quality, manufacturing artifacts and sensor internal

errors, external radiation sources, signal and power grounding errors, measurement equipment and interface errors, and external vibration, which would be measured as rates by the sensors. Each of these potential sources will have specific characteristics and impact on the overall noise of the signal. A solid understanding of the operations of the sensor is needed to delineate which sources need to be addressed.

B. TESTING

With the experimental setup described in Chapter III complete and a MEMS test unit ready for testing, it was decided that the initial testing should focus on gaining a better understanding of the basic operation of the MEMS sensor during both startup and normal operations. Of particular interest would be the effects of bias on the output signal. These tests were designed to get a better understanding of the test environment, and to do some initial characterization of the sensor.

Before testing was started, it was determined that the first thing we needed to do was to determine the "recommended" sampling rate of the spacecraft ACS, and thus the sampling rate we would use in the WebDAQ. To determine this, a series of tests was conducted at sampling rates varying from 10 Hz to 1000 Hz. These tests ran 10 minutes each, and the data was sampled at the specified rate, and standard deviations were calculated. What we saw was that at sampling rates from 300 Hz to 1000 Hz, the standard deviations remained fairly constant at $\sigma = 1.5$ mV. At 200 Hz, we began to see an increase in standard deviation, and observed $\sigma = 1.6$ mV. Below 200 Hz, the observed standard deviations quickly increased. At 60 Hz σ was observed to be 2.9 mV, while a σ of 5.4 mV was seen at 20 Hz. To minimize the standard deviation, and therefore maximize the accuracy of measurements, a sampling rate between 60 Hz and 300 Hz should be selected. Experimentally, we were concerned with accuracy, but the ACS design team wanted to keep the sampling rate as low as possible to free up bandwidth for other measurements [3]. For the purpose of this thesis, a compromise was made between the desire for accuracy and the needs of the ACS design team, and 200 Hz was selected as the sampling rate of the ACS. Further testing with the flight unit once completed should be performed to determine the exact sampling rate for use on orbit.

1. Startup Profile and Short Term Bias Testing

The first few tests conducted were simple start up tests, where the WebDAQ and Python acquisition systems were started prior to powering the MEMS test unit. This allowed us to capture the outputs of the rate sensor during power up and allowed us to characterize the sensor output as it reached an operational state. The sensor output was sampled at 200 Hz, with averaged data reported every one second. The lengths of the test varied from 60 sec to 240 seconds, and the supply power for the sensor was set at +5.15 V and -5.00 V. Due to an early misunderstanding on the advantages of differential power input, many of the initial tests used this upper limit of acceptability as the supply input. Later, this differential voltage would be adjusted to a more consistent and manageable voltage would be used. To begin this test, the WebDAQ and Python acquisition program were set to gather 90 seconds of data, and then started. After five seconds, the MEMS test sensor was powered on, and the rate output start up profile gathered by the WebDAQ can be seen below.

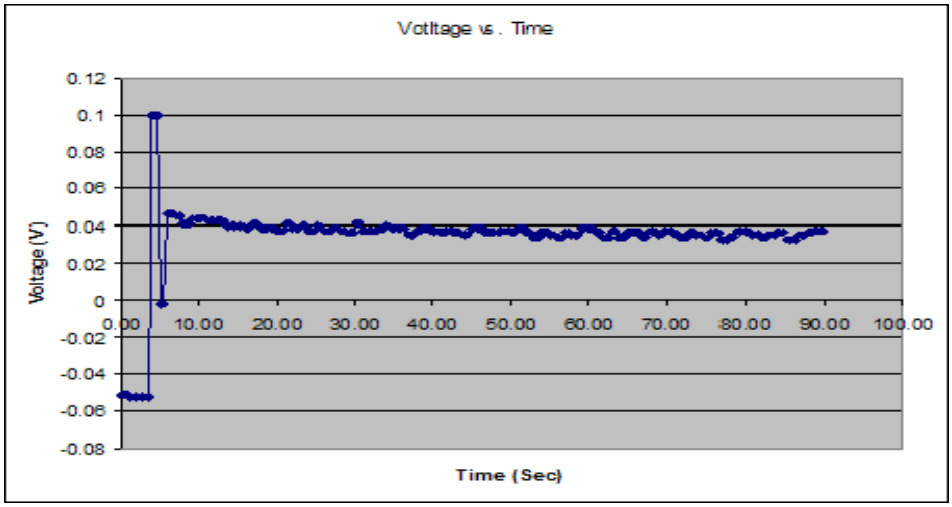

Figure 20. MEMS Start Up Profile.

As shown in Figure 20, the initial state of the rate output of the sensor is at some arbitrary value while the power is off, currently at -0.0513 V. Once the sensor was powered on it goes through a characteristic transition of roughly one second which was

seen in every startup test. During this transition the state of the sensor changes from non-operational to operational, achieving a constant rate output of 0.0464 V. This rate was interesting in itself. The sensor was not being subjected to any rotational rates, therefore the rate output from the sensor should have been zero, but as you can see this was not the case, and in fact, would be our first unknown source of bias.

After the one second transition, the biased output rate decreases slowly to an average bias of 0.0366 V over the next 50 seconds. After this the bias seemed to be fairly constant. There were numerous possible explanations for this phenomenon, but the one most likely was that the sensor needed a little time to reach its operational temperature. In response to this question, longer startup tests were conducted, and verified that an equilibrium bias state was achieved at approximately 50 seconds after startup, with a little further roll off over an additional 40 sec, with little to no change noted in this bias afterward.

2. Supply Voltage Differential Testing

A possible cause for the bias seen in Figure 20 could be the choice of input voltage. The manufacturer's data sheet states that the sensor requires a power supply of ±5 V ±3% [25]. This allowed for a potential supply range of ±5.15 V to ±4.85 V. To determine if the input voltage was the cause of the observed bias, three identical tests were conducted where the only variable changed was the input voltages. For simplicity sake these tests mimicked the startup test described above except that data collected began after startup and the data collected lasted slightly longer. The test results for this test can be seen below.

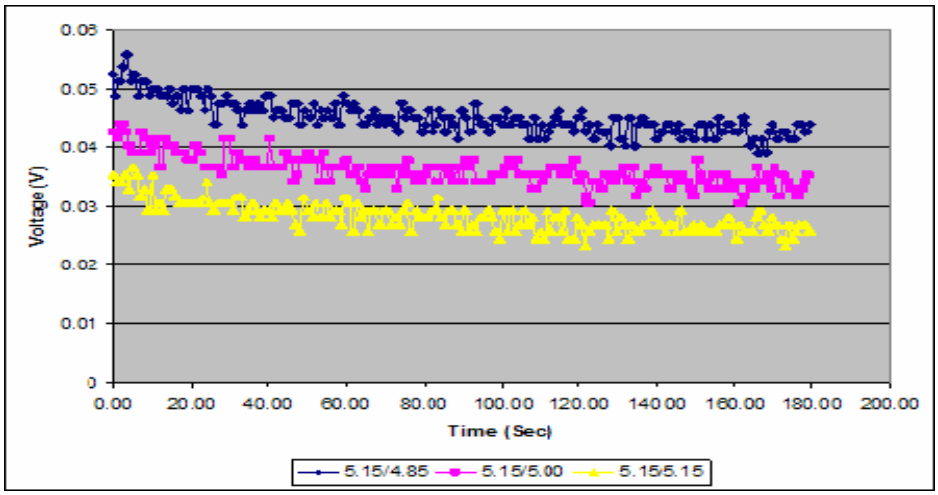

Figure 21. Voltage Differential Test vs. Bias.

Figure 21 shows that the bias is sensitive to the input voltages. The center plot (pink) seen above was supplied with the same voltage differential supplied for the test results seen in Figure 20. As we would expect, these results match perfectly with each other. What we do see is that the greater the input voltage differential, the great the bias. The upper plot (blue) with its 0.30 V of differential, that is the voltage difference between its positive and negative supply voltages, was observed to have an initial bias of 0.052 V. The center plot (pink) with its 0.15 V of differential was observed to have an initial bias of 0.044 V, very similarly to what was observed in Figure 20. The lower plot (yellow) had no voltage differential and was observed to have the lowest initial bias of 0.035 V. Thus it was confirmed that voltage differential did indeed effect the observed bias, but only slightly, roughly 10 mV of the observed bias. Further tests were then conducted to determine if the bias could be further reduced by setting the voltages to ±5.00 V as recommended, or possibly as low as ±4.85 V. While an improvement in bias as we lowered the positive input voltage was seen, the bias never went to zero. It was determined that for the remainder of the research conducted for this thesis that we would use the ±5.00 V as our supply voltage both due to the manufacturer's recommendation, as well as the fact that the lowest bias possible for any given supply voltage would have no voltage differential.

3. Gain Testing

Due to the limitations of the Analog-to-Digital Converters (ADC) of both the WEBDAQ (14 bit ADC) as well as that of the NPSAT1 ACS (12 bit ADC), we are only capable of achieving certain measurement accuracies within the rather large dynamic range of the sensor. By adjusting the gain in either the WebDAQ or in the ACS, we can achieve more accurate measurements at the lower end of the dynamic range of the sensors, where our interest lies. Unfortunately, doing so could reduce the overall dynamic range of the sensor, reducing the ability of the sensor to measure higher rates where there is also interest, during tip-off for example. This would cause clipping at the high ends of the sensors dynamic range, and would not be desirable.

Therefore, it is important to understand the resolution of both the WebDAQ as well as the ACS, and to determine if their measurement resolutions are sufficient for the needs of the experiment. If not, we must determine which gain is needed to increase this measurement resolution to a satisfactory level of signal accuracy, and determine if the loss of the overall dynamic range of the sensor is worth the increase in resolution. The first step was to determine the resolution of the WebDAQ and the ACS. To do this, a simple set of calculations was conducted to determine the theoretical resolution of the ADCS prior to experimental testing.

The WebDAQ is a 14 bit ADC with an overall dynamic range of ±10 V. Thus, its theoretical resolution (step size) can be calculated by 20 V / 2^{14}, which yields a resolution of 1.22 mV. This equates to 0.0024°/s, which is roughly 1/27 of orbital rate at LEO. This is more than accurate enough for our measurement purposes, easily falling within the ±4 mV standard deviation we had been observing in the rate output voltage. To verify this theoretical resolution, a quick test was conducted to capture a representative sample of the bias and noise of the sensor and determine the minimum step size of data (resolution). To do this the MEMS was powered on and allowed to warm up for 5 min. Once a steady operational state had been reached, rate data was acquired by the WebDAQ every second, and the bias vs. time was plotted below.

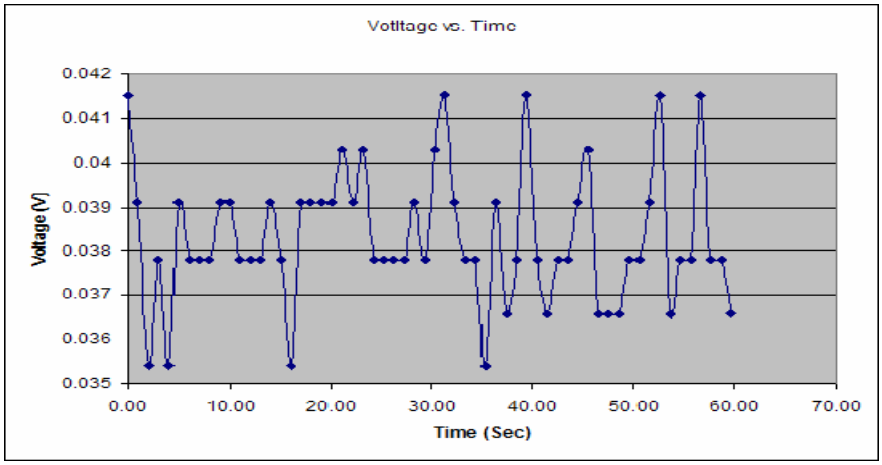

Figure 22. WebDAQ Resolution at 1X Gain.

As you can see, for a gain of 1X, the WebDAQs actual resolution (step size) is 0.0012 V, perfectly matching the calculated theoretical value of 0.00122V. This tells us that the WebDAQ is operating as it should, and that its measurements are accurate enough for the purposes of this research. It was then time to calculate the theoretical resolution of the ACS.

The ACS will utilize a 12 bit ADC with an overall dynamic range of 0 to 5 V. Thus, its theoretical resolution (step size) can be calculated by 5 V / 2^{12}, which yields a resolution of 1.22 mV. This is exactly the same resolution that we achieved from the WebDAQ. This indicates that the ADC of the ACS is accurate enough to accurately resolve rates from tip-off to well below Earth rate, yet the true accuracy and resolution of these measurements will still depend on the accuracy of the MEMS sensor. Even though the ACS is capable of resolving very fine measurements, this will be of no use if the MEMS can not provide data that is at least as resolved. If the sensor is able to accurately measure these rates, it would be possibly to accurately measure the rates of the spacecraft during routine attitude adjustments conducted on orbit by the ACS. These rates would be very small, and would be associated with the ACS's attempt to maintain a specific nadir orientation while on orbit. As long as these rates are not too low, perhaps 1/10 orbital rate, the ACS should be able to accurately measure the MEMS rate output. If the rates to be measured are lower than this, a gain in the signal output may be required to improve

the overall signal resolution. To verify this, further testing may need to be conducted once bias and noise has been compensated for, and after a better understanding of the expected rate environment is modeled.

A quick calculation was conducted to compute the likely gain value needed to achieve a resolution capable of measuring rates as low as 1/40 orbital rate. This resolution was calculated to be 33 mV / 40 = 0.8 mV, where 33 mV represents the orbital rate of 0.066°/s divided by the sensor's scaling factor of 2°/s per volt. To achieve this resolution with the ACS, a gain of 1.48 would be required. This gain would reduce the dynamic range of the signal from 0 to 5 V to 0 to 3.38 V, effectively reducing our measurable rate range from ±5°/s to ±3.4°/s. To verify this, four separate tests were conducted, where the gain values of the WebDAQ were set at 1X, 4X, 10X, and 40X. The WebDAQ test channel was given an initial input of 5V, and this input was scaled down by 1 V every 20 to 30 seconds to zero. The results of this test can be seen below.

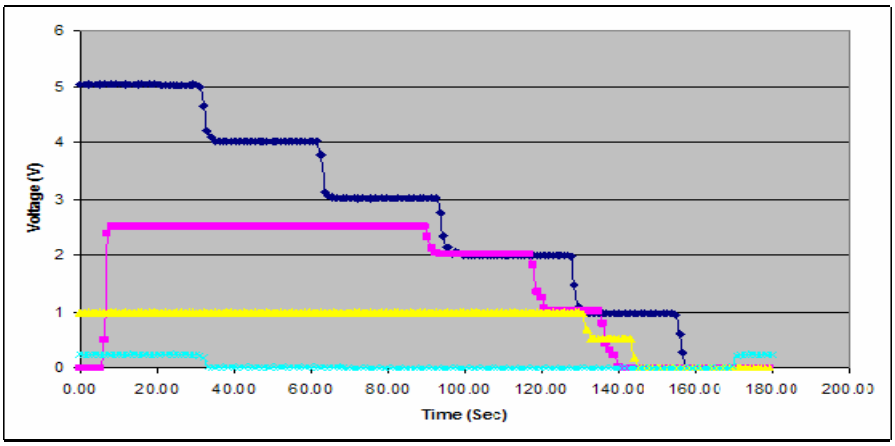

Figure 23. Clipping vs. Gain.

As you can see, the upper plot (blue) used a gain of 1X, and resulted in a resolution of 1.22 mV and a measurable dynamic range of ±10 V, as expected. The next plot (pink) used a gain of 4, and resulted in an increase in resolution to 0.3 mV, but dramatically reduced the measurable dynamic range to only ±2.5 V, a quarter of its original range. This increase in resolution may not be worth the loss in dynamic range.

For the ACS, a gain of 4X would result in a decrease in measurable dynamic range from ±5°/s to only ±1.25°/s. Therefore, with no overwhelming need for measurement accuracy greater than 1/27 orbital rate, and without knowing the MEMS ability to output meaningful data at such a low rate or out ability to pick out such a small signal from the noise, it was decided that no gain would be applied to the rate output of the sensor.

4. Long Term Bias Testing

The next step in this testing series consisted of running a startup test for an extended period of time to observe the characteristics of the signal bias over a much wider range of time. In particular, we were interested in seeing if the steady state bias observed in the initial testing after 50 seconds would remain constant, or if it would continue to drift lower over time. Therefore, another startup test was conducted, this time the Python program was set to acquire data from the WebDAQ every 30 seconds for 22 hours. This data can be seen below.

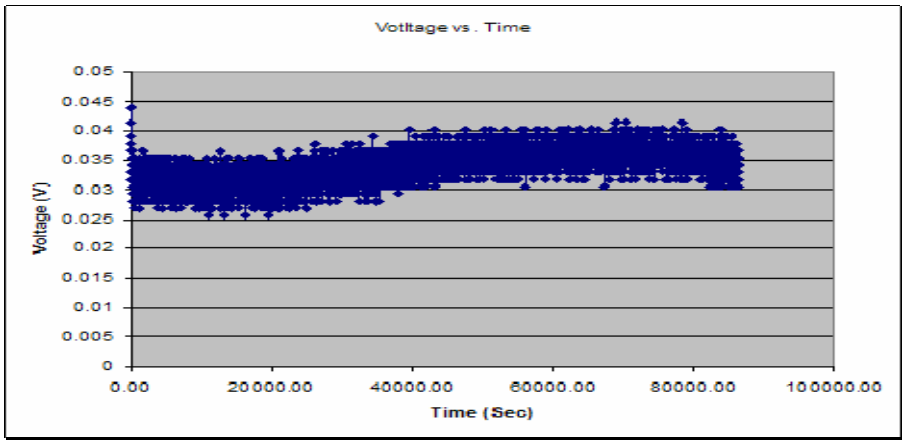

Figure 24. Long Term Startup Test (1 Day).

In Figure 24, an interesting artifact is seen over the duration of this test. What can be seen is what looks to be a cyclical variation of bias over the length of the test. Initially this artifact was troubling until it occurred to us that this characteristic may not be internal to the MEMS sensor, but rather an effect of the environment, possibly due to the

variation of temperature in the lab over the 22 hours of the test. To verify this hypothesis the test was repeated, this time for a period of three days. The results of this test can bee seen below.

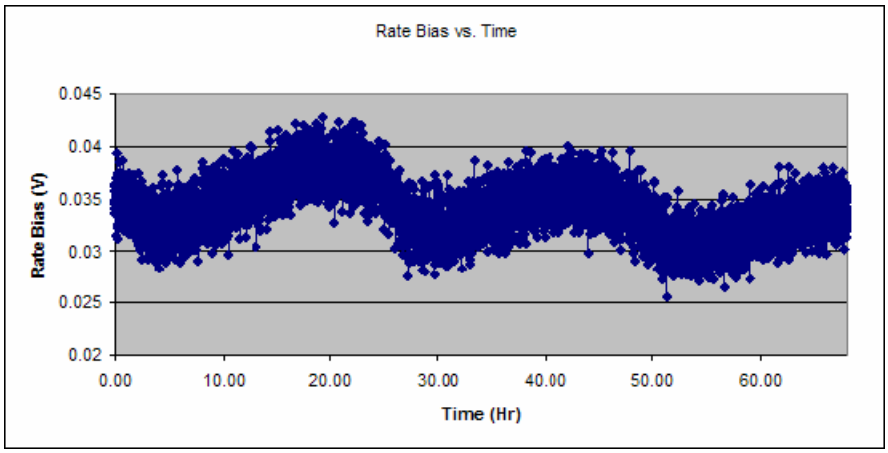

Figure 25. Rate Bias Voltage vs. Time (3 Days).

As seen in Figure 25, the rate voltage is indeed cyclical, and looks to be repeatable. There was a gradual shift in the voltage of the peaks of the graph, but this coincides with the fact that each of the three days was warmer than the previous. It seemed that temperature had a direct impact on the observed bias, and possibly linear, though further testing would be needed to confirm this. If this was true, it should be possible to compensate for bias for any given temperature. To do this an accurate temperature would need to be referenced, preferably from the same location as the sensor output. It turns out that the QRS11 provides a temperature output signal [25]. This signal was not included in the original power filter PRCB, wiring harness, or MEMS designs because the manufacturer had specified that the units purchased by NPS were already temperature compensated and that no further improvements in output accuracy could be achieved using temperature output [26]. To verify that this was in fact true, as well as to verify the relationship between temperature and bias, we would first need to integrate the temperature output form the sensor into the experimental set up.

5. Temperature Validation Testing

To take measurements of the MEMS internal temperature, a secondary wiring harness was built to connect Pin 6 to an open channel of the WebDAQ, and was run in parallel with the original test harness. Additionally, for comparison and validation purposes, a thermistor circuit was built into the WebDAQ utilizing a precision resistor. This setup can be seen in Chapter III and is identical to the thermistor circuits used in tests to monitor battery temperature [5]. The thermistor element was secured to the side of the QRS11 sensor with thermally conductive adhesive, inside of the MEMS housing cover. The thermistor's purpose was to provide a precise temperature for calibration and verification of the MEMS temperature output.

The QRS11 temperature output voltage varies from unit to unit, but has a nominal voltage between -0.100 to +0.050 VDC at 25°C. This nominal voltage will need to be determined for the sensor at 25°C before any temperature data can be processed. Once the nominal voltage is determined for the sensor, it should change with a positive, linear slope of nominally +0.0033 V/°C [25]. To determine the nominal voltage for the test sensor, a 28 V resistive strip heater was applied to the top surface of the MEMS housing, and powered by a separate power supply. Due to the large thermal mass of the sensor and mount, an insulating pad was inserted to isolate the sensor housing from the HAAS rotary table. Even with this, the heater would still take a long time to heat the MEMS sensor to the required 25°C, giving some control of how fast the sensor was heated. Once the internal thermistor temperature reached 25°C (77°F), the heater voltage was lowered to a point where a constant internal temperature was obtained. This was left for 30 minutes, giving the MEMS sensor time to thermally saturate. At this time three short tests were run to capture the nominal voltage value of the MEMS temperature output from Pin 6. Each test was one minute in length, and all data points with corresponding thermistor temperatures of 25°C were averaged together, yielding a nominal voltage for the test sensor of 0.0354 V.

With the nominal voltage of the test sensor determined, we conducted a long duration temperature test to verify the accuracy of the nominal voltage value, as well as the correspondence between to two independent temperature readings. A test was run for

three days, and the results of both the MEMS internal temperature output and the thermistor output are plotted together below.

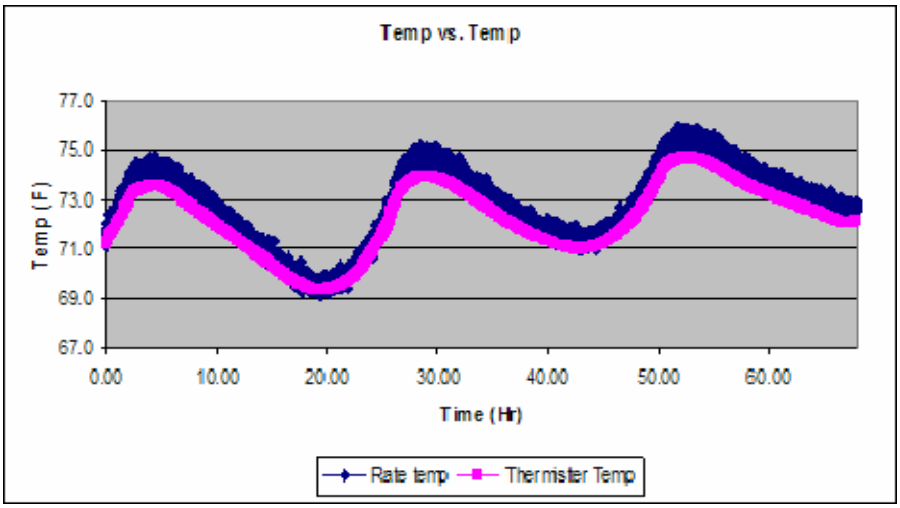

Figure 26. MEMS Temperature vs. Thermistor Temperature.

As you can see, both temperature measurements are quite close to each other, with the average temperature difference between the two being only 0.53°F. This can possibly be attributed to the fact that the MEMS output temperature is taken internally to the sensor, where it may be slightly warmer than the outside of the sensor. Also, a slight phase shift can be seen in the thermistor temperature output with respect to the MEMS temperature output. This is most likely due to the time required for the external temperature to dissipate and saturate the interior sensor. Although investigation and testing with temperature could confirm this hypothesis and validate the accuracy of the MEMS internal temperature output, in the end this is unnecessary, and the MEMS internal temperature output can be used directly to determine the rate bias.

6. Bias vs. Temperature Testing

With the internal temperature output of the MEMS adequately validated, it was now possible to conduct testing on the relationship between the MEMS temperature and its bias output. If we could establish that such a relationship did indeed exist, it might be

possible to account for all bias due to temperature. To ensure that we had a wide enough temperature variation during testing, a Formula Scientifica Bath and Circulator was used in conjunction with a cold plate to cool the MEMS sensor to roughly 48°F. The circulator was then turned off and the WebDAQ and Python data acquisition software was started. The test ran for 24 hours, and at approximately 20 hours a second cooling cycle was started. Both rate bias and temperature plots can be seen below in Figure 27 and 28.

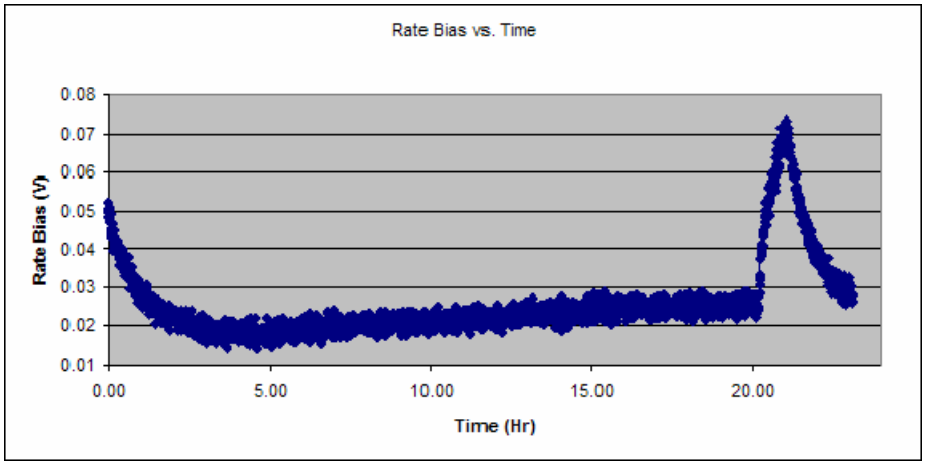

Figure 27. Rate Bias Voltage vs. Time.

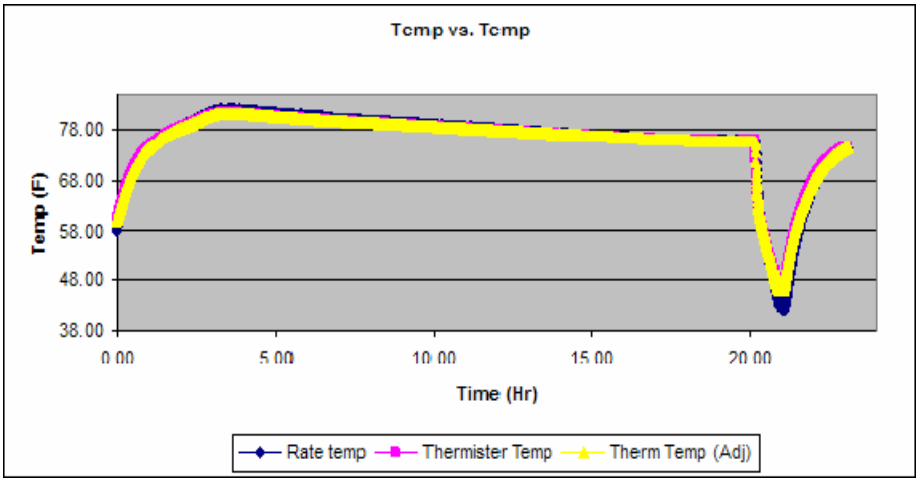

Figure 28. Temperature vs. Time.

Both the MEMS temperature output as well as the thermistor temperature output continued to follow each other well over the entire 40°F temperature range of this test. This verifies the calibration of the MEMS temperature output against the thermistor and validates its use over a much larger temperature range. This relationship will probably hold over all temperature ranges, but that may need to be verified. The major insight gleaned from the above two figures is the remarkable correlation between the bias and the temperature. Both plots seem to be the exact inverse of each other. This is strongly indicative of a linear relationship between bias and temperature. Additional tests over a variety of temperature ranges were performed to verify this relationship, and the results were always the same. To verify that the relationship between bias and temperature was truly linear, the MEMS bias data was plotted vs. the MEMS temperature data.

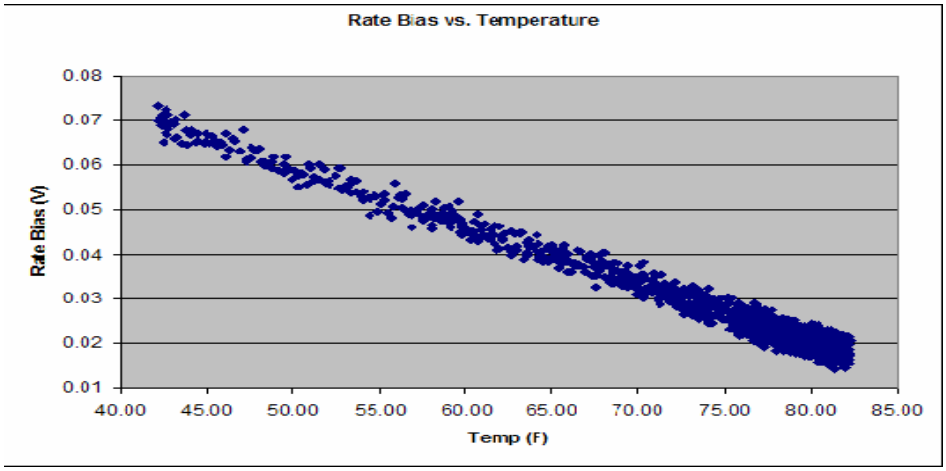

Figure 29. Bias vs. Temperature.

Figure 29 shows what appears to be a linear relationship between bias and temperature. Only through bias vs. temperature testing over the entire expected operating temperature range of the spacecraft will we be able to determine if this relationship is truly linear, or if it is a quadratic or cubic function. Treating this as a linear relationship, we attempted to adjust the bias plot seen in Figure 28 by compensating for temperature. To do this we used a simple linear formula. $Y = mX + b$, where Y is the rate bias in volts to be subtracted from the measured rate; X is the measured temperature in °F; and m and

b are constants calculated from the bias vs. temperature plot by using the Linest function for a linear plot in Microsoft Excel. The Linest function was calculated using the temperature and bias data from Figure 29, and yielded the following values.

Y	X	m	b
Rate	Temp	-0.0027576	0.07104

Table 16. Linear Compensation Variables.

These variables are used to calculate the rate bias value for every data point from the test. This value is then subtracted from the original rate value to yield a corrected rate output that has been stripped of all temperature dependant bias. The corrected values were then plotted as shown in Figure 30.

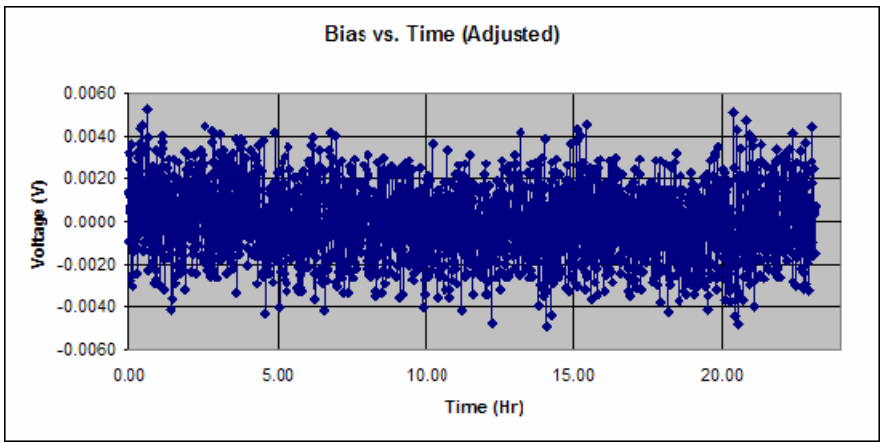

Figure 30. Adjusted Bias vs. Time (Figure 27 Adjusted for Bias).

The bias voltage seen in Figure 29 has been eliminated, leaving a straight and constant rate output with an average rate output of 0.000 V. This is what is expected when no rate is applied, and shows that temperature appears to be the root cause of, if not the sole source of the observed bias. With a firm understanding of the relationship between temperature and bias, it is now possible to successfully remove the bias,

eliminating it as a source of sensor error. This test was repeated with a different cooling profile, and the same results were obtained as seen in Figure 30. Because the temperature range observed does not yet see the full operating range of the spacecraft, it is difficult to confirm that the linear bias compensation values calculated in Table 16 will hold true over the entire expected temperature range. To verify this similar temperature vs. bias testing over a much larger temperature range were needed.

7. Thermal Vacuum Bias vs. Temperature Testing

Thus far, all bias vs. temperature testing had been done over a relatively small temperature range. To verify that the calculated linear bias compensation values will hold true for all expected temperatures the sensor needed to be tested over a much larger temperature range. To qualify for space flight, the sensor must prove that it is capable of surviving in a temperature environment ranging from -29°C (-20°F) to 66°C (151°F), for the purpose of this test we will use this expanded temperature range to verify a linear relationship. While this range is ideal for determining the linearity of the bias vs. temperature plot, it will not be ideal for the calculation of the bias compensation values. The expected operational range of the sensor is only -11°C to 9°C. Therefore, to yield the most accurate bias compensation values, the temperature range should be limited to this range. Either way, both of these ranges will need to be investigated individually, and bias compensation values computed for each.

To obtain such a wide temperature range, the TVC was used to control the temperature experienced by the MEMS sensor. The experimental test setup was moved from the solar cell lab down into the satellite lab as described in Chapter III. Once the MEMS and the WebDAQ were verified to be operational, the TVC was purged and set to -35°C. Once the MEMS had reached the desired temperature, the TVC was turned off and the bias vs. temperature test was started, and allowed to run for 12 hours. The bias and temperature results can be seen in Figure 31 and 32.

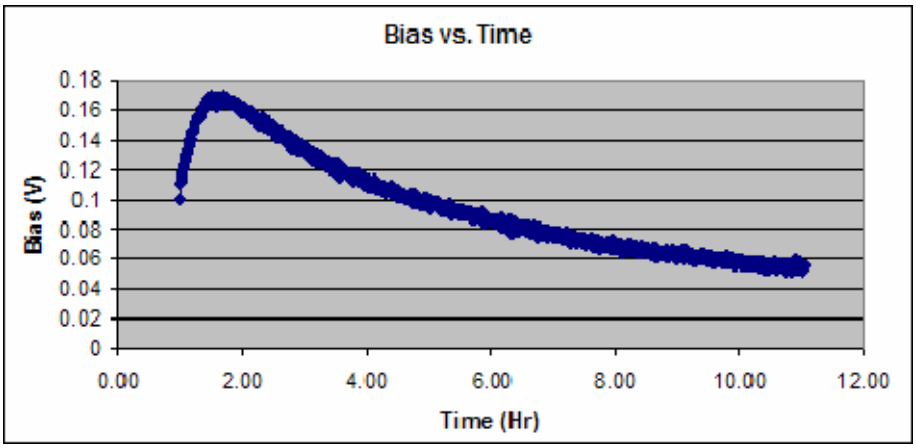

Figure 31. TVC Bias vs. Time (Cooling).

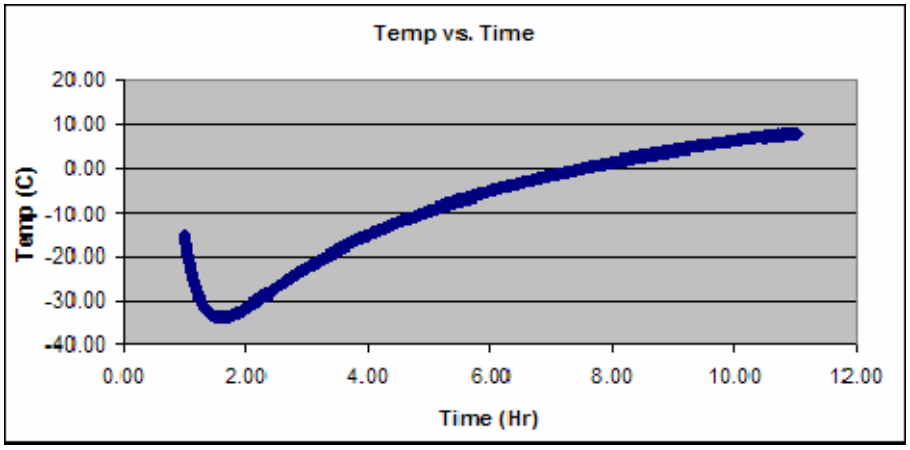

Figure 32. TVC Temp vs. Time (Cooling).

As before an inverse correlation between the bias and the temperature is seen. This data was then plotted in relation to each other in the TVC bias vs. temperature plot seen below.

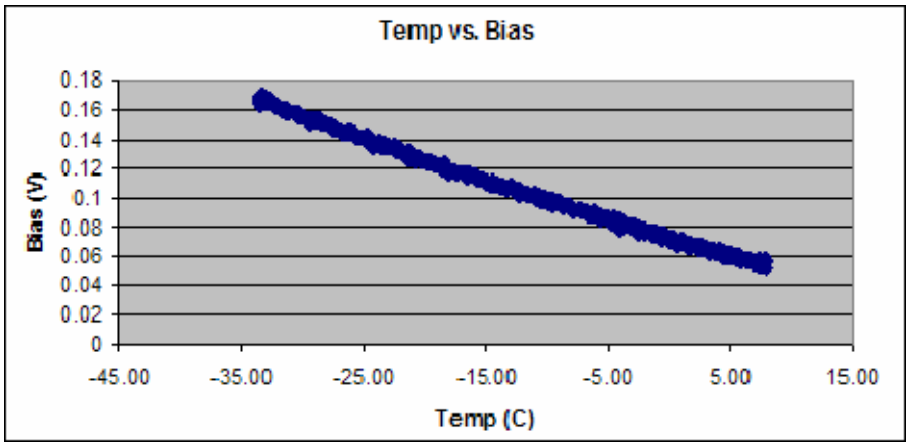

Figure 33. TVC Bias vs. Temp (Cooling).

Although the relationship seems to be fairly linear, it is possible to see a curve in this plot, suggesting that the temperature vs. bias relationship is not simply linear. To verify this, the bias compensation values were again calculated using the linear Linest function in Excel, and temperature and bias data from Figure 33, yielding the values in Table 17. Note that these values are almost the same as the values seen in Table 16 to within about 2%. This says that there is little variation between the values calculated in the TVC and those calculated in the solar lab.

Y	X	m	b
Rate	Temp	-0.0026868	0.072872

Table 17. Linear Compensation Variables.

These variables were then used to calculate the rate bias value for every data point from the test. As before, this value was then subtracted from the original rate value to yield an adjusted rate output that was stripped of all temperature dependant bias. Figure 31 was then re-plotted with its corrected rate vs. temperature, as seen in Figure 34.

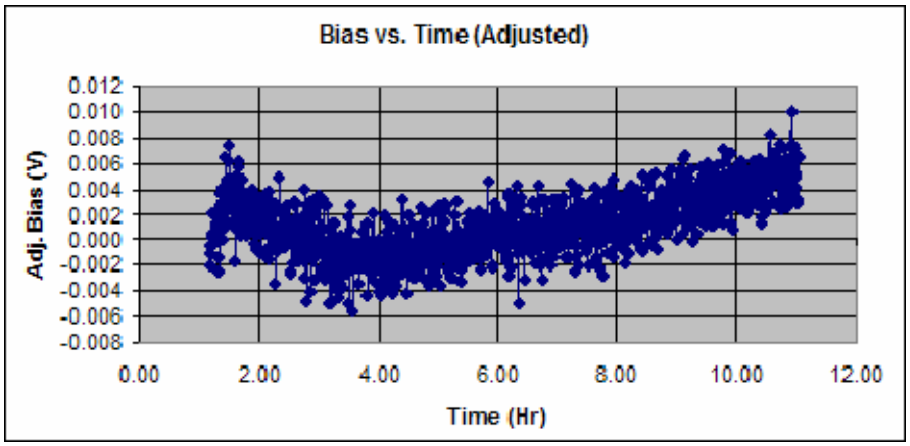

Figure 34. Adjusted Bias vs. Time (Figure 31 Adjusted for Bias).

Clearly, the linear bias compensation values no longer adequately compensate for bias over the temperature range of this test. The average rate is no longer zero, and the standard deviation has increased significantly. This indicates that the bias vs. temperature relationship is not linear, and in fact, it is most likely at least quadratic. To test this hypothesis, the Linest function was again used to calculate the bias compensation values from the data from Figure 33. But this time, the Linest function was used to calculate a quadratic curve rather than a linear. To do this we used the following formula, Y = m2*X^2 + m1*X + b, where Y is again the rate bias value to be subtracted from the measured rate; X is the measured temperature; and m2, m1, and b are constants calculated from the bias vs. temperature plot by using the Linest function for a quadratic plot in Microsoft Excel. The Linest function was calculated using the temperature and bias data from Figure 34, and yielded the following values.

Y	X	m2	m1	b
Rate	Temp	0.000011	-0.0024196	0.072504

Table 18. Quadratic Compensation Variables.

These variables are then used to calculate the rate adjustment value for every data point from the test. As before, this value is then subtracted from the original rate value to

yield an adjusted rate output that has been stripped of all temperature dependant bias. The new quadratic adjusted rate plot is plotted on top of Figure 34 for comparison and can be seen below in Figure 35.

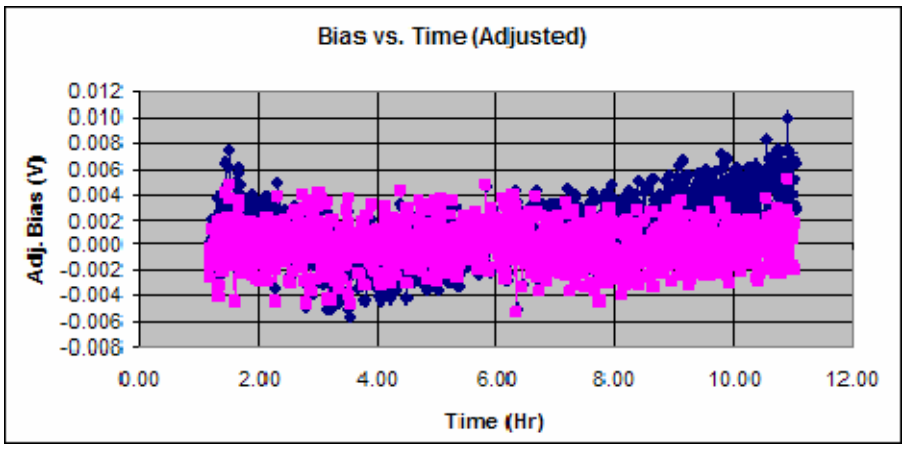

Figure 35. Linear vs. Quadratic Adjusted Rate Outputs.

The quadratic bias compensation values accurately compensate for bias over the temperature range of this test where the linear bias compensation values could not. The average rate returns to zero as we saw in earlier tests, and the standard deviation decreases as well. This shows that the temperature vs. bias relationship is not linear, and is at least quadratic. Further investigation and testing at the lower temperature ranges validated this data, and verified that a quadratic is an accurate representation of the bias vs. temperature curve for the lower half of the qualification temperature range. This is the range for the MEMS expected operational temperatures, and therefore, quadratic bias compensation values should produce the most accurate values.

The next logical series of tests were to repeat the same TVC bias vs. temperature tests as before, but for the upper qualification temperature range. As expected, the upper curve was also shown to be non-linear, and is also quadratic. Yet, the curve in the upper half of the temperature range was inversed from the curve seen in the lower half of the temperature range. This is more easily seen in Figure 36 in the next section, but verified that the overall curve for the entire temperature range is not a quadratic, but actually at

least a cubic. Therefore, when computing the bias compensation values for the entire qualification temperature range, a cubic curve and bias compensation values should be used. With the insights gleaned from this section, it was now time to conduct the testing and calculations to accurately calculate the actual bias compensation values for the test sensor for both the qualification range as well as the operational range.

8. Bias Compensation Algorithm Testing

It is desired to be able to easily convert raw MEMS rate data into "corrected" rate data. This process uses the cubic relationship between bias and temperature to compensate for the inherent offset of the sensors rate voltage due to temperature. Previously, linear and quadratic equations were used to fit these curves, but the wider the temperature range got, the more obvious the need for a cubic equation. To do this, we needed to conduct experimental testing, correlate all the relevant data, and use analysis tools to generate a best-fit cubic equation. The rate bias vs. temperature data used to generate this cubic function was obtained by conducting three long-duration thermal vacuum chamber tests, one in the upper temperature range, and two in the lower temperature range where the sensors was expected to operate. The bias vs. temperature plots of these three tests can be seen in Figure 36.

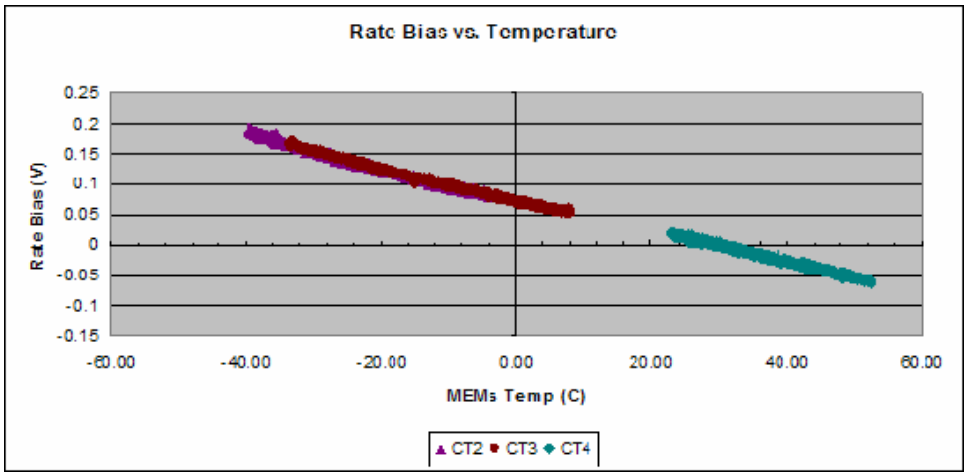

Figure 36. Bias vs. Temperature (Qualification Range).

The overall shape of the curve is indeed cubic. These three tests yielded a total of 47 hours of experimental data, and covered a temperature range of over 95°C. You will notice the gap in the curve representing room temperature from which the tests were started. In order to reduce induced noise from the chamber, tests were not begun until after they were at either the high or low temperature. In the interest of time, the tests were stopped prior to reaching room temperature, yielding the gap you see above. This will be addressed during the characterization of the flight unit by increase the test length to allow the tests to fully return to room temperature. After compiling all the bias vs. temperature data for these three tests, a Linest function in Excel was performed to generate the needed cubic bias compensation values for m3, m2, m1, and b. These bias compensation values can be seen below.

Y	X	m3	m2	m1	b
Rate	Temp	-3.8093893	-0.8473034	-0.7856849	-0.0147263

Table 19. Cubic Bias Compensation Values (Qualification).

To verify that these bias compensation values are accurate over the entire temperature range and that the overall shape of the plot is adequately represented by a cubic, these compensation values are plotted against the data from Figure 36. If the experimental data deviates from the cubic fit, then this relationship may not be cubic, and further research into the geometry of the relationship curve would be needed. The cubic fit is plotted with respect to Figure 36 below in Figure 37.

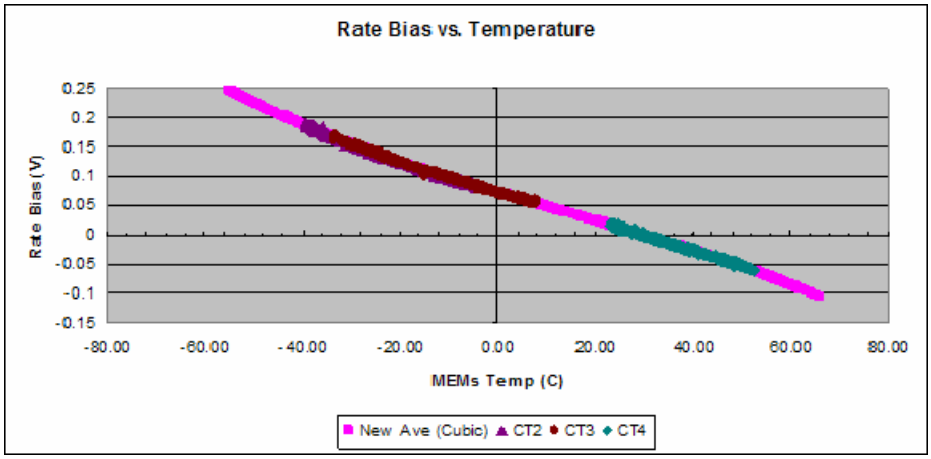

Figure 37. Theoretical Cubic vs. Actual Data.

The theoretical plot of the cubic fit matches the experimental results obtained through the three thermal chamber tests over the entire temperature range. It is now possible to compensate for temperature related bias over the entire qualification temperature range of the spacecraft. To verify this, the cubic bias compensation values were used to calculate the rate adjustment value for every data point from the three tests using the following formula, $Y = m3*X^3 + m2*X^2 + m1*X + b$. Where Y is again the rate bias value to be subtracted from the measured rate, X is the measured temperature, and m3, m2, m1, and b were calculated in Table 19. As before, this value was then subtracted from the original bias values of all three tests to yield an adjusted rate output that had been stripped of all temperature dependant bias. The new cubic corrected rate plot was plotted below.

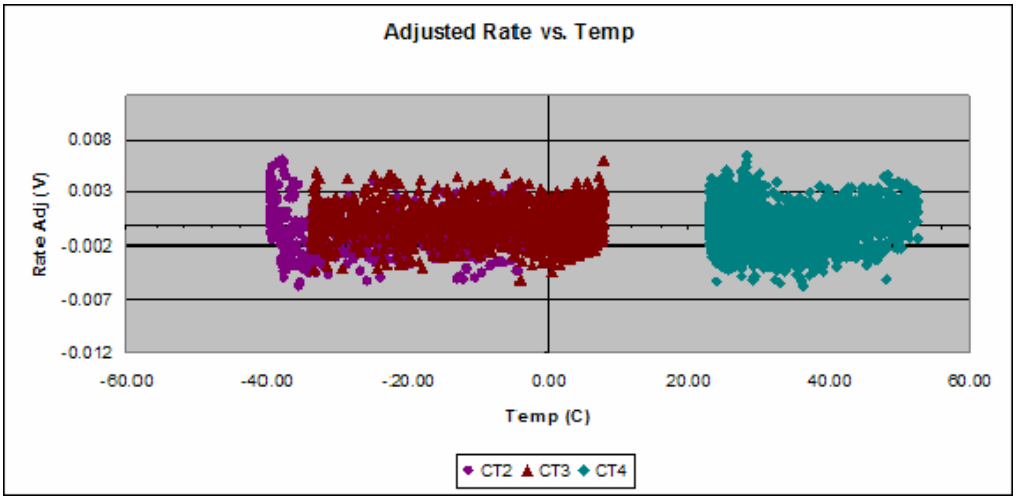

Figure 38. Adjusted Output (All Data).

As you can see, the plot takes the raw rate data from all three tests, and corrects for temperature using the newly formulated cubic bias compensation values. The original data nicely reduces to an average rate value of -0.00005 V, with a standard deviation of only 0.00172 V (1.7 mV). Also visible is the ±4 mV of rate signal noise that is consistent with the 200 Hz sampling rate we have become accustomed to using through most of the experimental testing. This rate was based on the approximate maximum available sampling bandwidth of the ACS [3]. The further reduction of this noise will be the focus of the next chapter.

C. CONCLUSIONS

Through the experimental research conducted in this chapter we set out to understand and characterize the QRS11 MEMS angular rate sensor. This thesis research began with the desire to fully understand the capabilities of the QRS11 angular rate sensor and to determine its capabilities. Initially knowing little about its potential capabilities, a wide variety of characterization tests were conducted to gain a better understanding of the basic operation of the MEMS sensor during startup and normal operations, as well as an understanding of the effects of bias on the signal output. What we found during these tests was that temperature is the single largest driver of bias in the rate output signals of the sensor. While some yet unknown factors may still contribute

slightly to this observed bias, we found that nearly all observable bias could be effectively removed by compensating for temperature.

This discovery lead to the generation of a cubic function to be used to generate bias compensation values for the entire temperature range required for space flight qualification. Now we can take any biased rate and temperature data from the QRS11's and remove the bulk of the bias from the rate output, resulting in a correct rate for any given temperature. This discovery warrants a serious re-investigation into the possible utility of the QRS11 sensors at very low rates and suggests that the QRS11 sensors may be capable of performing at much lower rates than expected. To verify this further testing will be conducted in Chapter VI specifically addressing bias compensation of a sensor undergoing a known and calibrated angular rate. Of the two most obvious sources of sensor error, bias appears to be understood, leaving only noise.

V. PCFB TESTING, RE-DESIGN, AND BUILD

A. INTRODUCTION

In Chapter IV we described how the bias offset for the QRS11 is almost entirely dependant on temperature and how it is possible to formulate sensor-specific bias compensation values that effectively remove rate bias due to temperature. It is now possible to focus our attention on the next known error mechanism for the sensors, and that is the inherent sensor noise itself. As we saw in Chapter IV, the QRS11 has a very specific noise profile which can be seen below.

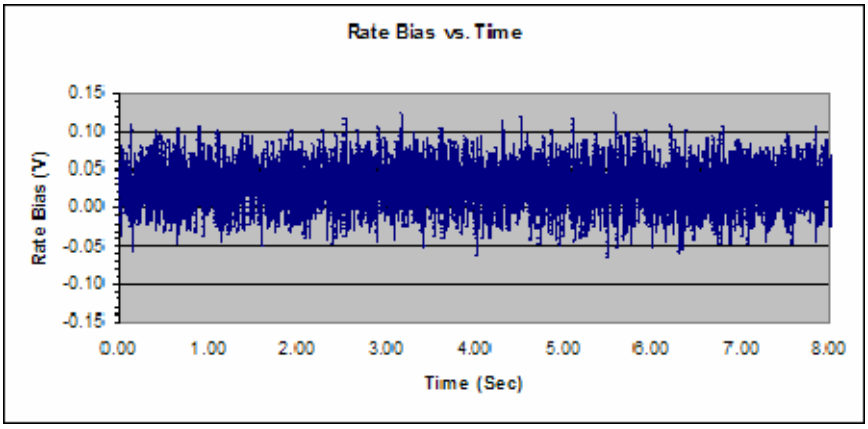

Figure 39. MEMS Rate Output Noise (Zero Rate).

This profile was obtained by using the Agilent high end scope with the new low noise probes to capture a representative sample of the internal noise of the QRS11 sensor (Configuration 1) prior to any voltage regulation, filtering, or averaging at room temperature, and with no rate applied. This data was taken at 1K samples/sec, and resulted in an average rate output of 0.027 V with a standard deviation of 0.025 V. The maximum voltage output was observed to be 0.122 V and the minimum voltage output was observed to be -0.067 V, yielding a noise spread distribution of 0.188 V, corresponding to 4σ. This noise data is repeatable, and consistent with all noise experiments conducted thus far. The bias due to temperature adequately explains the 27 mV offset seen in the rate output. The noise dynamic range over the standard deviation

(4σ) is most likely due to inherent noise in the system. The frequency components of the noise from Figure 39 can be seen in the FFT of the noise below in Figure 40.

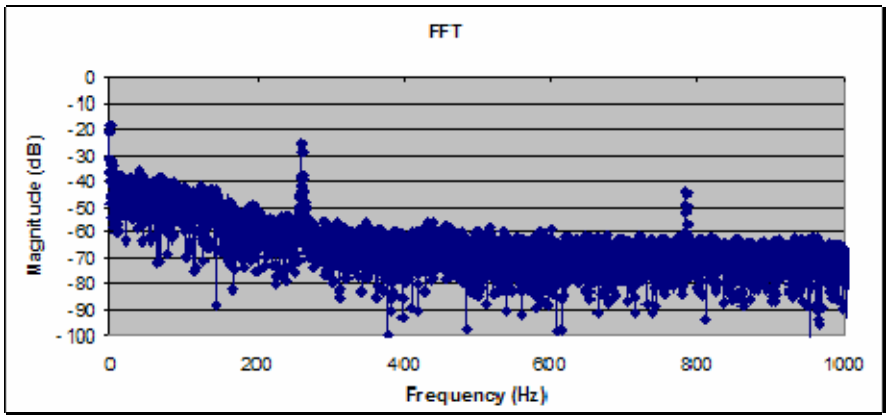

Figure 40. MEMS Rate Output Noise FFT (Zero Rate).

There are three frequency spikes present, and these spikes are probable causes for the rather large dynamic range seen in Figure 39. The first spike, seen near 0 Hz, represents the bias offset of the sensor due to temperature. The second spike at approximately 262 Hz, is a known characteristic of the sensor, and was specified by the manufacturer as an inherent manufacturing artifact [25]. The third spike is the third harmonic of this tone at approximately 786 Hz. The shape of the FFT is as anticipated according to the manufacturer, with a sensor bandwidth of 100 Hz and a roll off of -12 dB per octave [25].

To verify that the large dynamic range and noise spikes seen in Figure 39 and 40 are truly random noise and not some other artifact, a histogram was constructed from the data to plot the distribution of the data points to determine if they are Gaussian or not. This plot can be seen in Figure 41 below. As you can see, the Gaussian curve was plotted on top of a histogram using an average of 0.024 V and a standard deviation (σ) of 0.025 V, showing that the noise is a random, Gaussian distribution.

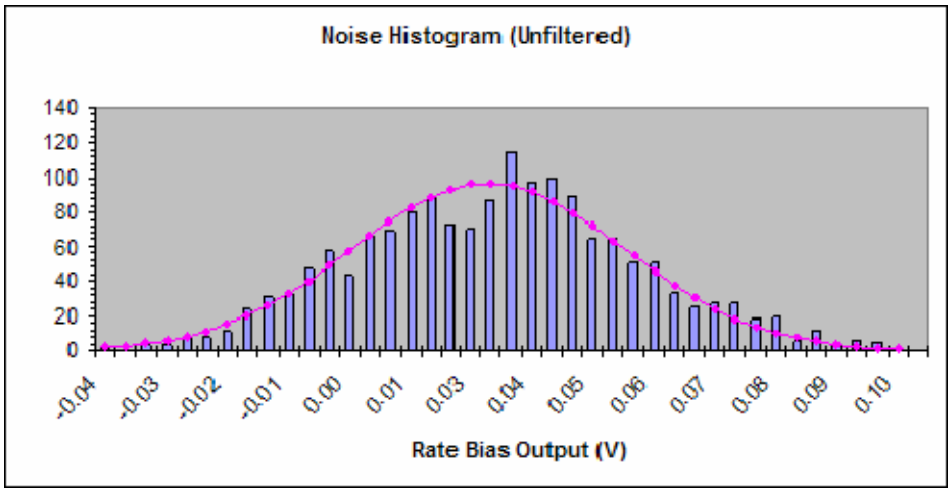

Figure 41. Gaussian Distribution of Initial MEMS output.

The rest of this chapter describes the efforts to reduce the noise of the QRS11 sensor outputs to yield a cleaner signal. To do this we will need to focus on two specific areas. First, we will need to reduce the possibility of inducing noise due to power quality as suggested by the manufacturer [25]. We can do this by voltage regulation and power filtering. Next, we will attempt to develop a filtering scheme to reduce the sensor's inherent noise profile. This will focus on removing the noise spikes seen in Figure 40, as well as in an overall reduction of the 4σ noise spread seen in Figure 39.

B. POWER FILTER / VOLTAGE REGULATOR TECHNIQUES

The first possible method for noise to be induced into the MEMS system is through the power input from the NPSAT1 ACS board. To ensure that power input is not a cause of the noise, each QRS11 sensor in the suite will need to be supplied with a clean power input. The MEMS (Configuration 2) accomplished this through the addition of a simple PRCB to be mounted on the top surface of the sensor. Its purpose was to regulate and filter the power from the ACS board as close as possible to the sensor prior to its use. The voltage regulator took the supplied ± 12 V, stepping the voltage down to the ± 5 V required by the sensor, and also filtering the power prior to supplying it to the MEMS. The latest PRCB diagram can be seen in Figure 42. Though this PRCB met the requirements for power regulation and filtering, through lessons learned in the research in

this and previous chapters, it was determined that it would no longer meet the current needs of the experiment, specifically in that it did not address the noise of the sensor itself. Therefore, this PRCB needed to be re-designed to properly mitigate the effects of sensor and transmission noise.

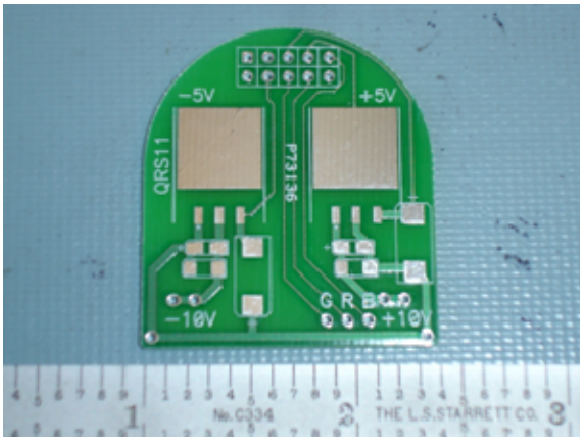

Figure 42. PRCB Design Picture.

C. POWER FILTER / VOLTAGE REGULATOR TESTING

As mention earlier, the PRCB design included a simple voltage regulator and filter designed to reduce the possibility of inducing noise from the power supply. The design of this regulator and filter circuit stemmed from the recommendation of the manufacturer. It stated that to realize the performance parameters specified in Table 2 for the QRS11 Rate Sensor, the input voltage must be well regulated and relatively noise free in certain frequency bands [25]. The recommended circuit is comprised of a positive and negative voltage regulator, integrated into a circuit loop of capacitors to accomplish the power regulation and filtering. This circuit is shown in Figure 43. To optimize the performance of the filter, it was also recommended to place the filter within three inches of the sensor. This is the reason we mount the PRCB directly to the sensor.

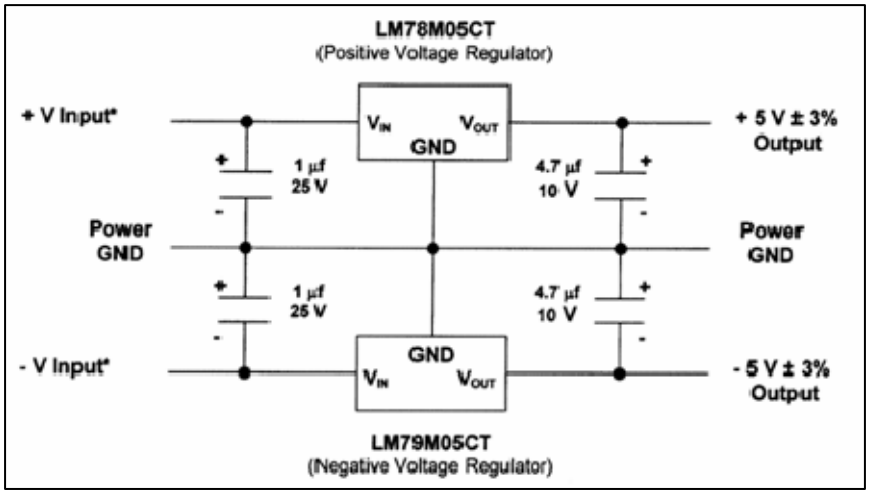

Figure 43. BEI Recommended Voltage Regulator Circuit.

1. Description

The SDI Voltage Regulator Circuit is the foundation for the redesign of the last PRCB. The first modification we will be making to this circuit design is in the overall reduction of component size. The last PRCB design utilized two large voltage regulators to dissipate the heat from the ±12 V input to ±5 V, too large for the new PCFB, with three times the number of components as the last PRCB. Smaller surface mount components were ordered to replace the larger parts. Additionally, to reduce the size of the voltage regulators, the power provided by the ACS board was reduced from ± 12 V, to ± 6 V, and a Low Drop Out (LDO) regulator was selected. Before building this finalized test board, the circuit seen in Figure 43 was built with available components to test its functionality. This test board is seen in Figure 44.

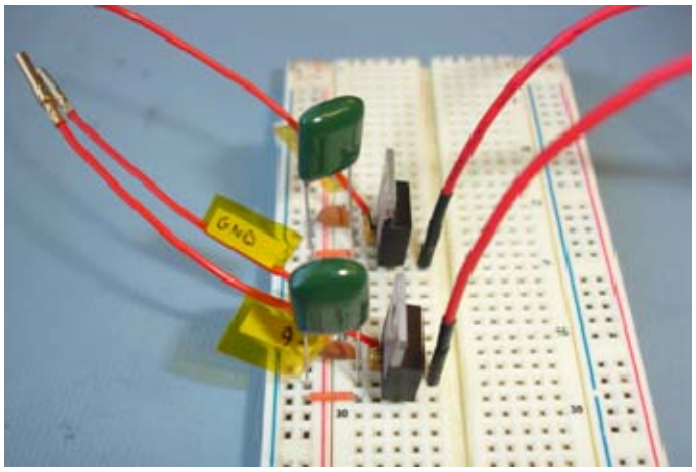

Figure 44. Voltage Regulator and Power Filter Circuit Picture.

2. Testing

The test board seen above was placed on the experimental test bench. A calibrated multi-meter and power supply was used to provide the test circuit with a variable power input, and the Agilent scope was connected to the circuit to monitor the voltage output of the test board. The sensor was then supplied with a calibrated input voltage as seen below in Table 20, and the outputs were recorded.

Power In	Regulated Power Out
± 8.02 V	-4.985 / +4.995
±7.00 V	-4.985 / +4.995
± 6.00 V	-4.985 / +4.995
± 5 V	-4.400 / +4.110
± 4 V	-3.392 / +3.196

Table 20. Voltage Regulation Verification Record.

As you can see, the voltage regulation test circuit performed as expected, stepping down all voltages ±6 V and greater to the required voltage. These voltages yielded an error of only ±0.2%, well below the required ±3%, verifying that the voltage regulation circuit was working correctly. For all supplied voltages ±5 V and below, as would be expected, the voltages fell below the voltage required for the QRS11 to operate correctly as specified by the manufacturer. Further experimentation determined that the minimum

input supply voltage from the ACS needed to provide the required ±5 V ±3% to the QRS11s was ±5.45 V. If this error requirement is decreased to a more accurate voltage such as ± 0.4%, the minimum supply voltage needed would be ± 5.75 V. Therefore, to ensure an error of less than 0.4%, we must ensure that the supply voltage provided by the ACS board never falls below ±5.75 V. For the NPSAT1 mission, the MEMS will be receiving ±6 V from the spacecraft bus, well above this threshold.

D. NOISE FILTERING TECHNIQUES

The primary requirement of the filter was to remove the noise spikes seen in the FFT from Figure 40 and to decrease the low frequency noise seen in the 100 Hz pass band of the sensor. Due to the higher frequencies of these spikes, the best method to achieve these ends is to use a low pass filter. Also, we needed to try to reduce the overall noise range of the rate bias seen in Figure 39, without corrupting the accuracy of the rate data output from the sensor. This further constrains the requirements of the low pass filter by requiring the selected filter to ensure it does not induce noise into the pass band. Induced noise in the pass band takes the form of a ripple, and yields an unrecoverable bias in the rate output. Listed below are a few potential low pass filters considered for use in the MEMS filtering scheme [28].

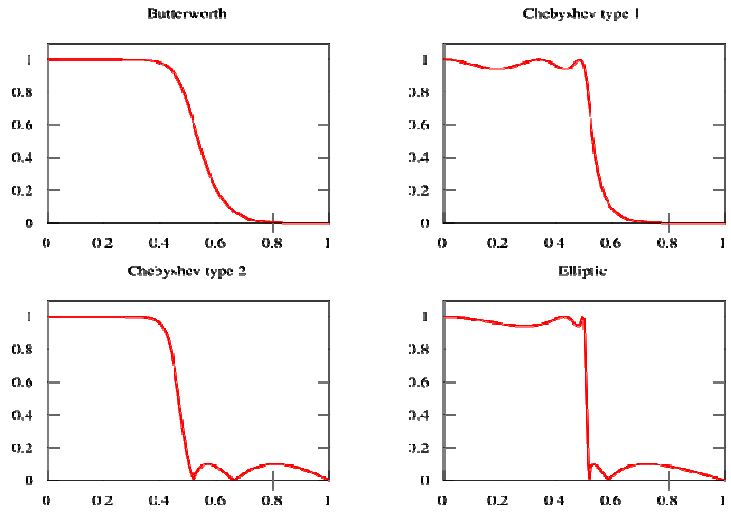

Figure 45. Potential Low Pass Filtering Techniques.

As you can see from Figure 45, the Butterworth low pass filter offers a clean and ripple free pass band as well as stop band. It achieves this, but has a slightly wider transition band compared to the other types of low pass filters [29]. Both the Chebyshev Type 1 low pass filter and the Elliptic low pass filter have smaller transition regions than the same order Butterworth filter, at the expense of ripples in the pass band. This will induce unwanted bias into the signal outputs of both types of filters. Therefore, neither of these filters is desirable for the purposes of this experiment. Like the Butterworth, the Chebyshev Type 2 low pass filter is a valid candidate. It has a ripple free pass band, and a much narrower transition band compared to the Butterworth, but it does have ripple in the stop band. This should have no effect on the pass band, and can be more or less ignored.

Therefore, the two potential candidates for filtering were the Butterworth and the Chebyshev Type 2. The pass band is the most important characteristic when comparing the two filtering techniques, and both filters perform similarly in this band. The transition band and the stop band of both filters are less important, and their differences can be somewhat neglected. With all else equal, it was determined that the Butterworth low pass filter, with ripples in neither the pass or stop band, was less risky than the Chebyshev Type 2, and was selected for use in the PCFB.

E. NOISE FILTER TESTING

With the selection of a Sallen Key Low Pass Butterworth Filter (SKLPBF), a filter diagram was created to graphically depict the layout of the filter design. To select the component values for the circuit resistors and capacitors, we needed to select a cut off frequency for the filter. To ensure that all the higher frequency noise spikes, as well as any possible induced noise would be removed from the sensor's outputs, a 1 Hz cut off frequency was selected for the filter. Another driving factor for the selection of this cut off frequency stemmed from the characteristics of the sensor itself. The QRS11 rate sensors are able to measure up to ±5°/s, this is equal to 5/360° = 0.014 Hz. Changes at these rates are expected to be small and slow, taking many seconds. Therefore, the lower

the cut off frequency the better. Component values were calculated based on this cut off frequency, and their values as well as the final filter design can be seen below.

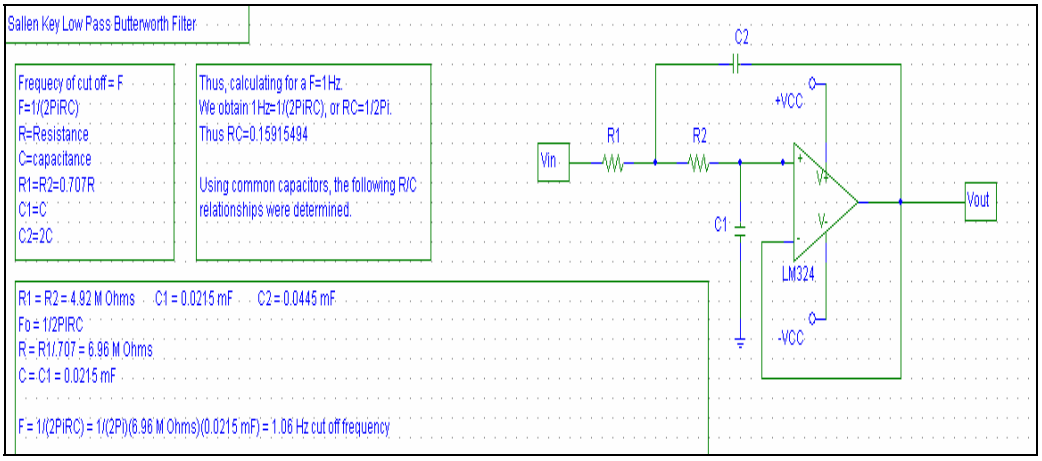

Figure 46. Sallen Key Low Pass Butterworth Filter Design.

Based on this, a test filter was constructed to verify the filter's performance characteristics. This filter can be seen in Figure 47. This sensor was powered by a calibrated power supply, and a signal generator provided an input signal to filter. Using the Agilent scope, the filter was observed to filter high frequencies.

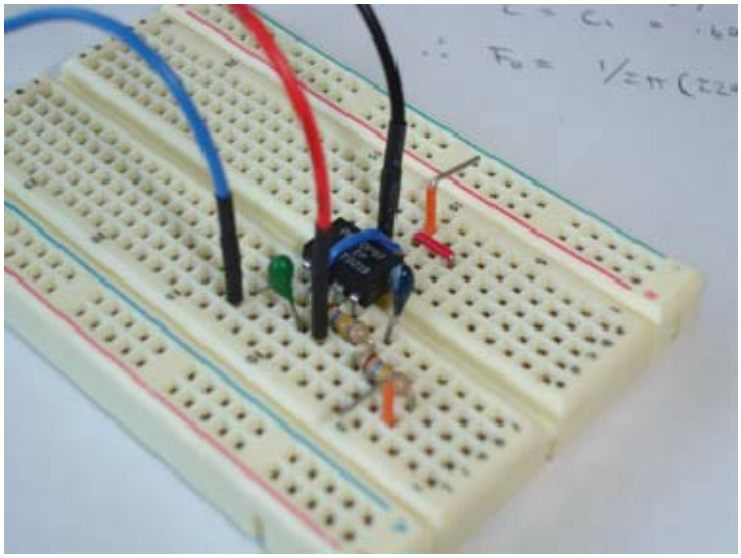

Figure 47. Sallen Key Low Pass Butterworth Filter Picture.

1. Description

With the modification of the PRCB presented in the last paragraph implemented, and noise due to power negated, the next step in the design of the PCFB was taken. It is generally known that filtering and buffering or amplification should be done as near to the signal source as possible. The low pass filter was added to the rate, BIT, and temperature outputs of the PRCB. The PCFB filter schematic was then updated to incorporate not only the voltage regulator and power filter, but a low pass Butterworth filter as well. This schematic can be seen below in Figure 48.

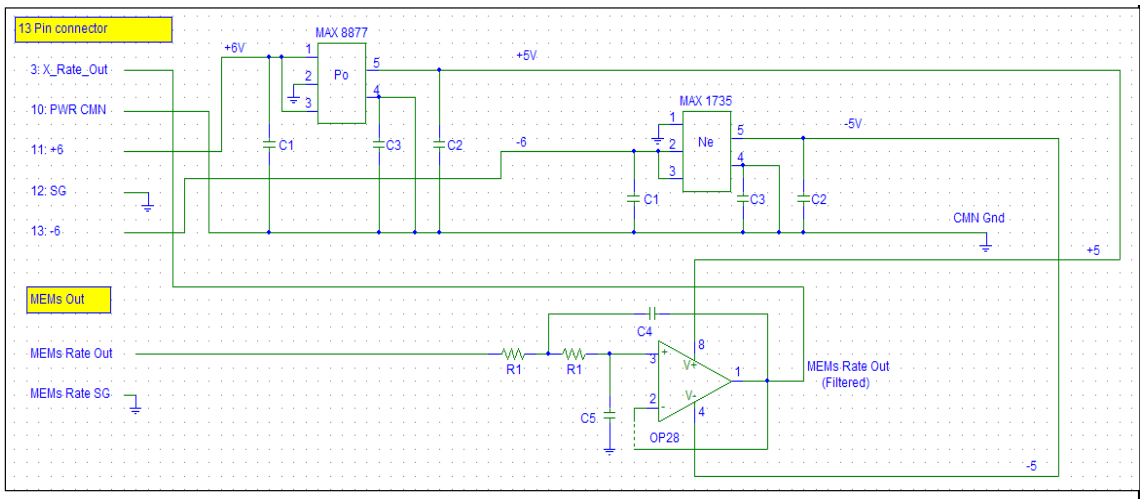

Figure 48. PRCB Circuit with Integrated Low Pass Filter Schematic.

The test board from the PRCB voltage regulator and power filter circuit test was combined with the SKLPBF circuit on a separate low noise test board. The circuit was then tested for connectivity, and can be seen below in Figure 49.

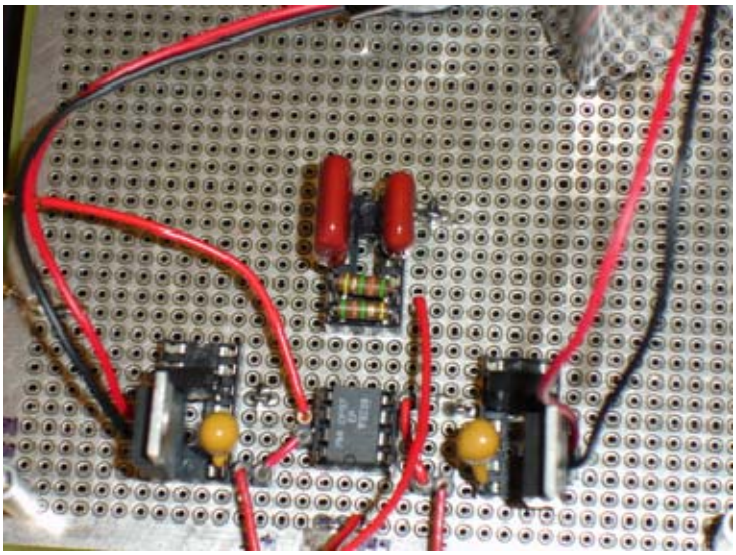

Figure 49. PRCB Circuit with Integrated Low Pass Filter.

2. Testing

The test board was placed on the experimentation test bench. A calibrated power supply was used to provide the power and voltage regulator and filter with ± 6 V, as it would from the ACS board. An input AC voltage from the signal generator was attached to the filter input to provide a test signal. The Agilent scope was attached to the filter output using a pair of low noise probes, and a characterization test of the noise filter was then conducted to confirm its characteristics. The signal generator voltage was applied to the filter input while the frequency range of the input was adjusted from 0 to 100 Hz. The phase shift and filtered voltage outputs are recorded below in Table 21.

Hz Range	Base (V))	Filtered (V)	Phase (°)	Error (dB)	dB
0.1	4.54	4.55	7	0.001	0.01
0.2	4.54	4.53	14	0.001	-0.01
0.3	4.54	4.52	24	0.001	-0.02
0.4	4.54	4.49	32	0.001	-0.05
0.5	4.54	4.44	41	0.001	-0.10
0.6	4.54	4.33	51	0.001	-0.21
0.7	4.54	4.15	61	0.01	-0.39
0.8	4.54	3.90	70	0.01	-0.66
0.9	4.54	3.69	80	0.01	-0.90
1.0	4.54	3.40	90	0.1	-1.26
2	4.54	1.16	133	0.6	-5.93
3	4.54	0.58	150	0.9	-8.91
4	4.54	0.30	160	1.1	-11.76
5	4.54	0.19	?	1.4	-13.72
10	4.54	0.05	?	2	-19.67
20	4.54	0.02	?	3	-24.27
100	4.54	0.01	?	15	-28.12

Table 21. Filter Characterization Results.

The filtered voltage begins to fall off shortly before the 1 Hz frequency, achieving a response of about -1.26 dB at 1 Hz, and then quickly dropping the output to around -20 dB at a frequency of 10 Hz, which is a characteristic of a single pole low pass filter. The 90° phase shift at a frequency of 1 Hz is also characteristic of this type of filter. Areas of the table highlighted in red denote questionable or unreadable measurements at the low end of the equipment's resolution. Figure 50 shows the plot of the filtered output vs. frequency where these characteristics are easier to visualize. As you can see, compared to a steady input voltage, the output voltage falls off significantly after the 1 Hz cut off frequency.

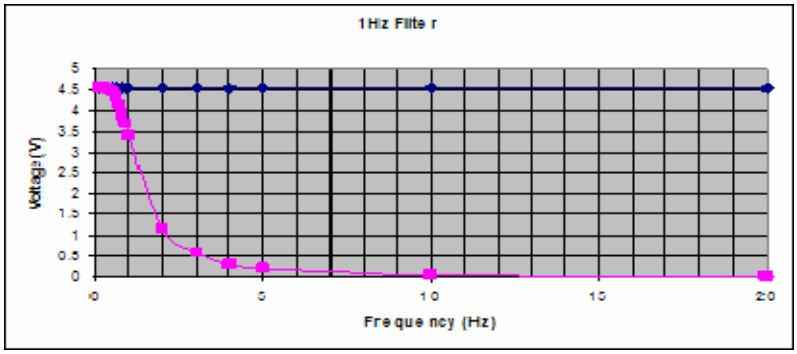

Figure 50. Voltage Input vs. Filtered Input.

The frequency vs. response in dB of this filter data was then plotted in Figure 51 below, and compared to the theoretical performance plot of a single pole low pass filter seen in Figure 52. A single pole Butterworth low pass filter (first order filter) should roll off at about -6 dB per octave, or -20 dB per decade. This theoretical response of the single pole filter was plotted below as a pink line. Error bars were included with the data to account for inaccuracies of the measurement equipment at very low rates. As you can see, the experimental data plot fits the theoretical plot up to 10 Hz. Above this frequency some divergence from the theoretical plot was seen, perhaps attributed to errors due to resolution of the measurement equipment at such very low voltages outputs, which are quickly approaching zero.

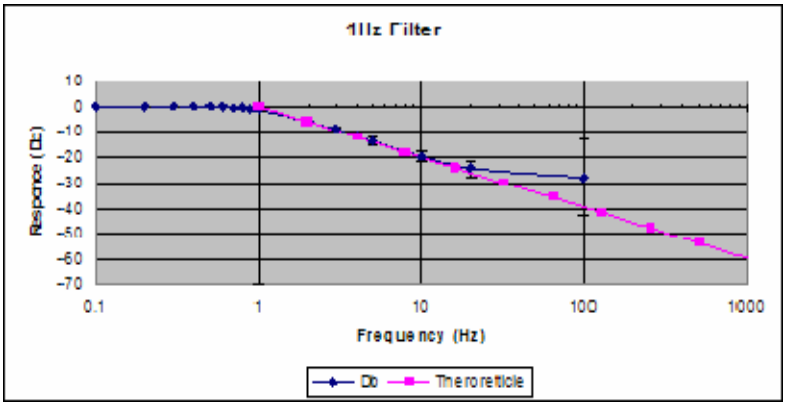

Figure 51. Filter Response Curves.

Figure 52 shows the theoretical plots of response in dB vs. frequency for each order of a low pass filter. The filter currently being used is a 1st order filter, and the data we see above matches this plot. Therefore, if this filter works as it should, the response of the noise spikes we saw in the raw MEMS noise FFT should be greatly reduced. Extrapolating from the Figure 52 to incorporate our noise spikes, it was calculated that the noise spike seen at approximately 262 Hz in Figure 40 should have a response of about -49 dB, and the noise spike at approximately 786 Hz should have a response of about -57 dB. The desired response for the experiment was determined to be approximately -50 dB [30]. So the noise filter should meet the needs of the experiment.

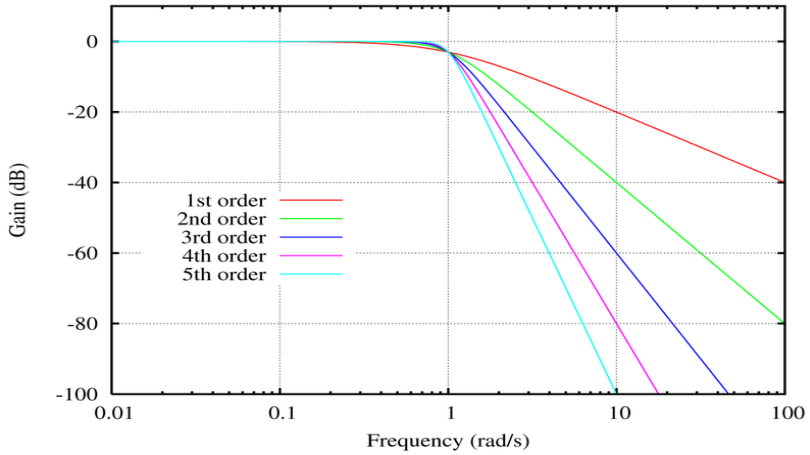

Figure 52. Theoretical Filter Response.

3. Results

With the promising results achieved from the above testing of the filter, it was now time to integrated the 1 Hz test filter into the voltage regulator and power filter circuit, and run a test to verify that the filter was stripping out the QRS11 noise spikes without inducing any new bias. Prior to doing this, the Agilent scope was used to capture a representative sample of the sensor noise into the PRCB test board with voltage regulator and power filter (Configuration 2) prior to connecting the low pass filter. The following data was taken at 5K samples/sec:

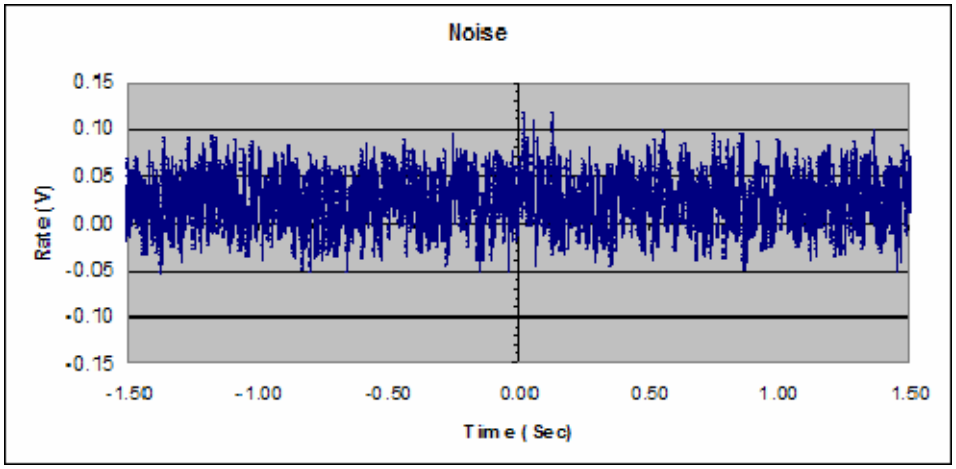

Figure 53. MEMS Power Filtered Rate Output (Zero Rate).

As you can see, this is fairly similar to the non-filtered noise chart seen in Figure 39, with some overall improvements. These improvements are due to the addition of the voltage regulator and power filter to the test circuit. Bias due to temperature is still the primary reason for the 29 mV of offset we see, and will not be removed until we integrate the bias control algorithms determined from the thermal bias testing of the flight structure. The average dynamic range of the noise has been reduced slightly from about 188 mV of the original unregulated and unfiltered signal to about 160 mV, a 15% decrease in the peak-to-peak noise. The standard deviation remained constant at 25 mV, and this, coupled with the decrease in peak-to-peak noise, is indicative that some of the noise seen in Figure 39 may be caused by noise induced through the power input. This would explain why the integration of the voltage regulator and power filter yielded a cleaner and more accurate output signal.

Next, the low-pass filter was integrated and connected into the test circuit, and again the Agilent high end scope was used to capture a representative sample of the internal noise of the output signal of the PCFB test board. As you can see from Figure 54 below, bias due to temperature remains unchanged at about 29 mV. But the average peak-to-peak noise has been reduced from about 188 mV of the original unregulated and unfiltered signal, to only 11 mV, a 94% decrease in peak-to-peak noise. Additionally, the standard deviation of the signal was reduced from 25 mV to only 2 mV, a decrease of 92%. As you can see, this dramatically improved the overall signal quality, though some low frequency noise is still evident in the data. Effects due to temperature may be neglected due to the short test cycles, typically 3 seconds.

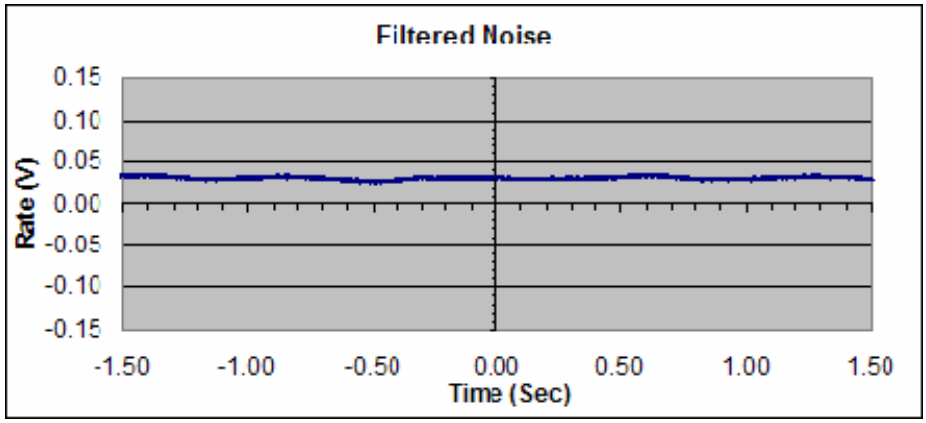

Figure 54. MEMS Power Filtered Rate Output with Low Pass Filter.

This data was then taken and a distribution was again constructed from the data, and the results can be seen below in Figure 55. As you can see, the filtering has had a dramatic effect on the original noise distribution curve seen in Figure 41. The Gaussian curve still fits the histogram, but the noise is clearly reduced.

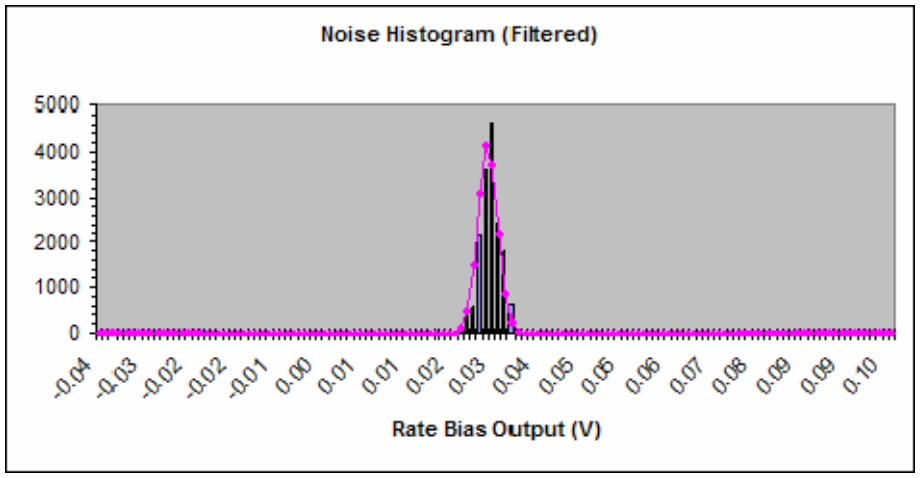

Figure 55. PCFB Gaussian Plot.

Below is the FFT of this filtered noise. As you can see, the two spikes we saw earlier at approximately 262 Hz and 786 Hz from Figure 40 are gone. What we do see is a rapid roll off of the noise above the 1 Hz frequency, and then a level response level of ≤

-80 dB. This is slightly better than what was expected, and tells us that the filter is working basically as anticipated. From the theoretical plots in Figure 52, we expected to see a response of -49 dB at the 262 Hz frequency spike, and a -57 dB response at the 785 Hz frequency spike. Instead we saw an approximate response of -58 dB at the 262 Hz frequency spike, and an approximate response of -63 dB response at the 785 Hz frequency spike. This better than expected response may be attributed to the addition of the voltage regulator and power filter circuit to the Butterworth low pass filters.

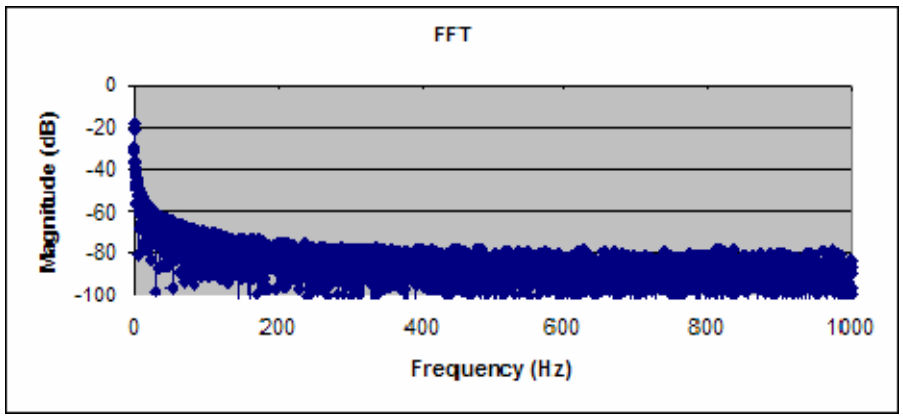

Figure 56. MEMS FFT Filtered.

F. PCFB DESIGN

From what was learned through the research already presented in this chapter, we knew that a PRCB redesign was needed. Expanding on the original PRCB design, we decided to modify the existing voltage regulator and power filter circuit, as well as include a SKLPBF for the rate output, temperature output, and the BIT outputs. In addition to these modifications, we also decided to amplify the temperature output to improve the signal-to-noise ratio of the temperature output.

From the data collected in the bias vs. temperature testing, we saw that the temperature output produced voltages from -0.3 V to +0.1 V for a temperature range of -60°C to +50°C. This range is reduced even further as the expected operational temperature range of the MEMS sensor suite, calculated from the thermal analysis of the spacecraft and its subsystems, is predicted to only be -11°C to +9°C. So it was decided to

first filter and then amplify the temperature output by a factor of 13. The schematic representing these circuits is shown in Figure 57 below.

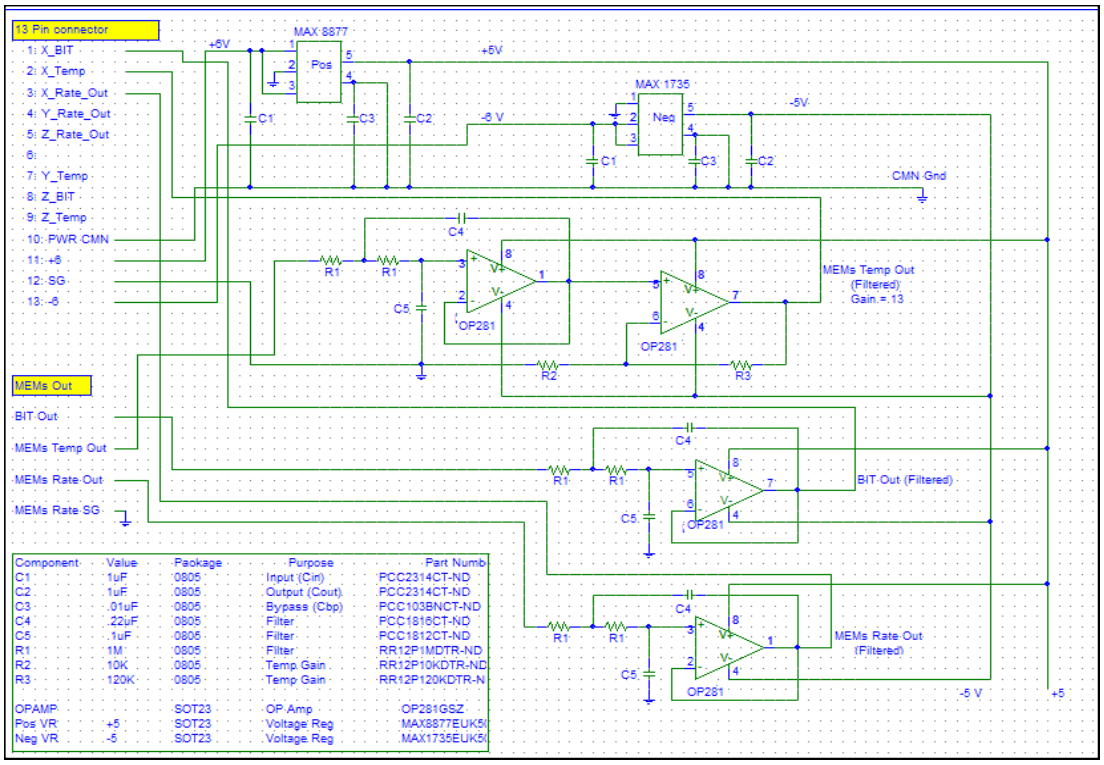

Figure 57. MEMS PCFB Electrical Schematic.

1. Initial PCFB Design

To implement the circuit schematic, and build a test PCFB, research was conducted on the potential components to determine which would meet not only the requirements of the circuit, but of the temperature environment as well. These parts were then selected and ordered, and are listed in Figure 57 and 58. The considerations for selection where threefold: First, the parts needed to be small, able to all fit onto a surface of approximately the same size as the original PRCB, approximately 1.5 sq in. The PCFB must not only fit onto the QRS11, but in the MEMS housing and on the MEMS tri-axial mount as well. Second, the characteristics and precision of the components needed to be of the best possible grade. Third, the components must meet the required power, accuracy, and temperature requirements of the spacecraft itself. With the parts

selected, an initial five times scaled PCFB sketch was constructed on a piece of paper using scaled part sizes to determine a rough layout of the overall PCFB, as well as to verify that all the components would fit onto the small surface of the PCFB. This sketch is shown in Figure 58.

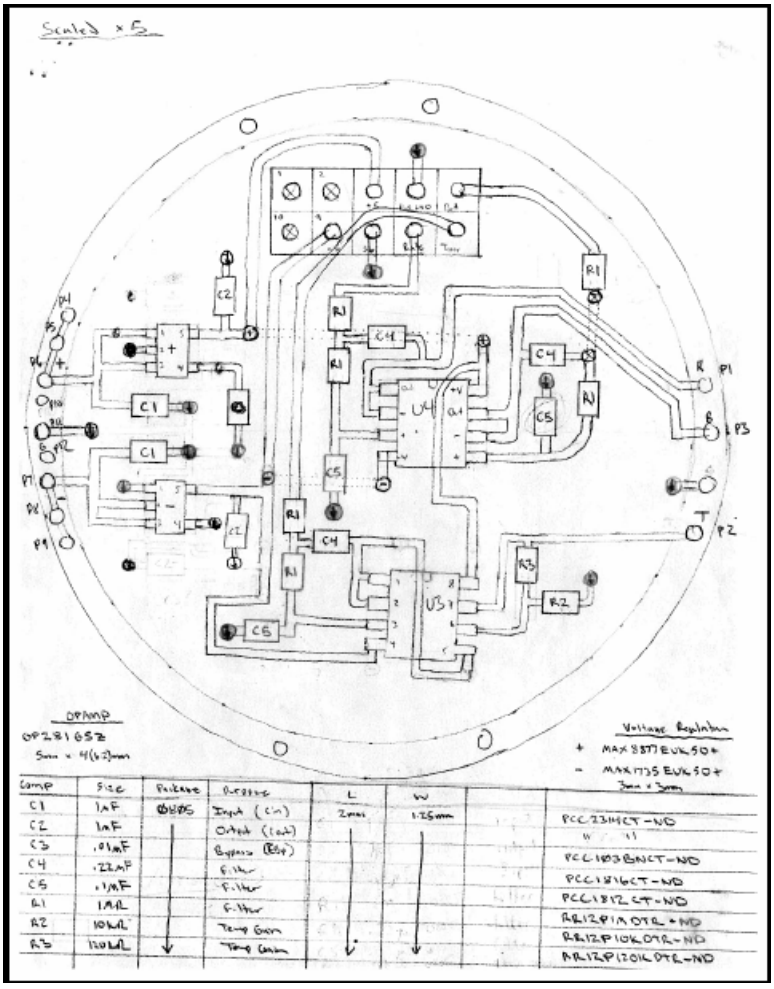

Figure 58. MEMS PCFB Initial Sketch.

2. Final Design

With the initial circuit schematic, parts selection, and sketch in hand, the PCFB was designed in-house with the assistance of David Rigmaiden utilizing CAD design program produced by Texas Instruments called FilterPro. The layout process took a couple of days. The completed PCFB layout was then systematically reviewed by the

members of the design team over the next couple of days, and a few additional modifications were integrated into the design. The layout of the complete PCFB can be seen below in Figure 59, and the design was sent out for manufacturing by Advanced Circuits, with a total of ten PCFBs being purchased for a total of $496.15.

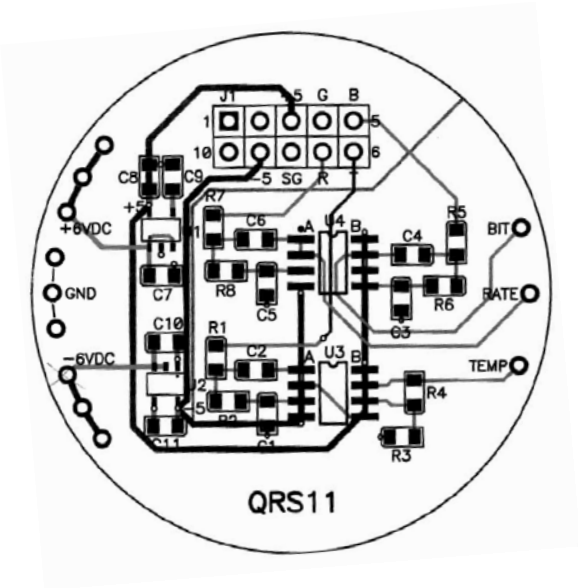

Figure 59. MEMS PCFB Final CAD Diagram.

The final PCFB is a four layer board of radius of 0.85 inches, with a thickness of 0.062 inches. Like the original PRCB, it was designed to mount directly on top of each QRS11 sensor by soldering the ten pins of the sensor to the pin holes of the PCFB. This will keep the filters as close to the source as possible. The first layer (top), contains all the solder pads required to mount all 23 components to the PCFB, as well as many of the traces as possible. The second layer consists of the remaining traces. The third layer is the grounding plane, connected to the numerous surface grounding points through vias. The fourth layer is the bottom substrate layer.

G. PCFB BUILD

The ten PCFBs were received from the manufacturer. A simple visual inspection and connectivity test was conducted to ensure the pins and leads of the PCFB were built

to specifications. One PCFB was built and verified to be operational. After this, three more test boards were placed on a clean surface, and cleaned in preparation for building. The soldering gun was turned on, set to 700°F, and solder and flux were set in easily reachable locations. Next, a cut out CAD diagram of the PCFB was placed on the work bench, and all components were placed on to it in their respective positions. Each component was then measured, verifying that the component fell within specifications, and the results were then annotated in Table 22 below.

Component	Nominal Value	Actual Value (Test Board)	Actual Value (-X Axis)	Actual Value (Y Axis)	Actual Value (-Z Axis)	Part Number
U1	ACRS					MAX887EUK50+
U2	AD0Z					MAX1735EUK50+
U3	OP281					OP281
U4	OP281					OP281
C1	.10 uF 25V 0805 10%	0.096	0.092	0.093	0.095	PCC1812CT-ND
C2	.22 uF 16V 0805 10%	0.202	0.206	0.202	0.202	PCC1816CT-ND
C3	.10 uF 25V 0805 10%	0.098	0.093	0.091	0.094	PCC1812CT-ND
C4	.22 uF 16V 0805 10%	0.202	0.203	0.202	0.207	PCC1816CT-ND
C5	.10 uF 25V 0805 10%	0.098	0.094	0.094	0.094	PCC1812CT-ND
C6	.22 uF 16V 0805 10%	0.206	0.202	0.207	0.203	PCC1816CT-ND
C7	1 uF 25V 0805 10%	0.890	0.907	0.883	0.855	PCC2314CT-ND
C8	1 uF 25V 0805 10%	0.890	0.876	0.896	0.889	PCC2314CT-ND
C9	.01 uF 16V 0805 10%	0.010	0.010	0.009	0.009	PCC103BNCT-ND
C10	1 uF 25V 0805 10%	0.890	0.897	0.899	0.892	PCC2314CT-ND
C11	1 uF 25V 0805 10%	0.890	0.878	0.906	0.849	PCC2314CT-ND
R1	1.0 Mohm .1W .5%	1.008	0.997	0.996	0.995	RR12P1.0MDCT
R2	1.0 Mohm .1W .5%	1.008	0.995	0.995	0.996	RR12P1.0MDCT
R3	10.0 Mohm .1W .5%	10.100	10.010	10.000	10.000	RR12P10.0KDCT
R4	120 Mohm .1W .5%	120.400	120.000	120.000	120.000	RR12P120KDCT
R5	1.0 Mohm .1W .5%	1.008	0.996	0.996	0.995	RR12P1.0MDCT
R6	1.0 Mohm .1W .5%	1.008	0.995	0.995	0.996	RR12P1.0MDCT
R7	1.0 Mohm .1W .5%	1.008	0.996	0.996	0.996	RR12P1.0MDCT
R8	1.0 Mohm .1W .5%	1.008	0.996	0.996	0.996	RR12P1.0MDCT

(Test): Used Micronta, Radioshack 22-163, Built 06/26/2007, 6 wires, test connector.
(-X Axis): Used Micronta, Radioshack 22-163, Flight Built 07/8/2007, 7 wires, test connector, conformal coat.
(Y Axis): Used Micronta, Radioshack 22-163, Flight Built 06/12/2007, 7 wires, test connector, conformal coat.
(-Z Axis): Used Micronta, Radioshack 22-163, Flight Built 06/27/2007, 7 wires, test connector, conformal coat.

Table 22. PCFB Component Build Record.

Using a magnification lens and an assortment of precision tools, each component was then placed on the PCFBs and soldered into place. Each solder was then carefully inspected prior to starting the next component. Once the three PCFBs were complete, they were cleaned and visually inspected. A completed PCFB can be seen in Figure 60 below.

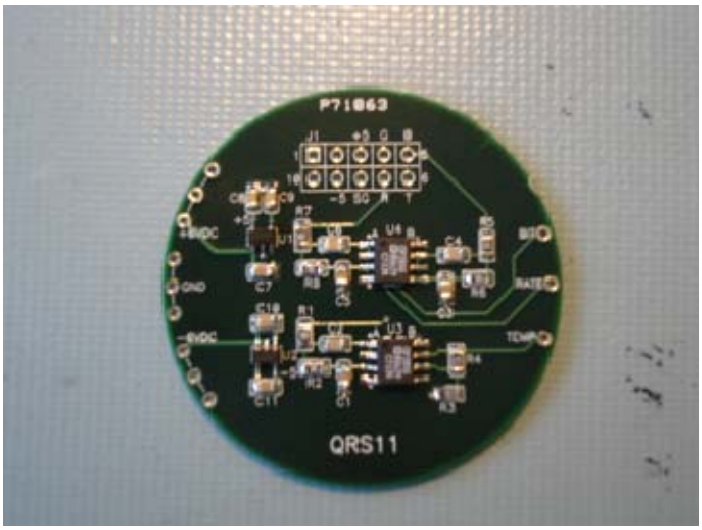

Figure 60. Completed PCFB.

H. PCFB BUILD VERIFICATION AND TESTING

After the three test PCFBs were constructed, they needed to be put through a series of simple tests to verify that they were properly constructed, and that they were meeting their design performance requirements. These tests included a simple voltage regulation test, a connectivity and grounding test, and an output test. The tests were designed to verify that all components were functioning properly, that the PCFBs had good connectivity from input to output, and that there are no shorts or dead leads. These tests were not designed to quantitatively measure the performance of the PCFBs. Such tests will come later.

Each of the three PCBs was mounted in a table clamp on the test bench, and a calibrated power supply was used to provide each PCFB with +6.0 V, -6.0 V, and a common GND. A calibrated multi-meter was placed on the table along with the test records in preparation for the following tests. A picture of this test setup can be seen below in Figure 61.

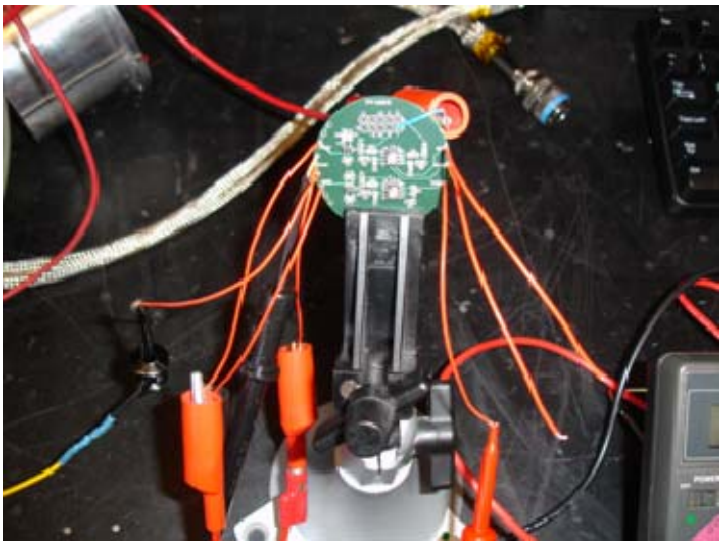

Figure 61. PCFB Build Verification Test Set Up.

Using a calibrated multi-meter, the voltage into the Pin 3 hole (+5 V) was tested and verified as +5 V for each PCFB. Likewise, the voltage into the Pin 9 hole (-5 V) was tested and verified as -5 V for each PCFB. This verifies that the voltage regulators are functioning properly on each PCFB.

Next, the calibrated multi-meter was connected to the rate output hole, and with floating input, an arbitrary rate output was observed. With a test lead, the rate Pin 7 (rate) output hole was grounded to the common ground of the PCFB, and the filtered rate output was observed to drop to zero. This was conducted for each of the three PCFBs, and confirms that the rate output filters are functioning as expected. This test was then repeated for both the BIT and temperature outputs, confirming that they too are showing proper operation for this test.

Next, a second power supply was integrated into the test setup to serve as a signal generator and provide a 1 V signal into the Pin 5 (BIT) hole. A calibrated multi-meter was used to measure the filtered BIT output, and was verified to be 1 V. This was done for all three of the PCFBs. This test was then repeated for the Pin 7 hole (Rate). These tests verified that the rate and BIT filter circuits produce unity gain and minimal bias under static signal conditions.

Next, the second power supply was set to provide a 0.2 V signal into the Pin 6 hole (Temperature), and a calibrated multi-meter was used to measure the output of the BIT lead. The temperature output from the PCFB is amplified with a gain of 13, and this was confirmed with the observed filtered and amplified temperature output of 2.6 V. This was conducted for all three of the PCFBs and verified proper operation.

I. CONCLUSION AND RESULTS

The purpose of this chapter was to minimize the noise of the MEMS sensor and to produce a cleaner signal prior to being sent to the ACS. To do this we focused our investigations on two specific areas, reducing noise due to power by voltage regulation and power filtering, and by developing a filtering scheme to remove the sensor's inherent noise. This was accomplished through the redesign and rebuild of the PRCB to include low pass filters for all three outputs, as well as an amplification circuit for the temperature output. The new PCFB greatly increases the capability and accuracy of the MEMS sensors, and in conjunction with the bias vs. temperature algorithms developed in Chapter IV, should negate most types of the known errors in the system. With the PCFB complete, it is time to integrate it into the MEMS angular rate subsystem and test the system under flight-like conditions to verify PCFB operation with the dynamic signals of the QRS11.

VI. FLIGHT BUILD AND CHARACTERIZATION TESTING

A. INTRODUCTION

Significant progress has been made in understanding the operations and capabilities of the QRS11 sensor, as well as how to optimize the sensor to maximize its potential utility to the spacecraft. These optimization techniques were implemented and tested on the test sensor, and proved to greatly improve the overall performance of the test sensor. If any further optimization is possible, it needs to be done through testing of the actual flight QRS11 MEMS rate subsystem, incorporating the improvements thus far.

Testing of the flight subsystem serves two purposes. Firstly, it will verify that the test results from previous chapters are repeatable with the 3-axis configuration of the flight sensors, and that these characteristics hold true for the flight sensors after integration into the flight assembly. This will yield a tested and verified, fully functional flight subsystem that is ready for acceptance and qualification testing. Secondly, having incorporated the improvements learned during this thesis research, it will provide a flight-like system on which further testing and optimization of the sensor could be performed.

B. MEMS SUBSYSTEM COMPONENT ASSEMBLY

This section describes the build of the flight-like subsystems that will allow a move to more detailed testing. Testing of the MEMS assembly will now include the flight QRS11 sensors, the new PCFBs, and the flight harness, enabling the MEMS subsystem to be tested under the most flight like conditions possible. To do this, the two major components of the MEMS subsystem must first be constructed, the sensor suite itself, as well as its wiring harness.

1. MEMS 3-Axis Rate Sensor Assembly

Following assembly of the three PCFBs and their basic operations verified, they were mounted to the MEMS sensor suit in a flight-like configuration in accordance with the MEMS Build Procedures. These procedures are included in Annex B. The two variations from these procedures are the use of connector headers in lieu of permanently

soldering the PCFBs to the QRS11 sensors and not using thread tight on any of the bolts. This allows the MEMS subsystem to be opened and the PCFBs removed if needed, which would prove useful in follow-on testing and modifications. Other than this, the MEMS subsystem utilized only flight hardware. Below is a picture of the MEMS assembly prior to the addition of the housing and nitrogen purge.

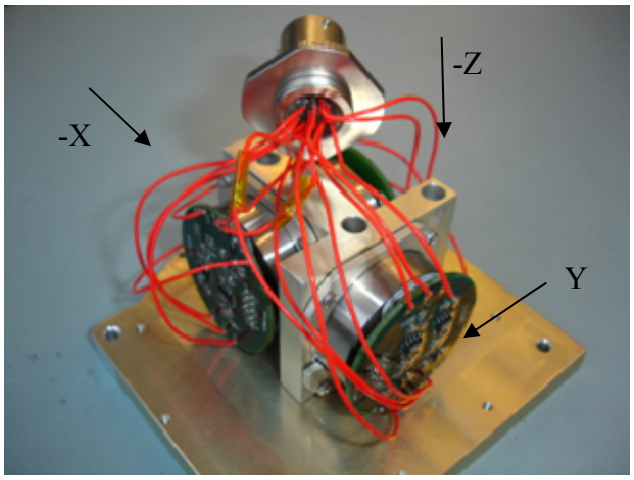

Figure 62. MEMS PCFB Integration.

2. Wiring Harness Assembly

The flight harness was constructed in accordance with the Flight Harness Build Procedures, included in Annex A. Unlike the MEMS build, the flight harness was constructed to the exact build procedure specifications and could be the actual space flight harness. The flight harness can be seen in Figure 63 integrated into the complete MEMS assembly.

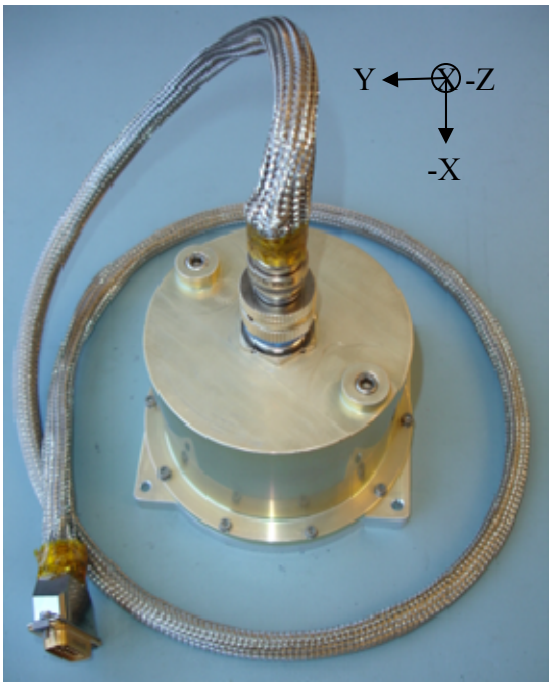

Figure 63. Completed Flight Subsystem.

C. MEMS FLIGHT SUBSYSTEM TESTING

The MEMS subsystem was mounted to the HAAS TRT, ensuring that the –X axis sensor sense axis (curved edge) was aligned with the orientation markings of the rotation table. The sense axes are provided, where the O/X symbol represents the –Z into the page. Ensuring that the 13-Pin connector was firmly seated and locked to the MEMS assembly, the 15-Pin side of the flight harness was then connected to the test interface bracket of the test bench. A picture of the complete set up can be seen below in Figure 64.

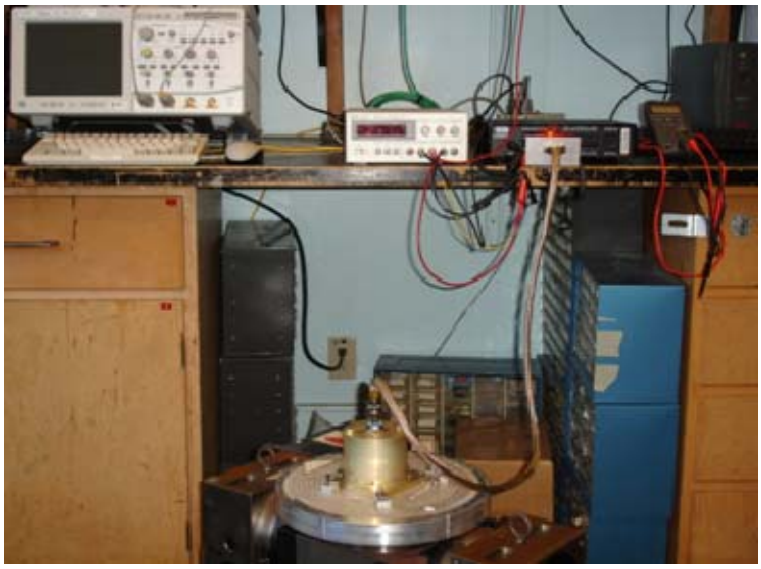

Figure 64. MEMS Subsystem Testing Setup.

Using the calibrated multi-meter, the power supply was set to ± 6.00 VDC, matching the voltage that would be supplied to the MEMS by the spacecraft bus, and was then turned off. The power supply was then attached to the MEMS test bracket, insuring that the +6 V, -6 V, and common ground leads were correctly attached to the respective test connector pins. Next, the 12 leads of the test interface bracket were connected to their respective channel ports of the WebDAQ as shown in the WebDAQ setup described in Chapter III. After verifying that all leads were correctly connected, the WebDAQ was powered on to ensure connectivity. The WEBDAQ was then programmed to sample and average data at 200 Hz, the planned sampling frequency of the ACS, and set to display and record results every second.

It is important to note here that each sensor has its own individual characteristics, and that there are variations between the individual sensors in operating temperature output, bias, and BIT outputs. These variations are not indicative of errors in the sensors, but rather of slight variations between sensors due to manufacturing, and will be compensated for by determining the individual sensor bias compensation values.

1. Startup and Operations Test

This test was run to verify that the overall design requirements and characteristics of the MEMS were being met, and that the flight MEMS assembly was meeting the anticipated performance characteristics as discussed in previous chapters. Areas of interest here included the verification of proper voltage regulation, an operational BIT output, accurate rate output, as well as a properly amplified temperature output. With the initial set up complete, the Python interface program was set to acquire data every second for three minutes, and the Python program was started. After 30 seconds, the power supply was turned on, and the data outputs of all three sensors were recorded for the next 2.5 minutes. The recorded data included Rate, Temperature, and BIT data. The first obvious check is to verify that the BIT outputs from each sensor yield nominal outputs. The BIT outputs for all three sensors can be seen below in Figure 65.

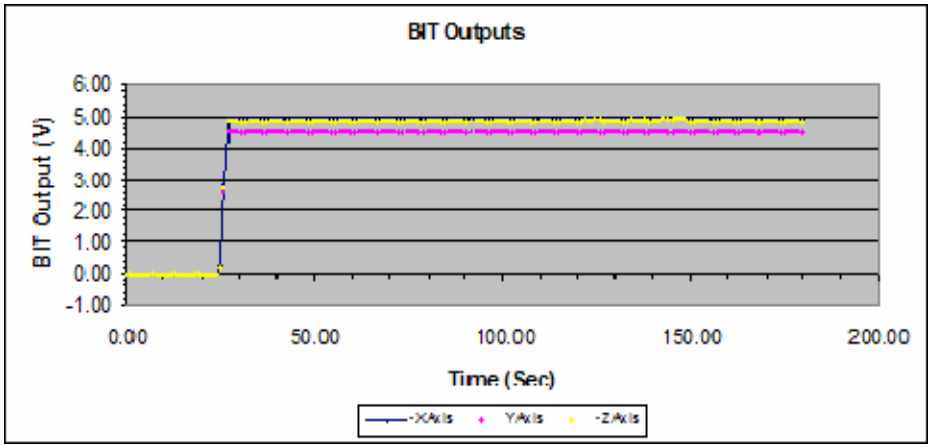

Figure 65. BIT Startup Profile.

With the power off, the first 30 seconds of the test yielded a BIT output of less than 0.8 V (a logical 0). Once the power was turned on, all three sensors reported a functional state within one second, represented by an output voltage of greater than 2.4 V (the logical 1). From past experience, the typical BIT output was around 4.5 V, as it is here. This BIT start up profile is the same every time the QRS11 is powered on, and indicates that the QRS11 sensors as well as the BIT output of the PCFBs are functioning correctly.

The rate startup profile data was then analyzed and compared to past experimental results. From past experience, a short spike in the rate output of all three sensors is expected when the power is turned on, followed by a fairly consistent rate output of about 30 to 50 mV, which would slowly drift down about 10 mV over the first 2 minutes as the sensors warm up to operating temperature. This rate startup profile can be seen blow in Figure 66.

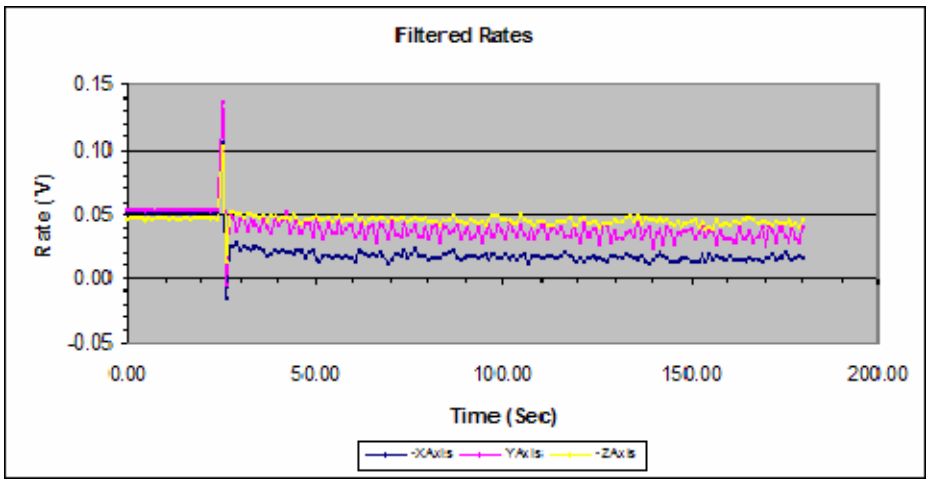

Figure 66. Rate Startup Profile.

These results match what was expected. All three sensors had initial bias values ranging from 20 to 50 mV. The –X axis had the smallest bias value of 28 mV, followed by the Y axis at 45 mV, and the –Z axis at 50 mV. These bias values rolled off as expected, slowly drifting down about 10 mV over the first 2 minutes. The variation in bias for each sensor is a manufacturing characteristic, which requires the computation of bias compensation values for each sensor.

Another artifact seen in Figure 66 is the periodic noise in the rate output of the Y axis sensor. This error persisted through this test series, as well as the noise and characterization testing presented later. This posed a potential problem as an unknown source of error, and was investigated further following the conclusion of this test series. Through additional tests and trouble shooting, this noise was determined to be the result

of a connection problem between the PCFB and the Y axis QRS11 sensor. This was determined by removing the PCFB, and switching the –X and Y axis sensors. The PCFBs were then re-attached to their original locations, independent of the sensors. Due to the length of the test series (over 100 hrs), a truncated version of the tests conducted in this chapter were repeated.

What we saw was the noise spikes seen in the Y axis sensor were gone. The results of this test yielded a plot of the Y axis sensor much like what was observed in both the -X and –Z axis sensor plots seen in Figure 66. The –X and Y outputs seen in the first test series were now swapped in the second test series, yet their results matched perfectly with what was observed in the original test, minus the noise spikes. This suggests that the sensors themselves are mechanically consistent, and that bias and temperature move with the sensor, and are not affected by the PCFBs, which function the same regardless of the sensor they are attached to. The sensors were switched back to their original positions, and another set of truncated tests were conducted, confirming these test results. The noise seen in the Y axis sensor was gone, a result of a poor connection between sensor and PCFB. This indicates that all three of the QRS11 sensors as well as the rate outputs of the PCFBs are functioning as expected for non-rotating sensors.

Finally, the temperature startup profile data was analyzed and compared to past experimental results. Voltage curves very similar to the rate output was expected, only inverted, and with a far smoother curve as the temperature of the sensor heated up to operating temperature over the first 2 minutes. In addition, an output temperature of roughly -0.70 V at room temperature for each sensor was expected. This value was calculated by applying the gain of 13 to the temperature outputs observed from earlier tests, typically -0.054 V for room temperature.

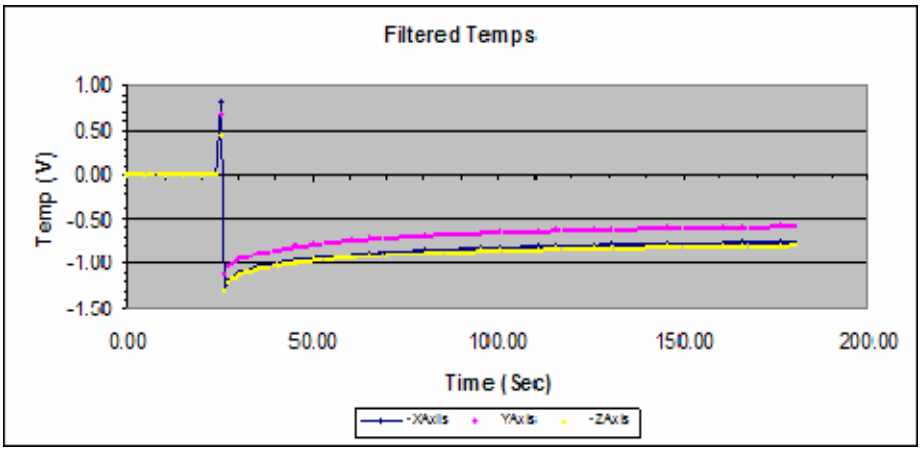

Figure 67. Temperature Start Up Profile.

As seen in Figure 67, the curves match with what was expected, and are similar to previous experience, accounting for the additional gain. All three sensors yielded temperature curves inverse to the bias curves seen in Figure 66, and all showed a gradual increase in temperature output as the sensors warmed up. The Y axis yielded the highest voltage of about -0.65 V, followed by the –X and –Z axis at about -0.80 V. This closely matches the -0.70 V we expected. As with bias, the observed variations in temperature output voltage between the three sensors was attributed to each sensors individual characteristic. These results indicate that the QRS11 internal temperature sensors as well as the temperature output and gain of the PCFBs are functioning as expected.

2. Noise Testing

This test was performed to verify that each PCFB was correctly filtering the MEMS rate outputs, and that the MEMS sensors were meeting their anticipated performance characteristics. Utilizing the same experimental setup as before, the MEMS assembly (Configuration 5) was powered on and allowed to warm up for five minutes. The WebDAQ was disconnected to ensure no noise was introduced, and the Tektronix Scope was used to capture a representative sample of the rate output at 1000 samples per second for all three sensor outputs for 20 seconds. These signals were then sampled and averaged in Excel at 200 Hz, and plotted in Figure 68.

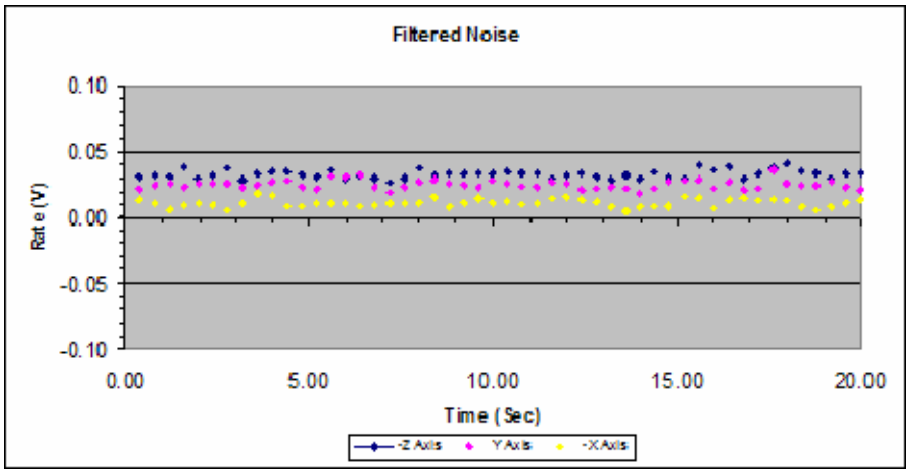

Figure 68. MEMS 3-Axis Rate Output.

As seen in Figure 68, all three sensors performed as expected from earlier testing using the QRS11 test sensor as documented in Chapter V, and resulted in average bias values very similar to what was seen for the test sensor. The –X sensor was observed to have a room temperature bias of 10.9 mV, with a standard deviation of 3.1 mV. The Y sensor had an average bias of 25.0 mV, and standard deviation of 3.3 mV, while the –Z sensor had an average of 32.8 mV and standard deviation of 3.1 mV. The average peak-to-peak range of these output signals was ±7 mV, very similar to what was observed with the test sensor. This indicates that noise is being filtered properly. To verify this, an FFT of the rate voltage data from each sensor was plotted in Figure 69.

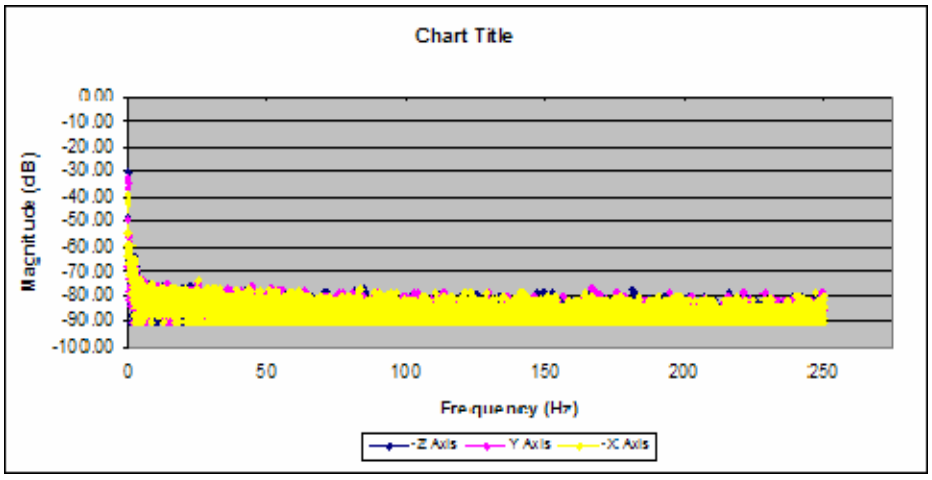

Figure 69. MEMS 3-Axis Rate Output FFTs.

The FFT of rate voltage for each sensor is as expected from testing of the QRS11 test sensor. The noise spikes at approximately 262 Hz and 786 Hz have been removed, and no unexpected noise has been introduced. This verifies that the flight PCFBs and MEMS subsystem is performing as expected, and is now capable of undergoing temperature characterization testing to determine the bias compensation values for each sensor.

D. MEMS CHARACTERIZATION TESTING

To convert raw MEMS rate data from each of the three flight sensors into the "corrected" data as described in Chapter IV, we need to compensate for the inherent bias of each sensor due to temperature. To do this, bias vs. temperature data are measured and cubic fit parameters were determined for each sensor. Six TVC tests, three above room temperature, and three below room temperature were performed. The six tests yielded a total of 113 hours of experimental data and covered a temperature range of over 55°C. A total of 13,000 data points from each sensor were used to construct the curves seen in Figure 70. Each of these data points is the average of 200 individual measurements conducted by the WebDAQ every second. Unfortunately, issues with the measurement and monitoring of the TVC during cooling cycles did not allow the chamber to achieve the desired qualification temperature ranges as discussed in Chapter IV. Fortunately, the

temperature ranges achieved were wide enough to more than span the expected operational range of the sensor, and the data was therefore useful.

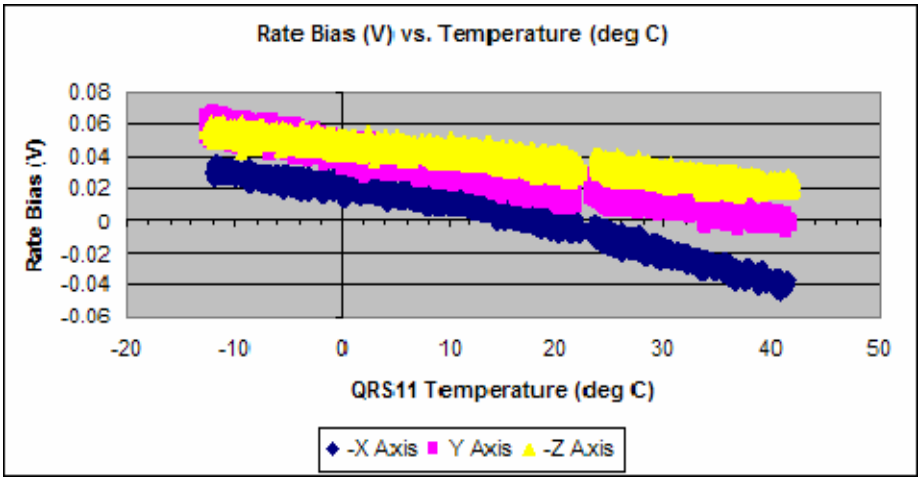

Figure 70. Flight Temperature vs. Rate (Wide Range).

The bias vs. temperature curves each have a slightly different shape. The –Z axis plot looks almost linear, while the –X axis looks to have a much larger divergence at higher temperatures than the other two sensors. In any case, the three bias vs. temperatures curves can be easily represented by a cubic function as before. There is a small gap in all three curves at the room temperature from which the tests were started. The sizes of these gaps were dramatically reduced from earlier tests by allowing the test to run longer, as suggested in Chapter IV. After compiling the bias vs. temperature data for these six tests, an Excel Linest function was used to generate the needed cubic bias compensation values for m3, m2, m1, and b for each of the three sensors. These bias compensation values can be seen below.

Sensor	m3	m2	m1	b
-X (062047)	0.001014	-0.007852	-0.047756	-0.027141
Y (062048)	-0.002785	-0.004087	-0.024304	0.012987
-Z (062046)	-0.001059	-0.002782	-0.015999	0.026439

Table 23. Flight Cubic Bias Compensation Values (Wide Range).

To verify the accuracy of these bias compensation values, the rate adjustment value for each of the 13,000 data point from the three individual sensors was calculated. In the following formula, $Y = m3*X^3 + m2*X^2 + m1*X + b$, Y is the rate adjustment value to be subtracted from the measured rate, X is the measured temperature, and m3, m2, m1, and b are given in Table 23. Y is then subtracted from the measured rates to yield an adjusted rate output, corrected for the temperature dependant bias, and is shown below in Figure 71.

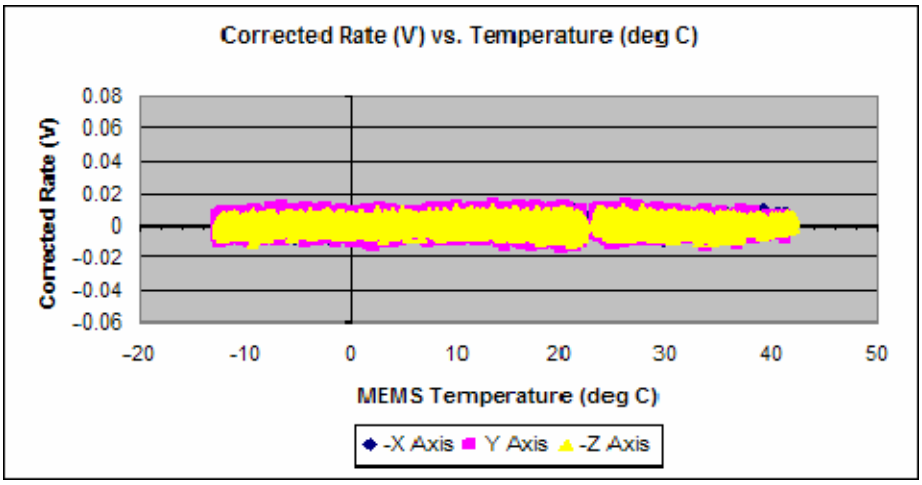

Figure 71. Corrected Rate vs. Temperature (Wide).

The corrected rate data averaged to 0.0000 V for each sensor. The –X axis sensor has a standard deviation of only 2.7 mV, while the –Z axis has a standard deviation of 2.8 mV. As expected, the Y axis saw a wider distribution than the other axis, as well as a higher standard deviation of 4.6 mV. This was due to the connector contact error mentioned earlier in this chapter. Once this problem was resolved, further testing showed that the peak-to-peak range of the Y axis seen in Figure 71 was reduced by nearly 40% to

the same level of both the –X and –Z axis sensors, as well as its standard deviation being reduced from 4.6 mV to 2.4 mV, again along the same level of both the –X and –Z sensors.

The operational temperature range of the sensors is expected to be between -11°C and +9°C. It may be that by limiting the range of data points used to calculate the cubic bias compensation values to the operational temperature may result in an improvement to the bias compensation values. Now looking only at data points falling in the expected operational temperature output range (-1.8 V to -0.9 V), an Excel Linest function was performed to generate the cubic bias compensation values for m3, m2, m1, and b for each of the three sensors. These bias compensation values are shown in Table 24.

Sensor	m3	m2	m1	b
-X (062047)	-0.004470	-0.020555	-0.049752	-0.021715
Y (062048)	0.016641	0.075200	0.080788	0.058187
-Z (062046)	-0.004815	-0.014171	-0.025366	0.025405

Table 24. Flight Cubic Bias Compensation Values (Operational Range).

These values were used to recalculate the corrected rate values for each of the data points in the operational temperature range. The corrected rates for the operational temperature range were then plotted in Figure 71 to verify that the new bias compensation values were accurately correcting for temperature.

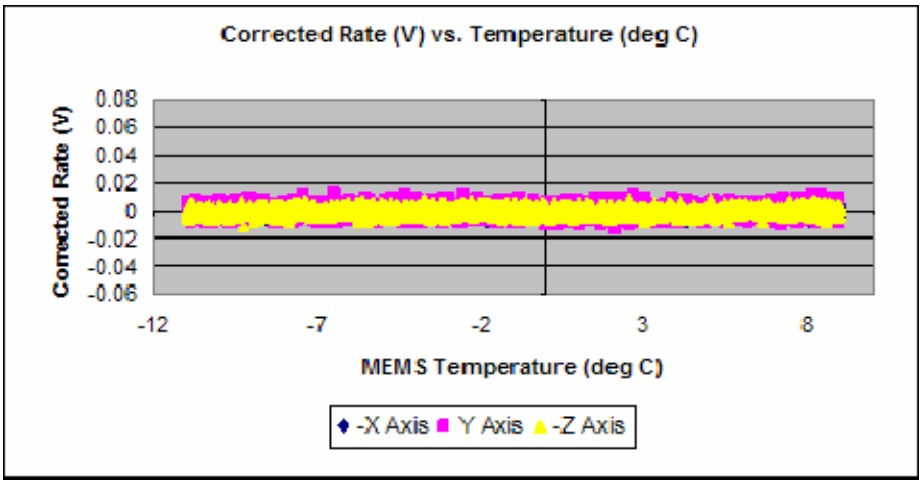

Figure 72. Corrected Rate vs. Temperature (Operational).

Figure 72 is similar to Figure 71, but has been limited to the specific expected operational temperature range. Again the Y axis to have a much larger range than the other axis, and is still attributed to the connector contact error previously mention. Once it was resolved, the peak-to-peak range of the Y axis seen in Figure 71 and 72 was reduced by nearly 40% to the same range as both the –X and –Z axis sensors, and its standard deviation was reduced to comparable levels as well. The following data reflects this data.

The –X axis sensor saw a decrease in peak-to-peak range of nearly 20%, and a decrease of its standard deviation from 2.7 mV to 2.5 mV, a 7% decrease in standard deviation. The Y axis sensor saw a decrease in peak-to-peak range of nearly 18%, and a decrease of its standard deviation from 2.4 mV to 2.3 mV, a 4% decrease in standard deviation. The –Z axis sensor saw a decrease in peak-to-peak range of nearly 13%, and a decrease of its standard deviation from 2.8 mV to 2.6 mV, a 7% decrease in standard deviation. This shows that by restricting your bias v. temperature data to the expected operational temperature range expected in space, you are able to compute slightly more accurate bias compensation values.

While this is indeed an overall improvement, the improvement is not all that spectacular, and may not justify the use of two separate sets of bias compensation values on the spacecraft. It may be simpler to just keep the single set of bias compensation

values for the entire range of temperatures rather than switching between the two sets if the temperature varies more than expected.

E. QRS11 TEMPERATURE DETERMINATION

On occasion, the spacecraft may want to check on the temperatures of the various subsystems on board. The MEMS sensors output temperature voltage values to the ACS. These values can be used to compute an actual sensor temperature if properly calibrated. From the QRS11 User's Guide, the "nominal voltage" value is defined as the steady state temperature output of each sensor at 25°C. To determine the nominal voltage value for each sensor, the MEMS assembly was placed in the thermal vacuum chamber for twenty-two hours, while the chamber was set to 25°C. The data from this test can be seen below in Figure 73.

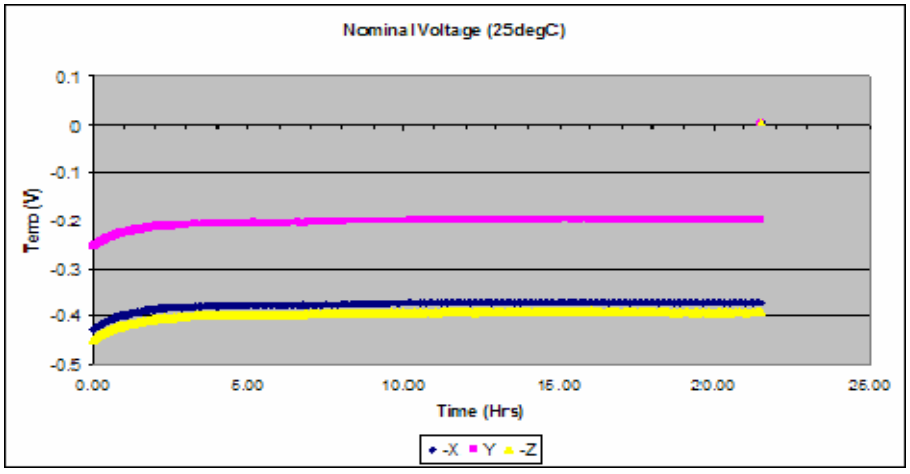

Figure 73. Nominal Voltage Test Results.

The plots for each sensor ramp up from room temperature to their individual values representing 25°C over the first few hours. This output remains fairly consistent over the remaining time of the test. To calculate the nominal voltage for each sensor, the first 5 hours of data from each sensor was thrown out, as well as the last hour. The

remaining sixteen hours of test data was then averaged to calculate the nominal voltage value for each sensor as shown in Table 25.

Sensor	Vn
-X	-0.3724
Y	-0.1995
-Z	-0.3932

Table 25. Nominal Voltage Values.

These values can be saved into the spacecraft onboard computer, and when needed, can be used to calculate the actual temperature of each sensor at any given time using the following equation. $T = 25°C - ((Vn - Tm) / (0.0033 * G))$, where T is the temperature in °C of the sensor, Vn is the nominal voltage value of each sensor, Tm is the measured value of the temperature output in V, and G is the gain of the temperature filter. Gain was calculated for each sensor utilizing the measured PCFB component values recorded in Table 22, where G = R4/R3 + 1, or 120.0 k Ohms / 10.0 k Ohms + 1, yielding a gain of 13.

F. RATE OUTPUT VERIFICATION TESTING

A rate verification test was performed to show that each QRS11 sensor correctly output rates for specific applied rates. The MEMS device was powered up and allowed to warm up for five minutes. The WebDAQ was then programmed to display results every second, and to sample at 200 Hz (200 samples averaged every sec). The Python acquisition program was then set to acquire and display data every 1 second for 50 seconds. The HAAS TRT was then setup according to the setup procedures in Chapter III. It is important to note that while every attempt was made to orient the tilt axis of the HAAS TRT to true west, errors of up to a ±3° were possible. These alignment errors could possibly induce small and fixed voltage outputs errors in the off axis sensors of up to 5% of Earth rate. At Earth rate (2 mV), an error of ±3° in alignment has the potential of inducing (2 mV)sin(3°) = 0.1 mV of error, roughly 5% . This is negligible at high rates, but will need to be addressed at low rates.

1. –Z Axis

Once the controller was zeroed and initialized with tilt and rotation of zero, aligning the TRT locally level and the –X sensor axis pointing east, a series of tests were performed to verify the rate outputs of the each sensor individually. The first axis to be verified was the –Z axis, and required a -36.6° orientation change in the tilt axis of the HAAS TRT. This will place the sense axis of the –Z sensor perpendicular to the East-West rotation of the Earth. The test regiment shown in Table 26 below was used to program each of the ten tests. The tilt, rotation, and rate values were entered and the program was initiated, followed by the Python acquisition program. The WebDAQ results were then averaged over the 50 seconds of the test, and corrected for temperature by subtracting the average rates of each sensor collected before and after each test, then recorded below in Table 26 next to the expected values. This was repeated for all 10 rate tests. The variation in sign of the rotational angle was to keep the sensor wiring harness from over twisting, hence the back and forth rotations.

ΔTilt (°)	ΔRot (°)	Rate (°/s)	-Z Axis (V) Meas/Exp	-Z (σ) mV	-Z (Δ)	Y Axis (mV) Meas/Exp	Y (σ) mV	-X Axis (mV) Meas/Exp	-X (σ) mV
0	250	5.0	2.490 / 2.500	2.4	0.4%	1 / 0	2.9	-2 / 0	2.2
0	-250	5.0	-2.490 / -2.500	2.4	0.4%	0 / 0	2.1	-1 / 0	3.4
0	125	2.5	1.245 / 1.250	2.3	0.4%	2 / 0	2.3	-1 / 0	2.9
0	-125	2.5	-1.245 / -1.250	2.9	0.4%	1 / 0	2.1	2 / 0	2.4
0	50	1.0	0.497 / 0.500	2.0	0.6%	1 / 0	2.7	1 / 0	3.1
0	-50	1.0	-0.499 / -0.500	2.3	0.2%	0 / 0	2.6	0 / 0	2.7
0	25	0.5	0.248 / 0.250	1.8	0.8%	1 / 0	2.1	-3 / 0	2.6
0	-25	0.5	-0.251 / -0.250	1.7	0.4%	0 / 0	2.3	1 / 0	3.0
0	5	0.1	0.049 / 0.050	2.6	2.0%	1 / 0	2.4	-1 / 0	2.7
0	-5	0.1	-0.052 / -0.050	1.9	4.0%	0 / 0	1.9	0 / 0	2.8

Table 26. –Z Axis Sensor Rate Verification Record.

The –Z axis sensor performed as expected, measuring rates very close to those of the programmed input rates for all ten tested rates. An average standard deviation of 2.23 mV was observed in the –Z axis, with a maximum error of 4% seen at the lowest rates, which falls within the potential error due to alignment. Both the –X and Y axis showed

no apparent rate output, with standard deviations in line with what was observed in the -Z axis, verifying that little if any cross coupling is taking place.

2. Y Axis

The next axis to be verified was the Y axis, and required an orientation change to the HAAS TRT in order to align the sense axis of the Y sensor perpendicular to the East-West rotational axis of the Earth. To do this the table was rotated +90°, and the tilt table was tilted -80°, putting the table in the starting position for testing. The test regiment shown below in Table 27 was used to program each of the ten tests. The tilt, rotation, and rate sequence were entered as before, and the program was initiated, followed by the Python acquisition program. The WebDAQ results were then averaged over the 50 seconds of the test, and corrected for temperature by subtracting the average rates of each sensor collected before and after each test, then recorded below in Table 27 next to the expected values. This was repeated for all 10 rate tests.

ΔTilt (°)	ΔRot (°)	Rate (°/s)	Y Axis (V) Meas/Exp	Y (σ) mV	Y (Δ)	-Z Axis (mV) Meas/Exp	-Z (σ) mV	-X Axis (mV) Meas/Exp	-X (σ) mV
160	0	5.0	2.500 / 2.500	2.4	0.0%	5 / 0	1.8	1 / 0	2.3
-160	0	5.0	-2.497 / -2.500	2.7	0.1%	-9 / 0	2.6	16 / 0	3.1
125	0	2.5	1.246 / 1.250	2.8	0.3%	2 / 0	2.5	-9 / 0	2.3
-125	0	2.5	-1.248 / -1.250	2.8	0.2%	-5 / 0	2.0	9 / 0	2.3
50	0	1.0	0.490 / 0.500	2.3	2.0%	0 / 0	2.7	-4 / 0	2.5
-50	0	1.0	-0.502 / -0.500	1.8	0.4%	-2 / 0	2.4	4 / 0	2.3
25	0	0.5	0.250 / 0.250	2.3	0.0%	0 / 0	2.2	-1 / 0	3.5
-25	0	0.5	-0.252 / -0.250	2.5	0.8%	-1 / 0	2.0	1 / 0	2.6
5	0	0.1	0.050 / 0.050	2.6	0.0%	-1 / 0	2.6	1 / 0	2.4
-5	0	0.1	-0.052 / -0.050	2.0	4.0%	0 / 0	2.3	-1 / 0	3.2

Table 27. Y Axis Sensor Rate Verification Record.

The Y axis sensor performed as expected, measuring rates very close to those of the programmed input rates for all ten tested rates. An average standard deviation of 2.42 mV was observed in the Y axis, with a maximum error of 4% seen again at the lowest rates, still falling within the potential error due to alignment. Both the –X and Y axis had standard deviations in line with what was observed in the –Z axis, with some

observed divergence from zero rate in the -X and –Z axis, especially at higher Y axis rates. Calculations show that an alignment error of approximately 0.4° in the orientation between the Y and –x and _Z axis would cause the observed outputs in the -X and –Z axis sensors, and was consistent through all ten tests. This indicates that there is some alignment error, perhaps internal to the sensor itself, as the -3-axis mount appears to be precision machined and the TRT as well.

3. -X Axis

The next axis to be verified was the –X axis, and required an orientation change to the HAAS table in order to align the sense axis of the -X sensor to the axis of rotation. To do this, the table was rotated an additional +90° from the starting point of the last test, leaving the table in the proper starting position for the tests. The test regiment shown below in Table 28 was used to program each of the ten tests. The tilt, rotation, and rate sequence was entered, and the program was initiated, followed by the Python acquisition program. The WebDAQ results were then averaged over the 50 seconds of the test, and corrected for temperature by subtracting the average rates of each sensor collected before and after each test, then recorded below in Table 28 next to the expected values. This was repeated for all 10 rate tests.

ΔTilt (°)	ΔRot (°)	Rate (°/s)	-X Axis (V) Meas/Exp	-X (σ) mV	-X (Δ)	-Z Axis (mV) Meas/Exp	-Z (σ) mV	Y Axis (mV) Meas/Exp	Y (σ) mV
160	0	5.0	2.499 / 2.500	2.6	0.0%	19 / 0	2.9	11 / 0	2.1
-160	0	5.0	-2.504 / -2.500	2.4	0.2%	6 / 0	2.0	11 / 0	2.4
125	0	2.5	1.249 / 1.250	2.2	0.1%	16 / 0	2.3	9 / 0	2.0
-125	0	2.5	-1.246 / -1.250	2.2	0.3%	13 / 0	1.7	5 / 0	2.2
50	0	1.0	0.501 / 0.500	2.4	0.2%	13/ 0	2.2	4 / 0	2.5
-50	0	1.0	-0.499 / -0.500	1.9	0.2%	-15 / 0	2.4	-1 / 0	2.6
25	0	0.5	0.252 / 0.250	2.2	0.8%	7 / 0	2.3	3 / 0	2.2
-25	0	0.5	-0.251 / -0.250	2.1	0.4%	-7 / 0	2.2	0 / 0	2.2
5	0	0.1	0.051 / 0.050	2.6	2.0%	1 / 0	1.9	-2 / 0	1.8
-5	0	0.1	-0.050 / -0.050	3.2	0.0%	-2 / 0	2.7	-1 / 0	2.7

Table 28. -X Axis Sensor Rate Verification Record.

The -X axis sensor performed as expected, measuring rates very close to those of the programmed input rates for all ten tested rates. An average standard deviation of 2.38 mV was observed in the -X axis, with a maximum error of 2% seen again at the lowest rates, still falling within the potential error due to alignment. Again, both off-axis sensors had standard deviations in line with what was observed in the –Z axis, and again showed some observed divergence from zero in both sensors, especially at higher rates. This again pointed to the possibility of unknown alignment errors in the sensor, and warranted further study to determine the root of these errors.

Further investigations into the divergence seen above was conducted to determine whether or not the induced errors in the off-axis sensors were due to alignment errors or other unknown errors. To do this, the MEMS sensor was opened, and all sensors were remounted in their brackets, verifying that they were properly aligned and flush with the mounting surface. The subsystem was then again mounted to the HAAS TRT, and aligned as carefully as possible. At this time, we noticed that the mounting surface was not exactly flat, and was slightly warped outwards, a possible cause to our observed error. Every attempt was made to keep the MEMS base as flush as possible. The WebDAQ again used to capture data as before, and the –Z axis was measured at ±5°/s, these results are seen below.

-Z Axis (V) Meas/Exp	-Z (σ) mV	-Z (Δ)	-X Axis (mV) Meas/Exp	-X (σ) mV	Y Axis (mV) Meas/Exp	Y (σ) mV
2.489 / 2.500	2.7	0.4%	-6 / 0	3.0	-13 / 0	2.5
-2.490 / -2.500	2.4	0.4%	2 / 0	2.5	15 / 0	2.7

Table 29. Alignment Verification Data Test 1.

As you can see, this data differs from what we saw in Table 26 for this axis at these rates. We now see an error in both the –X and Y axes. With mounting alignment verified, this indicates that the observed error may be possibly induced through either the mounting surface of the HAAS TRT, which would explain the varying test results when mounting is altered, or through the internal alignment errors specific to each sensor. Calculating this error from the offset of each axis output and the expected value, we see

that the -X sensor has an offset of 4 mV, which equates to an alignment error of 0.09°. The Y sensor showed an offset of 14 mV, which equates to an alignment error of 0.32°.

To verify that this error was indeed due to alignment, a second test was conducted utilizing a shim of approximately 0.32°. This shim was constructed from paper, and was placed under the left side of the MEMS assembly to re-align the Y axis sensor to negate the observed error in that axis seen in Table 29. With the length of the sensor determined to be approximately 11 cm, the shim thickness was calculated to be 0.06 cm to account for the desired 0.32°. This is extremely difficult to measure accurately, and every attempt was made to construct the shim as close to the required thickness as possible, but some error will be induced here. The results from this test can be seen below.

-Z Axis (V) Meas/Exp	-Z (σ) mV	-Z (Δ)	-X Axis (mV) Meas/Exp	-X (σ) mV	Y Axis (mV) Meas/Exp	Y (σ) mV
2.488 / 2.500	2.3	0.4%	-7 / 0	2.6	-4 / 0	2.5
-2.490 / -2.500	2.4	0.4%	3 / 0	2.9	-1 / 0	2.6

Table 30. Alignment Verification Data Test 2.

As you can see, the shim reduced the rate observed by the Y axis sensor. The alignment error was reduced from 0.32° seen in Table 29 to only 0.07°. Although the shim did not entirely compensate for the observed error due to inaccuracies in the construction of the shim, it indicates that alignment errors are indeed the cause of the off-axes output that we have been seeing. If this is true, the shim should have also induced an error in the –Z axes as well. A shim of 0.25° should induce a rate offset of 0.0003 V in the –Z axis rate output. As you can see from Tables 29 and 30, a decrease in the –Z rate output of 0.0005 V was seen, and suggest that errors are indeed due to alignment.

The fact that these errors vary when the MEMS subsystem is re-mounted when no changes to the internal mounting are made suggests that the alignment errors may be primarily due to the uneven surface of the HAAS TRT, yet it is possible that some of the observed error may still be due to the individual internal alignments of each sensor. To verify this, an absolutely flat mounting surface will be required to isolate the root cause

of the induced errors. It is recommended that these tests be repeated when more precise mounting surfaces and measurement tools are available.

The tests conducted during this test verify that the sensors are accurately measuring rates from tip off, the expected rate of the spacecraft after separation (approximately 5°/s), down to roughly 1.5 times orbital rate (0.1°/s). While some output voltage was observed in the off axis sensors, these errors were most likely induced through surface inaccuracies of the HAAS TRT or internal sensor alignment. Thus, proper alignment of the sensors must be addressed prior to launch to ensure that no unknown errors are unaccounted for during flight operations. With the establishment of the sensors ability to accurately measure rates from tip off down to roughly orbital rate, it was now time to test the performance of the sensor at very low rates.

G. VERY LOW RATE / EARTH RATE TESTS

Similarly to the test conducted above, these tests were developed to verify that each MEMS sensor was correctly outputting rates for specific low rates applied. These rates were extremely small, and attempted to identify the absolute measurement floor possible for the sensors. Utilizing the same experimental setup seen in Section F, the HAAS TRT was zeroed and realigned, returning it to its original starting position of zero tilt and zero rotation. The following two tests were conducted.

1. Low Rate Tests

The first low rate test was similar to the test conducted in the last section. This test was conducted in a single run of the tri-axial sensor, and would step the sensor through a variety of rates ranging from +0.5°/s through -0.5°/s in 24 steps for a single sense axis. The lowest rate tested would be 0.01°/s, roughly 1/7 of orbital rate. To do this the Python acquisition program was set to acquire and display data every one second for four minutes. The HAAS TRT was then turned on and programmed to run a single test, starting at a rotation and tilt of zero and a rotational rate of +0.5°/s, and systematically lowering its rate every 10 seconds, with a 10 second pause between rates, continuing through -0.5°/s. The rate sequence was as follows: +0.5°/s, 0°/s, +0.2°/s, 0°/s

, +0.1°/s, 0°/s, +0.05°/s, 0°/s, +0.02°/s, 0°/s, +0.010°/s, and then on through the respective negatives values. These outputs were overlaid with a reference plot to show when the rates were being applied, as show in Figures 74 through 76.

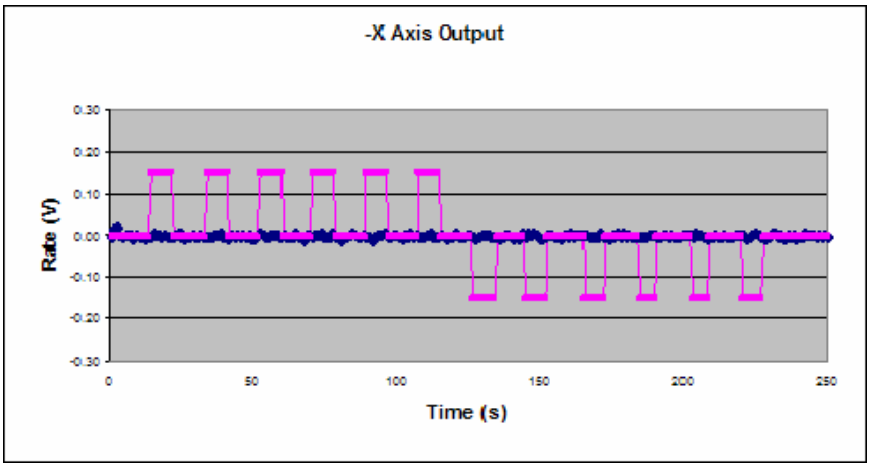

Figure 74. –X Axis (No Rate).

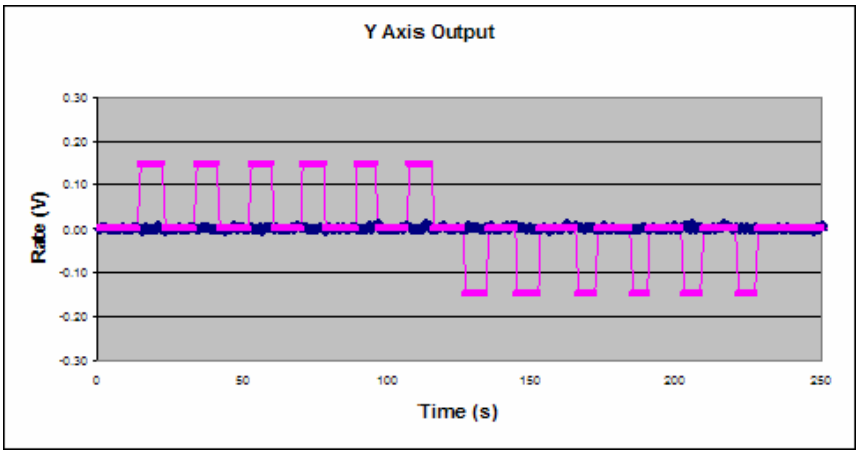

Figure 75. Y Axis (No Rate).

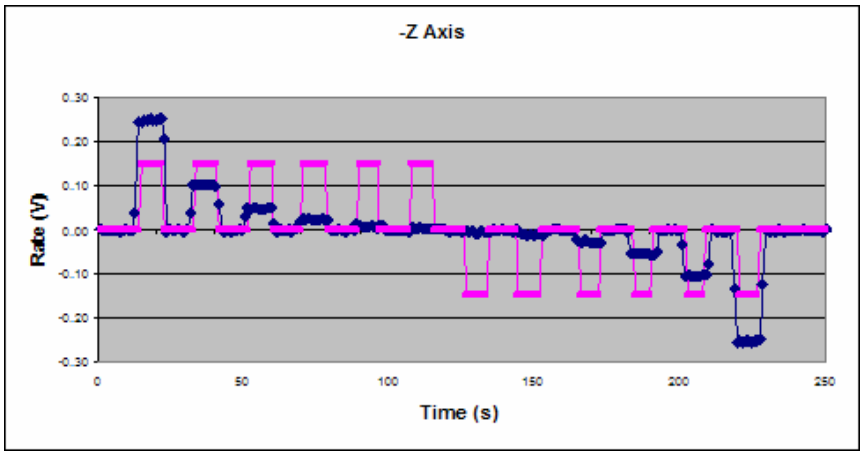

Figure 76. –Z Axis (Observed Rates).

The –X and the Y axes showed no observable variation in outputs during the applied rates, as they should. This is indicative that no cross coupling is taking place, and that the QRS11 sensors are properly aligned and mounted. The average rates were then calculated for the –Z axis during the periods when rates were applied, and can be seen below in Table 31.

Rate (°/s)	-Z Axis Rate (°/s)	σ (mV)	Error mV (Δ)
0.500	0.499	2.2	1 (0.2%)
0.200	0.201	1.3	1 (0.5%)
0.100	0.099	1.4	1 (1.0%)
0.050	0.047	1.3	3 (6.0%)
0.020	0.018	2.3	2 (10.0%)
0.010	0.011	1.7	1 (10.0%)
-0.010	-0.011	2.9	1 (10.0%)
-0.020	-0.020	1.3	0 (0.0%)
-0.050	-0.054	2.5	4 (8.0%)
-0.100	-0.102	0.6	2 (2.0%)
-0.200	-0.206	1.6	6 (3.0%)
-0.500	-0.504	2.3	4 (0.8%)

Table 31. Low Rate test Results.

The sensor performed well even at this much lower rate range, accurately measuring rates as low as 1/7 orbital rate. The error is typically within a standard

deviation and the rate is being obtained under flight-like conditions, where the ACS looks for rate information once a second. The average σ of 1.8 mV corresponds to an uncertainty of approximately 0.004 °/s, close to Earth rate. The maximum σ of 2.9 mV corresponds to an uncertainty of approximately 0.006 °/s. This is about 1/11 of orbital rate and can be considered close to the limit of the resolution without additional work, such as extended averaging and advanced filtering, such as Kalman filtering. A simple test at an extremely low rate would be to try to measure earth rate.

2. Earth Rate Test

The Earth rotates at 0.0042°/s, about 1/16 of orbital rate at LEO. A simple test was designed to measure the earths' rotation. The Agilent scope was used to capture a representative sample of the rate output at 200 samples per second for ninety seconds. The MEMS flight subsystem (Configuration 5), was then mounted to the rotational table of the HAAS TRT, and then it was turned on and programmed to run a single test. The table tilt axis was elevated -36.6° to align the plane of rotation with true north. This test would start with the sensor's sense axis initially pointing west, perpendicular to the Earth's rotation. After 18 seconds, the table would rotate 90° in five seconds, placing the sensor's sense axis south, opposite the rotation of the earth. This was repeated twice more, again putting the sense axis perpendicular and then north. The results from the Agilent scope were then averaged at 200 Hz and compensated for temperature, and can be seen below in Figure 77. The high-rate transition periods were removed for easier interpretation.

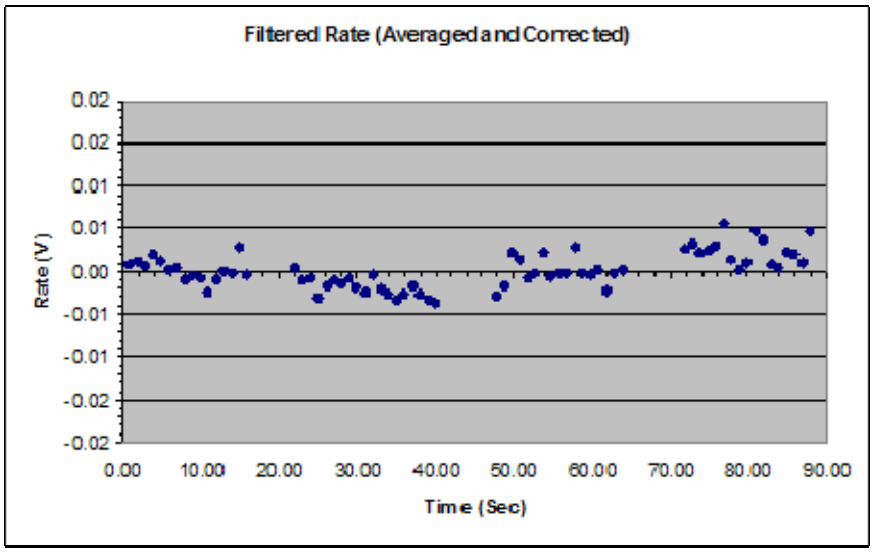

Figure 77. Earth Rate Results (Averaged at 200 Hz).

Notice the clear steps for the four different sense directions. Initially, when the sensor is pointing west, the sensor should see a measured rate of zero volts once temperature has been compensated for. As you can see form the calculations in Table 32, a corrected rate value of 0.0001 V was achieved. The sensors first and third rotation aligned the sensor with the negative and positive axis of the Earths rotation. Here we expected to observe outputs of -2.1 mV and 2.1 mV respectively, and as you can see from Table 32, a 2 mV value was achieved. Thus, the sensor can clearly delineate between rates as low as Earth rate (1/16 orbital rate) at LEO, but requires extended averaging to do it.

Dir	West		South		East		North
Time (s)	18		18		18		18
Rate	0		Neg Earth Rate		0		Pos Earth Rate
Rate (V)	0.0001		-0.0020		-0.0001		0.0023
Rate (°/s)	0.0002		-0.0040		-0.0002		0.0046
Stdev	0.0013		0.0011		0.0016		0.0016
Max	0.0029		0.0003		0.0028		0.0054
Min	-0.0025		-0.0037		-0.0030		0.0000

Table 32. Earth Rate Test Results (Agilent).

Unfortunately, as you can see from Figure 77, at rates this low there is the potential for a high amount of error for any given data point, possibly as high as 150% of Earth rate when measured by the MEMS. This error can be reduced through further averaging, quickly driving the measured rate closer to the true rate. Although averaging over periods of time longer than one second will lead to more accurate rate data at very low rates, it may not be feasible for the ACS to perform accurately under these conditions. Recall from Chapter I that the ACS performs attitude control measurements and control maneuvers every two seconds in an ongoing and continuous cycle. During this cycle the torquers will be activated to correct sensed spacecraft rotation. Unless this control algorithm is able to allow for longer rate determination by the MEMS before using rate information, control maneuvers will be measured by the MEMS, introducing variable rates into any extended averaging process. Clearly, some thought needs to be given to how best to incorporate QRS11 rate data into the ACS control algorithm.

H. SENSOR TO ACS SIMULATION

Now that we have shown that the flight MEMS subsystem is functioning as expected, and performing well above the its original design (Configuration 2), it is only natural to perform a full scale simulation to demonstrate how the ACS will integrate the MEMS data, including all recent re-design implementations, to calculate an accurate output for use. To understand this process a diagram was constructed to illustrate the flow of data from the MEMS to the ACS, and the steps and calculations involved in determining adjusted and useable data. This flow chart can be seen below.

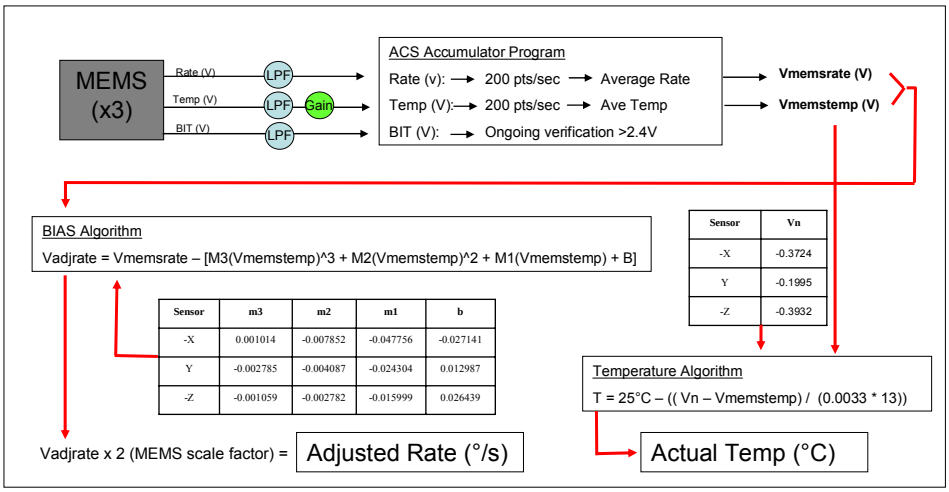

Figure 78. ACS Data Processing Flow Chart.

The purpose of this flow chart is to show how QRS11 data will be received and interpreted by the ACS, and how it will compute its adjusted values using the techniques developed in the research conducted during this thesis. It is not to prove that the MEMS is fully functional, this has already been established. Therefore, this demonstration will simulate only a single output, and will not repeat the same steps for the other 8 outputs of the sensors. For this simulation the Y axis rate output was selected. Using the Agilent scope to capture a representative sample of output rate without averaging or sampling, the following data was obtained from the MEMS subsystem (Configuration 2) at room temperature, with no rate applied.

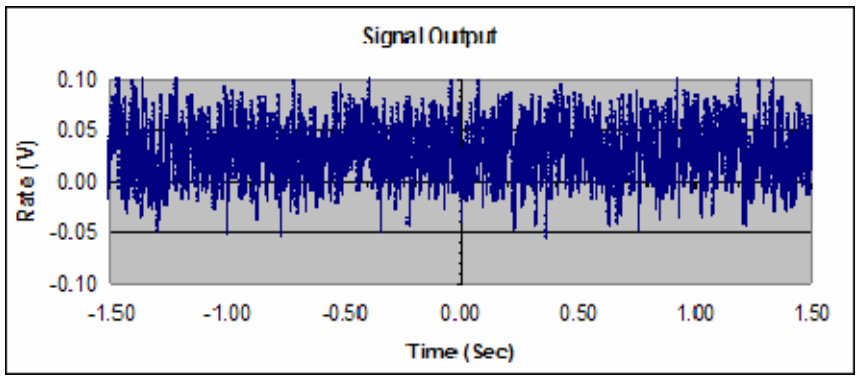

Figure 79. MEMS Signal Output.

This rate signifies the actual measured rate of the QRS11 prior to filtering or temperature compensation. As you can see, the bias of the signal has an average of 29 mV, which is very close to the 30 mV typically seen at room temperature for the Y axis sensor. This data would then pass through the PCFB (Configuration 5) and be filtered as shown below.

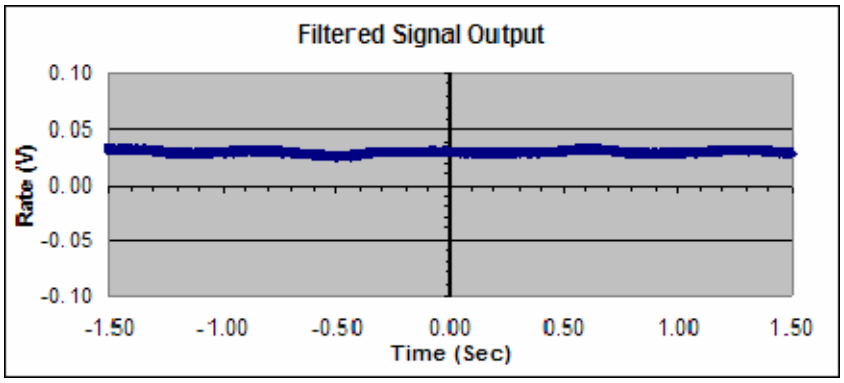

Figure 80. MEMS Filtered Signal Output.

As expected, the bias of the signal maintains its average of 29 mV, while the standard deviation sees a decrease from 24.8 mV to 1.8 mV, and the overall signal peak-to-peak rate output decreases from 160 mV to 11 mV. This data would then be sampled by the ACS at a frequency of 200 Hz, averaging every 200 data points into a single data point for rate. Figure 81 shows the results of this sampling process.

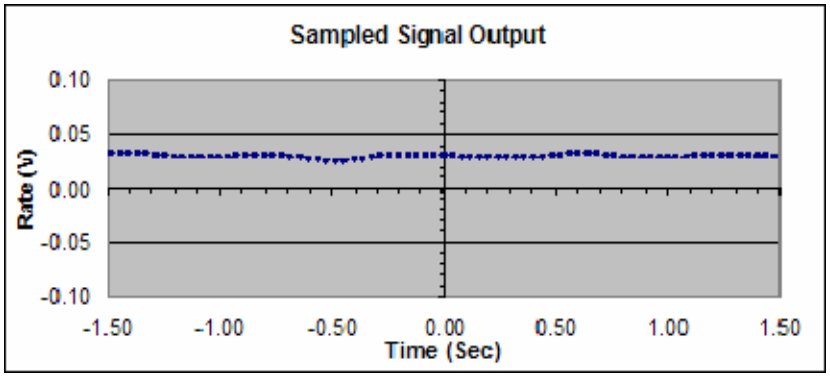

Figure 81. Sampled MEMS Signal Output.

The 200 Hz sampling process attempts to smooth out the filtered data even more. Fortunately, the filtering process does an excellent job minimizing noise. Thus, only marginal improvements were seen from the sampling. While this was the case for this test, it is not indicative of sampling in other application, and therefore, it is not recommended to reduce sampling rates solely due to these results. As expected, the bias of the signal maintains its average of 29 mV, while the standard deviation sees a slight decrease from 1.8 mV to 1.7 mV, and the peak-to-peak range decreases from 11 mV to only 7 mV. From here, the ACS accumulator pushes these data points through the bias compensation algorithm, and in conjunction with the bias compensation values a "corrected" rate voltage is calculated. This voltage was then multiplied by the scaling factor of two, and the "corrected" rate value is obtained. The adjusted rates values are plotted below in Figure 82.

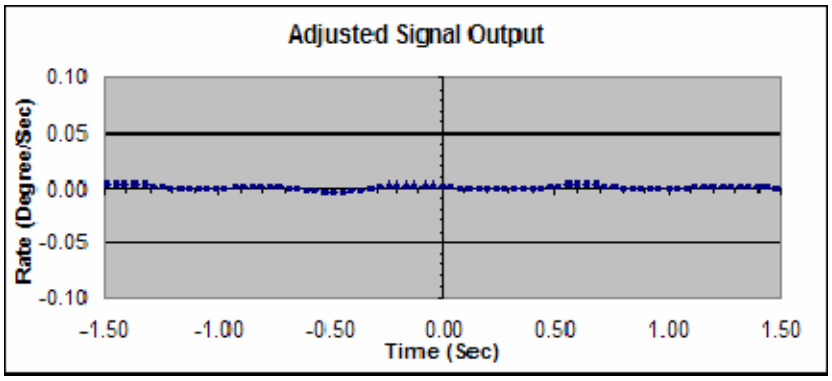

Figure 82. Adjusted Rate Signal Output.

As you can see, the average rate was shifted from the average bias of 29 mV to 0 mV, as it should be when no rate is applied. These points represent the data that the ACS would interpret as rate, and use for attitude control if needed.

I. RESULTS

Through the research conducted for this thesis, significant progress has been made into understanding the operations and capabilities of the QRS11 sensor, as well as how to optimize the sensor to maximize its potential utility to the spacecraft. The optimization techniques were implemented and tested and greatly improved the overall performance of

the test sensor. Testing of the actual flight MEMS subsystem verifies that continued improvement will be difficult and most likely be in the realm of advanced digital filtering.

The purpose of work described in this chapter was to build the actual flight MEMS subsystem, and continue our testing to verify that the improvements we had made to the MEMS subsystem build, PCFBs, and wiring harness would translate from the test sensor to the MEMS flight subsystem. This testing verified that the results from previous chapters are repeatable with the 3-axis configuration of the flight sensors, and that the characteristics learned from that testing remains true for the flight sensors after integration into the flight assembly. As we have seen throughout this chapter, this is indeed the case. The test results yielded data that is directly correlated to data from the test sensor. This yielded a tested, functional flight-like subsystem that is virtually ready for acceptance and qualification testing.

THIS PAGE INTENTIONALLY LEFT BLANK

VII. CONCLUSION AND WAY FORWARD

A. CONCLUSIONS

The original purpose of the MEMS experiment was simple: to gain operational flight experience with MEMS components. To implement this, the MEMS subsystem was to be integrated into the ACS as a low-cost, low-mass, and low-power method of measuring rates to feed to low-cost, 3-axis-stabilization technology demonstration experiment during spaceflight. At the time, there was very little knowledge or understanding of the capabilities of the QRS11 MEMS rate sensors other than what was provided by the manufacturer and the original planners may have not realized the true potential of the sensor. This led to early preconceptions about the capability of the QRS11 rate sensors, which in turn led to inaccurate assumptions. The original planners felt that the MEMS rate sensors would only be useful in the relatively high rate environment of the spacecraft shortly after tip off, estimated to be up to a maximum of 5°/s, and otherwise would be unable to resolve the very low rates associated with stabilized spaceflight at LEO [6, 7].

Through the research conducted for this thesis we now have a solid understanding of the performance characteristics of the sensors. The QRS11 rate sensors have been optimized to accurately measure rates far below what was expected based on the manufacture's specifications. The most important discovery was the relationship between the sensor output bias and temperature. This showed that the level of output bias was directly related to the temperature of the sensor, and that this relationship could be described parametrically. This allowed us to calculate bias compensation values that could be used to accurately correct any given output rate for temperature, removing virtually all bias from any given output rate, across the entire operating temperature range of the sensor. Removing rate bias as one of the two primary sources of rate sensor error allowed us to move on to the reduction of noise.

Significant reduction of noise was made possible by adding Low Pass filters to all three sensor outputs, as well as a gain value to the temperature output. We learned that, in addition to good voltage regulation, the implementation of filtering techniques designed

for our specific output signal, made it possible to greatly reduce the overall peak-to-peak voltage and standard deviation of the noise. These improvements were integrated into the design and build of a new PCFB. After testing, we saw that this PCFB greatly increased the capability and accuracy of the MEMS sensors. In conjunction with the bias compensation parameters, both bias and noise errors have been significantly reduced.

These two facets represent the majority of the improvement in the current flight MEMS build and design. Appendix A and B captures the improvements in procedures to build and test the flight subsystem. The testing conducted throughout this thesis is a testament to the steps needed to verify these improvements, as well as how to reproduce them. While some further optimization may be possible, the improvements presented in this thesis have most likely realized most of what is possible, and that any further optimization may come only through significant cost increases or through areas outside the original scope of this thesis, namely the ACS interface and selection of a different, newer MEMS rate sensor. Other potential sources for future improvements are suggested in the follow-on work section of this chapter.

These rate sensors can easily measure rates at tip-off, and are capable of accurately measuring rates as low as an orbital rate of 0.066°/s for a LEO satellite. Finally, the QRS11 angular rate sensors allow us to sense rates as low as Earth's rotational rate of 0.004°/s. This is a huge shift in the understanding of the sensors, making the overall utility of this sensor far greater than anticipated. These improvements, coupled with the general improvements made to the flight components and build procedures, allowed for a re-design and re-build of the MEMS subsystem that was vastly superior to the original. The current MEMS subsystem is capable of accuracy and resolution thought impossible just 8 months ago, performing well above earlier expectations, and capable of performing accurately at very low rates.

It is important to note here that during the writing of this thesis, after all research was concluded, an article was discovered describing similar testing of a QRS11 sensor for spaceflight. The testing was conducted by Surrey Satellite Technology Ltd for the GIOVE-A spacecraft, and results were published in 2006 [32]. It is important that this work be acknowledged, even though it was not used during the research presented in this

thesis. Though this research is similar, it lacks sufficient detail. However, it does validate many of the conclusions presented here, as well as introducing additional research into bias instability and variance that was not addressed in this thesis. The work was based on the testing of the SDI QRS11 sensor, with High Performance option, standard Noise option, and a rate range of ±50°/s. Their paper also concluded that the QRS11 sensors are capable of achieving better measurement accuracy then specified in the data sheets if properly characterized and understood.

B. FOLLOW ON WORK TO COMPLETION

Through the course of this research there have been some observations noted as being possible follow-on research topics. These will make valuable contributions not only to the NPSAT1 project, but to the small satellite community as a whole. The following work is suggested to take the QRS11 rate subsystem to a completed flight subsystem and perhaps improve the system even further.

1. MEMS Acceptance and Qualification Testing

Though the space qualified MEMS flight subsystem remains to be completed, the bulk of the work has been done. The MEMS subsystem is currently quite flight-like. To finish the construction of the MEMS, first, the flight PCFBs must be assembled, soldered and bonded to the QRS11 sensors. Second, all bolts must be secured using thread tight and appropriate torque values. The "MEMS Test and Build Procedures" in Appendix A contain the necessary steps for both these. Thermal vacuum testing will then be required to verify that the MEMS subsystem is able to survive the temperature environments required for qualification for space flight, as well as that all seals of the MEMS assembly hold, and 1 ATM is maintained. As discussed in Chapter I this qualification temperature range was -29°C to +66°C. Additionally, this would be the time to connect the flight subsystem to the flight ACS to compute the valid bias compensation values for the integrated system as described in Chapter VI. These would be the values actually used by the ACS. Finally, 3-axis vibrational testing and post-vibe inspections will need to be performed. The requirements for these tests are addressed in Chapter II, and can most

likely be done quickly as long as the vibrational table and software are working. Once these tasks are complete, the MEMS flight subsystem will be qualified and ready for integration into the spacecraft.

2. Sampling Re-Testing

With the flight-like configuration complete, it would be a good idea to re-address some of the earlier testing into recommended sampling rates. Earlier in this thesis research it was determined that a sampling rate of the MEMS rate output of 200 Hz by the ACS would meet the needs for resolution and accuracy. Significant modifications to the overall MEMS subsystem have been made since these tests were conducted, and re-testing could possibly prove that even lower sampling rates are possible while maintaining the required accuracy and resolution. This could free up bandwidth and resources of the ACS for other more important tasks.

3. MEMS Stand Alone ACS Experiment

As mentioned in Chapter II, it should be possible to design and integrate an entire ACS subsystem with MEMS components that could have a huge mass and volume savings for possible use in small satellites. The central component of this system could be the Memsense MAG3 3-axis rate, 3-axis magnetometer, and 3-axis accelerometer. We believe that testing methods similar to those done in this thesis could determine if the sensor is capable of meeting the resolution accuracy required for space flight. If so, this research could be expanded to incorporate MEMS sun and star trackers, miniaturized reaction wheels, torquer rods, and electronics to package a stand alone ACS subsystem for use on small satellites

4. PCFB Optimization

Through this research significant improvements to the design of the PCFB were made. There is still room to improve here, namely with the introduction of a microcomputer chip to the PCFB. While we have optimized almost all aspects of filtering and power regulation, we believe that it is still possible to increase the utility of

the MEMS by assuming some of the roles of the ACS internally, and thereby, achieving higher accuracy while freeing up the ACS to perform other tasks. To do this, a microcomputer could be added to the PCFB to perform the duties of the ACS accumulator described in Figure 78, principally analog-to-digital conversion and data averaging. Because it would be free of any other duties, it could do this at much higher sampling rates, and possibly higher bit rates depending on the microcomputer selected. This would serve three functions. First, the data obtained will be much more accurate. Second, the ACS will be freed of the need to continually interface with the MEMS. It can now simply ping the MEMS for current rates. Third, depending on the method by which the data is sent, a significant reduction in the wiring harness mass could be possible. Since the measurements are all taken at the source, and only a value would be transmitted, there would be little potential for inducing digital or analog errors into the signal.

5. Kalman Filtering

The Kalman filter is an efficient recursive filter that estimates the state of a dynamic system from a series of incomplete and noisy measurements, developed by Rudolf Kalman in 1960 [31]. Implementation of a Kalman filter could be used to better estimate low rates while operating the torquers and reaction wheels, which would allow for longer averaging of data, possibly yielding more accurate rates in the very low angular rate environment expected in stable orbit.

6. Orbital Simulation

Simulation of the on-orbit rates and rate coupling profiles of NPSAT1 could be performed to ensure that the rate environment to be experienced by the rate sensors is understood. Research here could provide a better understanding and characterization of the expected low rate environment at stable orbit, as well as to determine if there is any susceptibility to the magnetic torquers. This could be used to re-address some of the earlier research presented in this thesis, potentially yielding higher measurement accuracy, and thus, much more accurate rate measurements.

THIS PAGE INTENTIONALLY LEFT BLANK

LIST OF REFERENCES

[1] D. Sakoda and J.A. Horning, "Overview of the NPS Spacecraft Architecture and Technology Demonstration Satellite, NPSAT1," presented at 16th Annual AIAA/USU Conference on Small Satellites, Logan, UT, 2002.

[2] NASA, "Procedural Requirements, Appendix A: Classification Considerations for NASA Class A-D Payloads," August 2007, http://nodis3.gsfc.nasa.gov/displayDir.cfm?Internal_ID=N_PR_8705_0004_&page_name=main.

[3] J. Horning (private communication), 2007.

[4] D. Sakoda (private communication), 2007.

[5] R. Phelps (private communication), 2007.

[6] B. Leonard, "Simulation Data Package for 20-21 August 2001 NPSAT1 ACS Design Review," Naval Postgraduate School, Monterey, CA, 15 July 2001.

[7] Planetary Systems Corporation Technical Staff, LightBand: An Advanced Separation System for Payload Separation and Staging, Planetary Systems Corporation, July 2003.

[8] E. Okano, "Microelectromechanical Systems for Small Satellite Applications," M.S. thesis, Naval Postgraduate School, Monterey, CA, June 2001.

[9] M. Gruhlke, "Computer Aided Thermal Analysis of a Technology Demonstration Satellite," M.S. thesis, Naval Postgraduate School, Monterey, CA, May 2003.

[10] R.C. Olsen, Introduction to the Space Environment, digital copy provided by author for PH 2514, Naval Postgraduate School, January 2005.

[11] BEI Systron Donner Inertial Division Technical Staff, QRS11: Space Applications, BEI Systron Donner Inertial Division, May 2004.

[12] BEI Systron Donner Inertial Division Technical Staff, "QRS11 Data Sheet (Revision F)," July 2007, http://www.systron.com/PDFS/datasheets/qrs11.pdf.

[13] BEI Systron Donner Inertial Division Technical Staff, "Technology: An Introduction to Quartz Inertial Technology," July 2007, http://www.systron.com/tech.asp.

[14] Sharing Earth Observation Resources, "UoSAT-12," August 2007, http://directory.eoportal.org/pres_UoSAT12.html.

[15] European Space Agency, “Integral,” August 2007, http://sci.esa.int/science-e/www/area/index.cfm?fareaid=21.

[16] European Space Agency, “Smart-1,” July 2007, http://smart.esa.int/science-e/www/area/index.cfm?fareaid=10.

[17] Sharing Earth Observation Resources, “GIOVE: Galileo In-Orbit Validation Element,” July 2007, http://directory.eoportal.org/pres_GIOVEGalileoInOrbit-ValidationElement.html.

[18] European Space Agency, “Plank Surveyor / Herschel Probes,” July 2007, http://sci.esa.int/science-e/www/object/doc.cfm?fobjectid=36465.

[19] BEI Systron Donner Inertial Division Technical Staff, “QRS100 Data Sheet (Revision H),” July 2007, http://www.willburger.de/produkte/neigunggier/datasheets/qrs100.pdf.

[20] MEMSense Technical Staff, “TriRate Triaxial MEMS Gyroscope (Revision F),” July 2007, http://www.memsense.com/downloads/datasheets/TriRate_SMT_Datasheet.pdf.

[21] Silicon Sensing, “CRS03 Angular Rate Sensor,” July 2007, http://www.siliconsensing.com/media/pdf/n/p/CRS03_Datasheet.pdf.

[22] Gladiator Technologies, “G10: Single Axis MEMS Gyro,” July 2007, http://www.gladiatortechnologies.com/DATASHEET/G10_MEMS_GYRO_DATASHEET_072607.pdf.

[23] Honeywell, “MEMS Rotational Rate Sensors: GG1178,” July 2007, http://www.honeywell.com/sites/servlet/com.merx.npoint.servlets.DocumentServlet?docid=D1EB1BDAB-6416-1A5D-5743-159BC78C1CAC.

[24] Melexis Microelectronics Integrated Systems Technical Staff, “MLX90609-N2,” July 2007, http://www.melexis.com/prodfiles/0005013_MLX90609N2_web_datasheet.pdf.

[25] BEI Systron Donner Inertial Division Technical Staff, QRS11 Users Guide (Revision B), BEI Systron Donner Inertial Division, 2005.

[26] J. Newman (private communication with BEI Systron Donner Inertial Sales Representative), 2006.

[27] HAAS Automation INC Technical Staff, Model: TRT7 Tilting Rotary Table User’s Guide, 1990.

[28] Wikipedia, “Butterworth Low Pass Filters,” August 2007, http://en.wikipedia.org/wiki/butterworth_filter.

[29] W. Jung, Analog Devices, Inc, Op Amp Applications Handbook, Newness Publishing, 2005.

[30] L. Wilson (private communication), 2007.

[31] Wikipedia, "Kalman Filters," August 2007, http://en.wikipedia.org/wiki/Kalman_filter.

[32] A. Cropp, C. Collingwood, S. Dussy, Surrey Satellite Technology Ltd, The Characterization and Testing of MEMS Gyros for GIOVE-A, August 2006.

[33] P. J. Overstreet, "Environmental Testing of the Petite Amateur Navy Satellite (PANSAT)," M.S. thesis, Naval Postgraduate School, Monterey, CA, 1997.

[34] D. Beazley, Python: Essential Reference, New Riders Publishing, 2000.

[35] G. Tobey, Burr-Brown Research Corporation, Operational Amplifiers, McGraw Hill Publishing, 1971.

[36] R. Gayakwad, Op-Amps and Linear Integrated Circuits, Prentice Hall Publishing, 2000.

THIS PAGE INTENTIONALLY LEFT BLANK

APPENDICES

Appendix A. MEMS Wiring Harness Build Procedures
Appendix B. MEMS Subsystem Build Procedures
Appendix C. Python Interface Program Code

THIS PAGE INTENTIONALLY LEFT BLANK

APPENDIX A

NAVAL POSTGRADUATE SCHOOL
NPSAT1

NPS Spacecraft Architecture
and
Technology Demonstration Satellite

MEMS Wiring Harness Build Procedures

Document Number: NPS-001-0801

Signature Page:

Original Signed By:

PREPARED BY:_____

Thomas Pugsley Date

PEER REVIEW:_____

David Rigmaiden Date

ENGINEER REVIEW:_____

Dan Sakoda Date

FACULTY APPROVAL:_____

Dr. Rudy Panholzer Date

REVISION LOG

This log identifies those portions of this document, which have been revised since the original issue.

Rev Code	DESCRIPTION	DATE
1.0	Initial Release-Draft	1 Feb. 2007
1.1	Draft Ver. 2	10 Feb. 2007
2.0	Initial Release	15 Feb. 2007
3.0	Updated Release	15 Jun 2007

Table of Contents

List of Tables

List of Figures

Acronyms

MEMS	Micro Electro Machined Systems
ACS	Attitude Control System
SC	Space Craft
SG	Signal Ground
FOD	Foreign Objects or Debris

1 DOCUMENT INFORMATION

1.1 PURPOSE:

This task provides specific instructions on the standard operating procedures for the assembly and testing of the MEMS rate sensor wiring harness (Flight), and preparation for the subsystems future integration into the SC buss. The wiring harness will be responsible for powering the MEMS 3-axis rate sensor and linking it to the ACS.

1.2 SCOPE:

The intention of this document is to develop set procedures for the build and testing of the MEMS 3-axis rate sensor wiring harness (Flight) for integration into the SC. These procedures begin with the availability of all required flight hardware, tools, and test equipment; and end with an assembled, fully operational and tested flight wiring harness, ready for integration into the SC.
This procedure provides steps to prepare, assemble, and test the wiring harness.

1.3 TASK FLOW DIAGRAM:

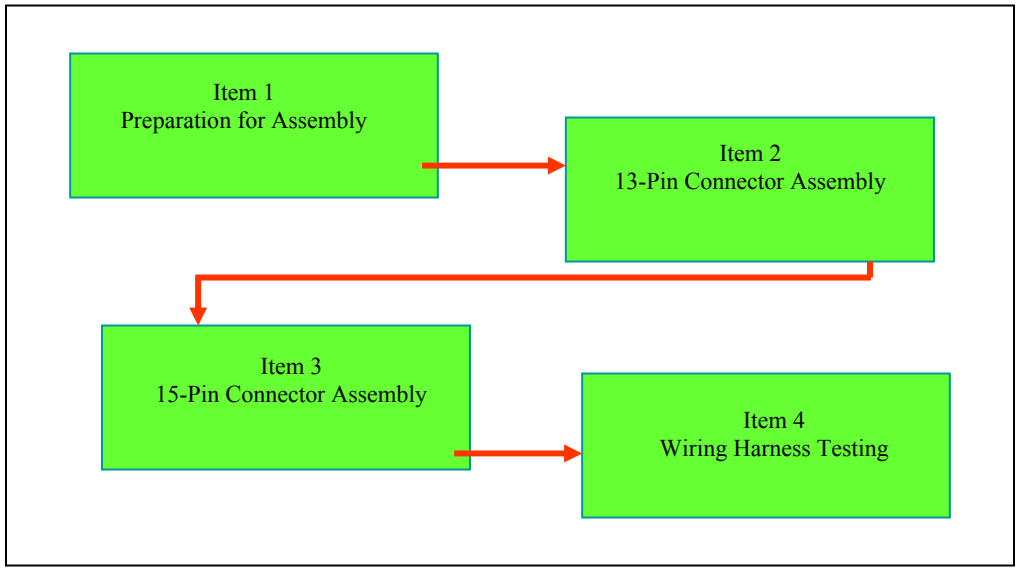

Figure 1: Task Flow Diagram

1.4 OPERATIONAL TIMELINE

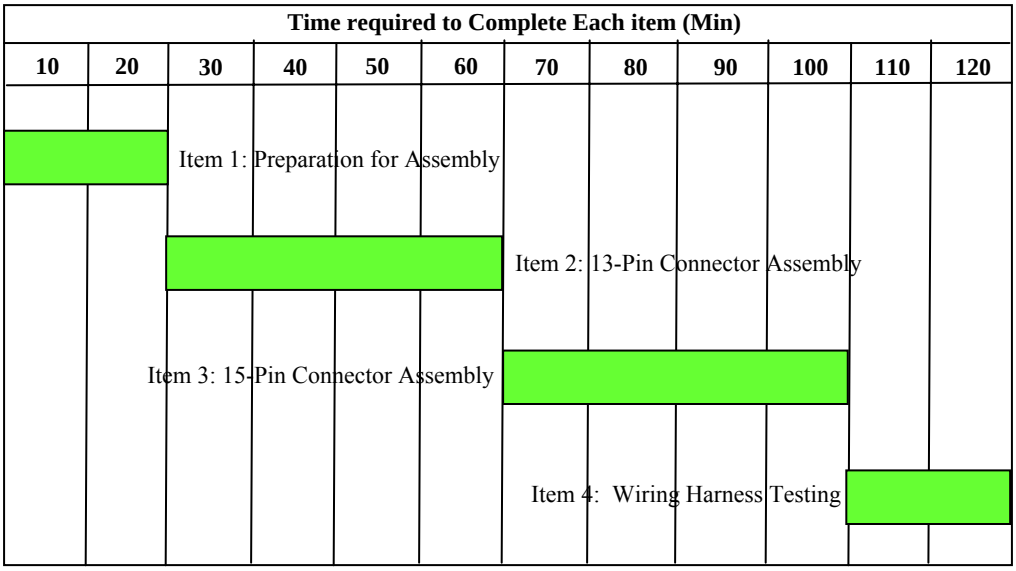

Figure 2: Operational Timeline

2 SAFETY INFORMATION

2.1 HAZARDS AND RISK MITIGATION

RISK MANAGEMENT WORKSHEET

1. Organization and Unit Location:		2. Page	1	of	1
Naval Postgraduate School (NPSAT1 MEMS Wiring Harness Build Procedures)					
3. Mission/Task:	4. Begin Date:	5. End Date:	6. Date Prepared:		
To sucessfully build and test the MEMS flight Wiring Harness for its intigration into the NPSAT1 SC.	TBD	TBD	15 June 07		

7. Operational Phase in which the Mission/Task will be conducted:
Task 1: Instructions (Will be used in all 4 sub-tasks)

8. Tasks	9. Identify Hazards	10. Initial Risk Level	11. Develop Controls	12. Residual Risk Level	13. Implement Controls ("How To")	14. Who/How Supervised
2.2, 3.1	Cut to hands or wires	L	Insure that the tech is working in a well lighted area, and that when not in use the exacto knife is placed away from the work area.	L	E will insure knife is kept clear when not in use. T will handle the tool carefully.	T: Check E: Verify
2.4, 3.3	Burns to hands or wires	L	Insure that the tech is trained on the use of the heat gun, and has the tools to keep his hands clear.	L	T will demonstrate his knowledge of the tool to the E prior to starting.	T: Demonstrate E: Verify
2.7, 3.6	Burns to hands or wires	L	Insure the tech is trained on the use of the thermal strippers, and that they are working properly.	L	T will inspect the strippers, and demonstrate his skill in their use.	T: Demonstrate E: Verify
2.8, 3.7	Bad pin crimps	M	Insure the proper die and depth setting are set for each set of pins, as well as the wires are stripped properly.	L	T will verify that crimper settings are correct, as well as do a test crimp to verify.	T: Test and Insp E: Verify
2.9, 3.8	Incorrect pin location	M	Insure that each pin is inserted into it's correct connector location.	L	T will use the provided diagrams to match tag, with pin, with hole, inserting a pin at a time.	T: Check E: Verify

2.2 PERSONNEL PROTECTIVE EQUIPMENT

Quantity	Part Number	Equipment
2 pair	Com. Item	Protective Gloves (Latex)
2 pair	Com. Item	Protective Splash Goggles

3 SUPPORT REQUIREMENTS

3.1 PERSONNEL REQUIREMENTS

Quantity	Description
1	Technician
1	Engineer Task Leader

4 STAGING REQUIREMENTS

4.1 REQUIRED DOCUMENTS AND DRAWINGS

Document Number	Revision	Description
NPS-0001-0005	Latest	NPSAT1 Wiring Diagram

4.2 REFERENCED DOCUMENTS AND DRAWINGS

Document Number	Revision	Description
MIL-C-38999 Series I-III	Latest	ITT Canon Crimping Instructions
BEI: 964011	B	QRS11 User's Guide

4.3 VEHICLE INSTALLATION PARTS

Quantity	Part Number	Description	Step
28 ft	M27500-24SD2T23	24g Twisted Pair Shielded Wire	2,3
4 ft	MIL-W-16878E	24g Single Wire	2,3
15	Tyco:021174-000	Serving Sleeves	2-3,3-2
1	ITT:KJL6T11N35SN	Cir. 13pin Connector	2-6/9/11
1	GA:440FS030M1003-2B	Cir. 13pin Connector Back Shell	2-12/13
1	AMP:311P409-2P-B-12	Rec. 15pin Connector	3-5/9
1	GA:557-107M2-06CB	Rec. 15pin Connector Back Shell	3-8to11
15	ITT:	Rec. Connector Crimp Pins	3-4/6
13	ITT:031-1147-007	Cir. Connector Crimp Pins	2-5/8/9/11
2	GA: Supplied with BS	Small Braid Banding Rings	2-14,3-7/9
1	Balden:8670-0	4.5ft of ¾" Flat Shielding Braid	2-14,3-9

4.4 GSE AND FACILITY INSTALLATION PARTS

Not Applicable

4.5 CONSUMABLE MATERIALS

Quantity	Part Number	Description	Step
1 Btl	Com. Item	Isopropyl Alcohol	1-1/2/5,3-4
1	Com. Item	Sharpie Permanent Black Marker	2-2,3-1
1 Roll	Com. Item	Capton Tape	2-1,3-8
1 Btl	Com. Item	Canned Air	If Needed

4.6 TOOLS AND TEST EQUIPMENT

Quantity	Part Number	Description	Step
1	Com. Item	Ezacto Knife	2-2,3-1
1	Com. Item	Tape measure	2-2,3-1
1	Com. Item	Diagonal Cut Wire Cutters	If Needed
1	Com. Item	Straight Cut Wire Cutters	If Needed
1	Com. Item	Scissors	3-11
1	PTS-30	Patco Thermal Wire Stripper	2-7/10,3-6
1	Com. Item	Tweezers	2-3,3-2
1	ITT:274-7048-000	Extraction Tool (Geen/White)	2-9
1	AMC:M8196/1-02	Extraction Tool (Red/White)	3-8
1	Com. Item	Needle Nose Pliers	If Needed
1	RMC: 998-306-001	Crimping Die (15 Pin) Setting #5	3-7,4-1
1	ITT:M22520/2-07	Crimping Die (13 Pin) Setting #5	2-8,4-1
1	ITT: M22520/2-01	Crimping Tool	2-8,4-1
1	HB:E-750	Heat Blow Heat Gun	2-4,3-3
1	TD:A30199 SN#17189	TIE-DEX II Banding Tool	2-14,3-11
1	Micro:22-194	Multi-meter (Micronta)	4-2

5 RESPONSIBILITY

5.1 ENGINEER RESPONSIBILITIES

The engineer is responsible to:

a. Be present at all times when work is being performed.

b. Verify or provide the document control working copy of this procedure to the work site.

c. Verify or provide a copy of all required documents and drawings listed in section 4.1 and 4.2 to the work site.

d. Give a briefing at the start of the assembly procedure.

e. Solicit and resolve any questions or problems raised by technician prior to or in parallel with start of work.

f. Walk down the work area and hardware. Verify ready to support.

g. Insure all personnel are wearing listed safety equipment.

h. Observe all work performed and verify that each step was completed correctly when that work is complete.

5.2 TECHNICIAN RESPONSIBILITIES

The technician is responsible to:

a. Review the procedure steps, the required documents, and drawings listed in section 4.1, and the reference documents and drawings listed in section 4.2.

b. Attend the engineer's briefing.

c. Understand the procedure steps prior to the start of work.

d. Identify any anticipated problems, conflicts in the procedure, exceptions to good shop practice, or better ways of performing the tasks.

e. Assist the engineer in resolving problems and improving the process.

f. Perform the tasks as written in the procedure.

6 TASK 1 INSTRUCTIONS

ITEM 1 PREPARATION FOR ASSEMBLY

There are no reference drawings for item 1.

WARNING

The following steps require the use of Isopropyl Alcohol (DPM 0530) that is flammable and a skin and eye irritant. Personnel shall wear (1) PN: DPM8557 Silver Shield Gloves when handling solvents. Wear (1) PN: DPM13169 Goggles when using this material at eye level or above. Use in well ventilated area.

NOTE

Environmental Note: Isopropyl Alcohol (DPM0530) is a Hazardous Chemical. Solid waste such as rags, brushes, swabs, or cleaning pads that come in contact with alcohol and are dry (contain NO FREE LIQUIDS) must be placed in a plastic bag and disposed of in normal trash.

1-1 Technician will clean the assembly table with Isopropyl Alcohol, insuring no FOD is present. He will then visually inspect all tools and test equipment listed in paragraph 4.6 for serviceability, clean them with Isopropyl Alcohol, and put them on the work surface in preparation for assembly.

T _____
Engineer_____

1-2 Technician will inspect the vehicle installation parts listed in paragraph 4.3 to insure they are present, in proper condition, and serviceable. He will clean all parts with Isopropyl Alcohol and place them on the assembly table.

T _____
Engineer_____

ITEM 2 13-PIN CONNECTOR ASSEMBLY

Reference drawings for Item 2 are the NPSAT1 wiring diagram, MEMs connector diagram, and the 13-Pin connector Diagram.

2-1 The technician will cut 7 x 4ft lengths of 24 gauge shielded twisted pair wire from the roll and 1 x 4ft length piece of 24 gauge single wire, and place them on the assembly table. He will tag each of these wires with its purpose with capton tape, 10 inches from one end.

T _____
Engineer_____

2-2 Working on the end opposite form the wire tags, the technician will mark off 5 inches from the end of each twisted pair with a permanent marker. Using an Exacto knife, he will make a perpendicular cut at the mark, around the wire. From this cut, he will then make an incision down the length of the wire to the end. He will then peal back the Teflon outer coating to the mark, cut it off, and trim off any excess coating with horizontal cutters.

T _____
Engineer_____

2-3 The technician will slide the 7 serving sleeves over the exposed wire shielding mesh past the mark. With a pair of tweezers, he will then pull the shielding mesh down to the mark, bunching it up and raising it away from the inner wire. With a pair of wire cutters, he will carefully remove most of the shielding mesh, leaving approximately ¼ inch of the shielding mesh past the mark. He will smooth out the remaining shielding mesh and trim off any excess wire. He will remove the paper wire verification ribbon from the cut off shielding, and verify the proper wire is being used.

T _____
Engineer_____

2-4 The technician will slide the 7 serving sleeves back down over the exposed wire shielding mesh, centering the solder band of the serving sleeve over the exposed shielding. Holding firmly in place, he will heat the serving sleeve with the high temperature air gun, until the solder band drops, and disappears. He will then inspect the serving sleeve, clean off any excess material and remove any FOD.

T _____
Engineer_____

2-5 The technician will visually inspect the 13 circular crimp pins to insure serviceability, and verifying they are the proper pin (Orange Yellow Gray identification bands). He will soak the pins in a small dish of Isopropyl Alcohol, then place on a lint free towel and let air dry.

T _____
Engineer_____

2-6 The technician will lay out the 13-Pin connector, back shell, and a single reference pin on a blank piece of white paper, and draw a diagram of the completed connector as a length reference for building the connector. *Note: Not all serving sleeves will fit into the back shell, thus it will be important to space them out, 3 inside, 4 outside. The 3 inside, closest to the connector, will be the 3 rate and signal ground twisted pairs.*

T _____
Engineer_____

2-7 The technician will bend back the serving sleeve wires for the 3 Rate/SG twisted pairs. He will clip the rate wires approximately 2 inch above the serving sleeve and the SG wires approximately 1 inch above the serving sleeve, centering the serving sleeve in the center of the back shell according to the drawn diagram. With the thermal strippers, he will strip these 6 wires so that the wire is visible through the pin inspection hole, and the Teflon coating is flush with the pin end. He will take the 3 x SG wires, and place them into a serving sleeve. Holding firmly in place, he will heat the serving sleeve with the high temperature air gun, until the solder band drops, and disappears. He will then inspect the serving sleeve, clean off any excess material and remove any FOD. He will then cut this serving sleeve wire to the same length as the 3 rate wires, using the thermal stripers to strip the pin end.

T _____
Engineer_____

2-8 The technician will insure that the proper die is inserted in to the crimping tool (#M22520/2-07), and that the crimp depth switch is set correctly (setting #5). He will then insert a clean pin into the die of the pin crimping tool. He will place the first of the 4 wires into the pin, verify that it is inserted properly and resting flush, and completely compress the crimping tool until hearing the click, then release. He will visually inspect the pin crimp under magnification, insuring a good crimp and proper connectivity. He will repeat these steps for the remaining 3 pins.

T _____
Engineer_____

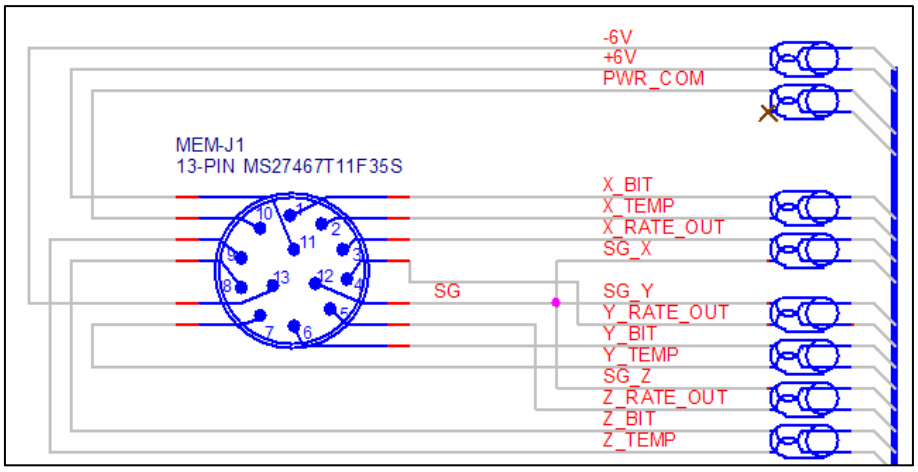

Figure 3: 13-Pin Connector

2-9 The technician will insert these pins with the insertion/extraction tool into the 13-Pin connector, insuring that each tagged wire and pin is inserted correctly to its appropriate location in the connector according to Figure 3. He will inspect both sides of the connector to insure that each pin is seated correctly.

T _____
Engineer_____

2-10 The technician will bend back the serving sleeve wires for the remaining 4 twisted pairs. He will clip the wires approximately 3 inches above the serving sleeve, centering the serving sleeves approximately 1 inch outside of the back shell according to the drawn diagram. With the thermal strippers, he will strip these 9 wires so that the wire is visible through the pin inspection hole, and the Teflon coating is flush with the pin end.

T _____
Engineer_____

2-11 The technician will repeat steps 2-8 and 2-9 for the remaining wires.

T _____
Engineer_____

2-12 The technician will now attach the 13-Pin connector back shell from the opposite side of the wiring harness, securely attaching it to the 13-Pin connector. *Note: He may need to individually feed wires through the back shell to allow the serving sleeves and 7 grounding wires to pass through.*

T _____
Engineer_____

2-13 The technician will bend back all 7 serving sleeve wires back over the banding point of the back shell. He will clip all 7 wires so that approximately 1/4 inch is

overlapping the back shell. Using the thermal strippers, he will strip 1/8 inch off each of these wires. Using a stripped piece of 24 gauge wire as a twist tie, he will secure all 7 of these striped wires to the banding point of the back shell, insuring each is properly grounded. He will then clip off any excess wire.

T _____
Engineer_____

2-14 The technician will slide the shielding braid over the incomplete wiring harness from the open end, insuring to overlap the braid with the back shell banding point and the twisted grounding wires. He will secure the braid with his fingers while sliding a banding band down over the shielding braid to the banding point. Using the banding tool, he will secure the shielding braid to the 13-Pin connector back shell. He will then visually inspect the band, removing any excess material. He will then bunch up the shielding braid as far as possible towards the 13-Pin connector side, and secure with a simple low pressure clamp.

T _____
Engineer_____

ITEM 3 15-PIN CONNECTOR ASSEMBLY

Reference drawings for Item 3 are the NPSAT1 wiring diagram, MEMs connector diagram, 13-Pin connector Diagram, 15-Pin connector diagram, and the ACS wiring diagram.

3-1 The technician will start by clipping and evening out the wires of the exposed 15-Pin connector side. He will then mark off 2" from the end of the 3 rate/SG twisted pairs, and 3" from the other 4 twisted pairs and single wire with a permanent marker. Using an Exacto knife, he will make a perpendicular cut at the mark, and around the twisted pair. From this cut, he will then make an incision down the length of the wire to the end. He will then peal back the Teflon outer coating to the mark, cut it off, and trim off any excess coating with horizontal cutters.

T _____
Engineer_____

3-2 The technician will slide the 7 serving sleeves over the exposed wire shielding mesh past the mark. With a pair of tweezers, he will then pull the shielding mesh down to the mark, bunching it up and raising it away from the inner wire. With a pair of wire cutters, he will carefully remove most of the shielding mesh, leaving approximately ¼" of the shielding mesh past the mark. He will smooth out the remaining shielding mesh and trim off any excess wire. He will remove the paper wire verification ribbon from the cut off shielding, and verify the proper wire is being used.

T _____
Engineer_____

3-3 The technician will slide the 7 serving sleeves back down over the exposed wire shielding mesh, centering the solder band of the serving sleeve over the exposed shielding. Holding firmly in place, he will heat each of the serving sleeves with the high temperature air gun, until the solder band drops, and disappears. He will then inspect the serving sleeves, clean off any excess material and remove any FOD.

T _____
Engineer_____

3-4 The technician will visually inspect the 15 rectangular crimp pins to insure serviceability, and verifying they are the proper pin. He will soak the pins in a small dish of Isopropyl Alcohol, then place on a lint free towel and let air dry.

T _____
Engineer_____

3-5 The technician will lay out the 15-Pin connector, back shell, and a single reference pin on a blank piece of white paper, and draw a diagram of the

completed connector as a length reference for building the connector. *Note: Not all serving sleeves will fit into the back shell, thus it will be important to space them out, 3 inside, 4 outside. The 3 inside, closest to the connector, will be the 3 rate and signal ground twisted pairs.*

T _____
Engineer_____

3-6 The technician will bend back the serving sleeve wires for all 7 of the twisted pairs to get them out of the way. With the thermal strippers, he will strip the 15 wires so that the wire is visible through the pin inspection hole, and the Teflon coating is flush with the pin end.

T _____
Engineer_____

3-7 The technician will insure that the proper die is inserted in to the crimping tool (# 998-306-001), and that the crimp depth switch is set correctly (setting #5). He will then insert a clean pin into the die of the pin crimping tool. He will place the first of the 15 wires into the pin, verify that it is inserted properly and resting flush, and completely compress the crimping tool until hearing the click, then release. He will visually inspect the pin crimp under magnification, insuring a good crimp and proper connectivity. He will repeat these steps for the remaining 14 pins.

T _____
Engineer_____

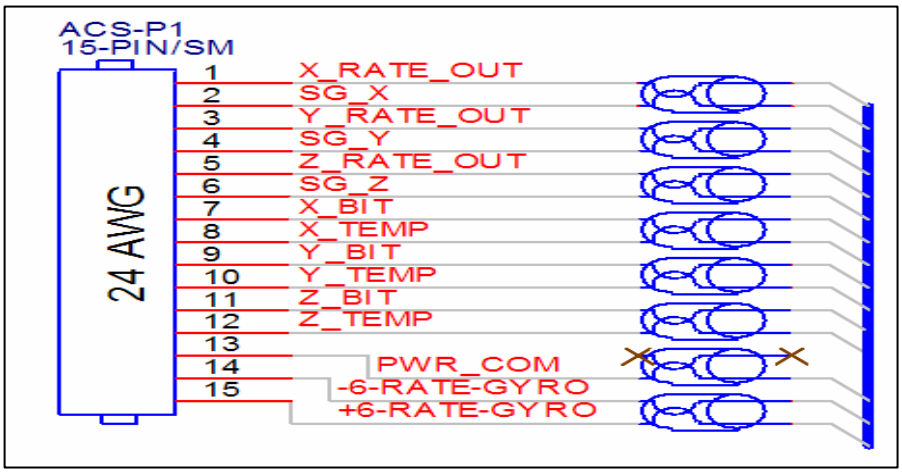

Figure 4: 15-Pin Connector

3-8 The technician will slide the banding band and the back shell over the pins down to the middle of the wiring harness. He will then carefully insert the 15 pins with the insertion/extraction tool into the 15-Pin connector, insuring that each tagged

wire and pin is inserted correctly to its appropriate location in the connector according to Figure 3. He will inspect both sides of the connector to insure that each pin is seated correctly. He will then remove the wire tags.

T _____
Engineer_____

3-9 The technician will now attach the 15-Pin connector back shell from the middle of the wiring harness, securely attaching it to the 15-Pin connector. *Note: He may need to individually feed some of the serving sleeves wires through in order for the back shell to pass*.

T _____
Engineer_____

3-10 The technician will bend back all 7 serving sleeve wires back over the banding point of the back shell. He will clip all 7 wires so that approximately 1/4 inch is overlapping the back shell. Using the thermal strippers, he will strip 1/8 inch off each of these wires. Using a stripped piece of 24 gauge wire as a twist tie, he will secure all 7 of these striped wires to the banding point of the back shell, insuring each is properly grounded. He will then clip off any excess wire.

T _____
Engineer_____

3-11 The technician will remove the clamp, and slide the shielding braid up and over the 15-Pin connector banding point. He will stretch and constrict the braid as much as possible, insuring a tight shielding braid fit over the wiring harness as well as a good overlap of the braid with the back shell banding point and the twisted grounding wires. He will then remove any excess shielding braid with scissors. Once the braid is properly fitted, he will secure the braid with his fingers while sliding the banding band down over the shielding braid to the banding point. Using the banding tool, he will secure the shielding braid to the 15-Pin connector back shell. He will then visually inspect the band, removing any excess material.

T _____
Engineer_____

ITEM 4 WIRING HARNESS TESTING

Reference drawings for Item 3 are the NPSAT1 ACS wiring diagram, MEMs connector diagram, 13-Pin connector Diagram, and 15-Pin connector diagram.

4-1 The technician will place the completed wiring harness on an electrostatic work surface. He will take two 6" long pieces of 24 gauge wire, and thermally strip off 1/8" off of each end. He will crimp a male pin to one of these wires and a female pin to the other wire.

T _____
Engineer_____

4-2 The technician will take a calibrated multi-meter, and attach one wire to each probe. He will set up the multi-meter to auto, and turn on the audio alarm. He will place the female test pin onto the respective male pin of the 15-Pin connector as seen in the table below. With the male test pin, he will cycle through all of the female pin holes of the 13-Pin connector including braid and case ground, and note when the alarm sounds.

Connector Pin # (15-Pin)	Alarm Pin # (13-Pin)	Correct Pin # (13-Pin)	Pass (Y/N)
1		3	
2		12	
3		4	
4		12	
5		5	
6		12	
7		1	
8		2	
9		6	
10		7	
11		8	
12		9	
13		10	
14		13	
15		11	

Table 1: Wiring Harness Test Record

T _____
Engineer_____

7 TASK COMPLETION REVIEW

7.1 ENGINEER REVIEW OF PROCEDURE TASK COMPLETION

The signature below indicates that the undersigned engineer has reviewed the completed work copy of this procedure, and the hardware affected, and is satisfied that the work is correct and complete.

Engineer Signature Date

Engineer Printed Name

7.2 DOCUMENT CONTROL REVIEW OF PROCEDURE COMPLETION

The signature below indicates that the undersigned document control representative has reviewed the completed work copy of this procedure, is satisfied that the document is complete, and will store this document in the document control center.

Document Control Representative Date

Document Control Representative Printed Name

APPENDIX B

NAVAL POSTGRADUATE SCHOOL
NPSAT1

NPS Spacecraft Architecture
and
Technology Demonstration Satellite

MEMS Test and Build Procedures

Document Number: NPS-001-0802

Signature Page:

Original Signed By:

PREPARED BY:_____

Thomas Pugsley Date

PEER REVIEW:_____

David Rigmaiden Date

ENGINEER REVIEW:_____

Dan Sakoda Date

FACULTY APPROVAL:_____

Dr. Rudy Panholzer Date

REVISION LOG

This log identifies those portions of this document, which have been revised since the original issue.

Rev Code	DESCRIPTION	DATE
1.0	Initial Release-Draft	15 Jun 2007
2.0	Initial Release	15 Jul 2007

Table of Contents

List of Tables

List of Figures

Acronyms

MEMS	Micro Electro Machined Systems
ACS	Attitude Control System
SC	Space Craft
SG	Signal Ground
FOD	Foreign Objects or Debris
PCB	Power Control Board (Power/Noise Filter and Amplifier)

1 DOCUMENT INFORMATION

1.1 PURPOSE:

This task provides specific instructions on the standard operating procedures for the assembly and testing of the MEMS 3-Axis rate sensor subsystem (Flight), and preparation for the subsystems future integration into the SC buss. The MEMS 3-axis rate sensor will be responsible for providing the ACS with essential temperature and rate data necessary for maintaining a high degree of point accuracy for the SC.

1.2 SCOPE:

The intention of this document is to develop set procedures for the build and testing of the MEMS 3-axis rate sensor (Flight) for integration into the SC. These procedures begin with the availability of all required flight hardware, tools, and test equipment; and end with an assembled, fully operational and tested flight subsystem, ready for integration into the SC.
This procedure provides steps to prepare, assemble, and test the MEMS 3-axis rate sensor subsystem.

1.3 TASK FLOW DIAGRAM:

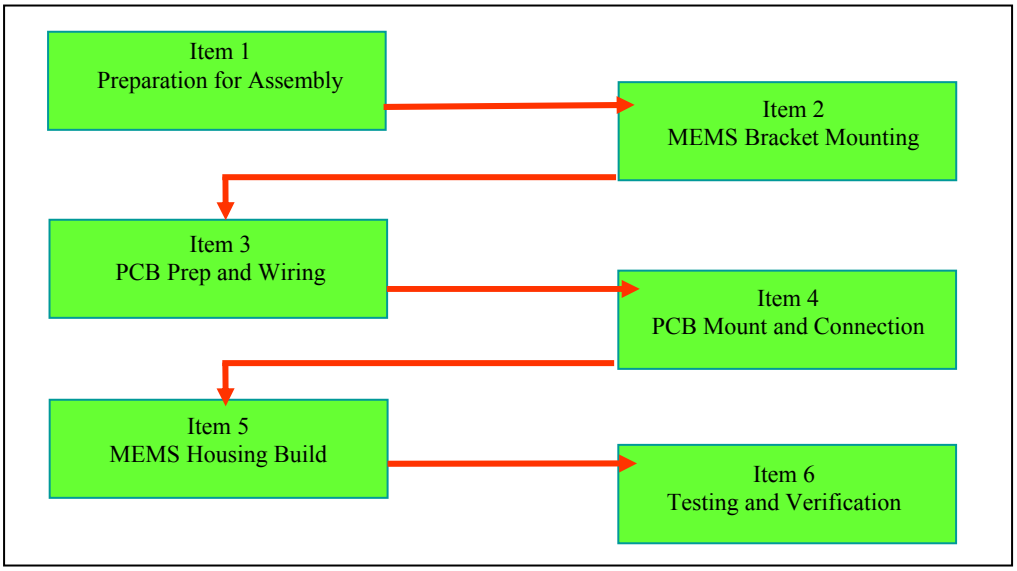

Figure 1: Task Flow Diagram

1.4 OPERATIONAL TIMELINE

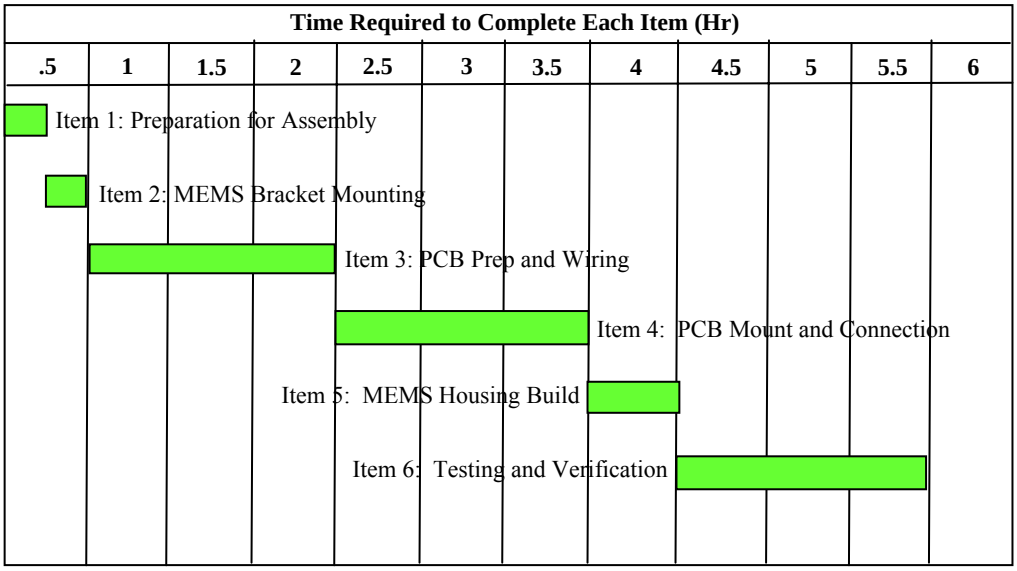

Figure 2: Operational Timeline

2 SAFETY INFORMATION

2.1 HAZARDS AND RISK MITIGATION

RISK MANAGEMENT WORKSHEET

1. Organization and Unit Location:		2. Page	1	of	1
Naval Postgraduate School (NPSAT1 MEMS Wiring Harness Build Procedures)					
3. Mission/Task:	**4. Begin Date:**	**5. End Date:**	**6. Date Prepared:**		
To sucessfully build and test the MEMS flight Wiring Harness for its intigration into the NPSAT1 SC.	TBD	TBD	15 June 07		

7. Operational Phase in which the Mission/Task will be conducted:
Task 1: Instructions (Will be used in all 4 sub-tasks)

8. Tasks	9. Identify Hazards	10. Initial Risk Level	11. Develop Controls	12. Residual Risk Level	13. Implement Controls ("How To")	14. Who/How Supervised
2.2, 3.1	Cut to hands or wires	L	Insure that the tech is working in a well lighted area, and that when not in use the exacto knife is placed away from the work area.	L	E will insure knife is kept clear when not in use. T will handle the tool carefully.	T: Check E: Verify
2.4, 3.3	Burns to hands or wires	L	Insure that the tech is trained on the use of the heat gun, and has the tools to keep his hands clear.	L	T will demonstrate his knowledge of the tool to the E prior to starting.	T: Demonstrate E: Verify
2.7, 3.6	Burns to hands or wires	L	Insure the tech is trained on the use of the thermal strippers, and that they are working properly.	L	T will inspect the strippers, and demonstrate his skill in their use.	T: Demonstrate E: Verify
2.8, 3.7	Bad pin crimps	M	Insure the proper die and depth setting are set for each set of pins, as well as the wires are stripped properly.	L	T will verify that crimper settings are correct, as well as do a test crimp to verify.	T: Test and Insp E: Verify
2.9, 3.8	Incorrect pin location	M	Insure that each pin is inserted into it's correct connector location.	L	T will use the provided diagrams to match tag, with pin, with hole, inserting a pin at a time.	T: Check E: Verify

2.2 PERSONNEL PROTECTIVE EQUIPMENT

Quantity	Part Number	Equipment
2 pair	Com. Item	Protective Gloves (Latex)
2 pair	Com. Item	Protective Splash Goggles

3 SUPPORT REQUIREMENTS

3.1 PERSONNEL REQUIREMENTS

Quantity	Description
1	Technician
1	Engineer Task Leader

4 STAGING REQUIREMENTS

4.1 REQUIRED DOCUMENTS AND DRAWINGS

Document Number	Revision	Description
NPS-QRS11-Ver3	Latest	MEMS PCB Schematic / Diagram
QRS-11 Board Build	Original	PCB Build Document
NPS-0001-0005	Latest	NPSAT1 Wiring Diagram

4.2 REFERENCED DOCUMENTS AND DRAWINGS

Document Number	Revision	Description
Glenair: 230-001	2004	Hermetic Circular Connector Diagram
BEI: 964011	B	QRS11 User's Guide

4.3 VEHICLE INSTALLATION PARTS

Quantity	Part Number	Description	Step
1	NPS-0311	MEMS Housing Base Plate	2(2)
1	NPS-0312	MEMS Housing	5(1)
1	Locally Purchased	MEMS Housing O Ring	5(1)
2	McMaster: 4464K559	MEMS Purge Plugs (1/16" Hex)	5(3)
1	BEI: 260550	MEMS Tri-Axis Mount Bracket	2(1)
1	GA: 230-001-P11-35P	13-Pin Hermetic Connector	4(6) 5(1,2)
1	Locally Produced	0.0255" Connector Shim	5(2)
10	24181	Housing Screws (#4-40 by 3/8" Hex)	5(1)
10	24181	Housing Screw Washers	5(1)
3	23157	Bracket Screws (#4-40 by ½" Hex)	2(2)
3	23157	Bracket Screw Washers	2(2)
12	22897	Sensor Screws (#2-56 by ¼" Hex)	2(1)
12	22897	Sensor Screw Washers	2(1)
3	BEI: 260550	MEMS Sensor C Clamp	2(1)
3	BEI: QRS 11	MEMS Rate Sensors	2(1)
3	Locally Produced	PCB Spacers	3(8)

3	Locally Produced	MEMS PC/Filter Board	3 (all)
4ft	AWC: 007642-AW	24 Gauge Wire (White and Red)	3(2)

4.4 GSE AND FACILITY INSTALLATION PARTS

Not Applicable

4.5 CONSUMABLE MATERIALS

Quantity	Part Number	Description	Step
1 Btl	Com. Item	Isopropyl Alcohol	1(1,2)
1 Roll	Com. Item	Capton Tape	3(7,8)
1 Roll	Com. Item	Teflon Tape	5(3)
1 Btl	Nusil	RTV	4(1,3)
1	Com. Item	Razor Blade / Exacto Knife	3(8,9)
1 Btl	Nusil: 01152CV	Conformal Coating (CV-1152)	3(7,8)
3	Com. Item	Acid Brush	3(7,8) 4(1)
1	Com. Item	Permanent Marker	3(1)
6 cuFt	Com. Item	Nitrogen	5(3)
1 Btl	Com. Item	Thread Tight (Locktite 222)	2(1,2) 5(1,2)
1	XYtronic: 168-3C	Solder Gun	3(all) 4(all)
1 Roll	Com. Item	Solder	3(all) 4(all)
1 Btl	Com. Item	Canned Air	1(1)

4.6 TOOLS AND TEST EQUIPMENT

Quantity	Part Number	Description	Step
1	Com. Item	Ruler	3(2)
1	Com. Item	Diagonal Cut Wire Cutters	As needed
1	Locally Produced	Nitrogen Purge Kit	5(3)
1	Com. Item	Straight Cut Wire Cutters	3(2)
1	PTS-30	Patco Thermal Wire Stripper	3(2)
1	Com. Item	Tweezers	When needed
1	Com. Item	Needle Nose Pliers	When needed
1		Torque Wrench	2(1,2) 5(1,2)
1	Com. Item	Philips Head Socket (#2-56)	2(1)
1	Com. Item	Hex Sockets (#4-40)	2(2) 5(1)
1	Com. Item	Allen Wrench (1/16”)	When needed
2	Com. Item	Wire Clamp	3(2)
1	Com. Item	Table Clamp	3(3,4,5) 4(6)
1	Com. Item	File	3(7)
1	Com. Item	Magnifying Glass	3(1) 4(2,3)
1	Cec: 05600-60100A	WebDAQ (SN# 100A001940004A2)	6(all)
1	Infinium 54832B DSU	Agilent Scope (SN# 5641000916)	6(4,5)
1	HP: E3630A	Power Supply (SN# KR34702193)	3(1,6) 6(all)

1	SN# 0125	HAAS 2-Axis Rotational Table	6(all)
1	Micro:22-194	Multi-meter (Micronta)	3(1,6) 4(10) 6(all)

5 RESPONSIBILITY

5.1 ENGINEER RESPONSIBILITIES

The engineer is responsible to:

i. Be present at all times when work is being performed.

j. Verify or provide the document control working copy of this procedure to the work site.

k. Verify or provide a copy of all required documents and drawings listed in section 4.1 and 4.2 to the work site.

l. Give a briefing at the start of the assembly procedure.

m. Solicit and resolve any questions or problems raised by technician prior to or in parallel with start of work.

n. Walk down the work area and hardware. Verify ready to support.

o. Insure all personnel are wearing listed safety equipment.

p. Observe all work performed and verify that each step was completed correctly when that work is complete.

5.2 TECHNICIAN RESPONSIBILITIES

The technician is responsible to:

g. Review the procedure steps, the required documents, and drawings listed in section 4.1, and the reference documents and drawings listed in section 4.2.

h. Attend the engineer's briefing.

i. Understand the procedure steps prior to the start of work.

j. Identify any anticipated problems, conflicts in the procedure, exceptions to good shop practice, or better ways of performing the tasks.

k. Assist the engineer in resolving problems and improving the process.

l. Perform the tasks as written in the procedure.

6 TASK 1 INSTRUCTIONS

ITEM 1 PREPARATION FOR ASSEMBLY

There are no reference drawings for item 1.

WARNING

The following steps require the use of Isopropyl Alcohol (DPM 0530) that is flammable and a skin and eye irritant. Personnel shall wear (1) PN: DPM8557 Silver Shield Gloves when handling solvents. Wear (1) PN: DPM13169 Goggles when using this material at eye level or above. Use in well ventilated area.

NOTE

Environmental Note: Isopropyl Alcohol (DPM0530) is a Hazardous Chemical. Solid waste such as rags, brushes, swabs, or cleaning pads that come in contact with alcohol and are dry (contain NO FREE LIQUIDS) must be placed in a plastic bag and disposed of in normal trash.

1-1 Technician will clean the assembly table with Isopropyl Alcohol, insuring no FOD is present. He will then visually inspect all tools and test equipment listed in paragraph 4.6 for serviceability, clean them with Isopropyl Alcohol, and put them on the work surface in preparation for assembly. He will then insure that the Electrostatic Work Matt is properly grounded.

T _____
Engineer_____

1-2 Technician will inspect the vehicle installation parts listed in paragraph 4.3 to insure they are present, in proper condition, and serviceable. He will clean all parts with Isopropyl Alcohol and place them on the grounded assembly table.

T _____
Engineer_____

ITEM 2 MEMS BRACKET MOUNTING

Reference drawings for Item 2 are the BEI QRS-11 diagram, MEMS Housing Base Plate Schematic, and the BEI QRS-11 Tri-Axis Mounting Bracket Diagram.

2-1 The technician will take the tri-axis mounting bracket, and place it on the work matt with the Y face up. He will take the first QRS-11 and carefully place it into its socket. He will now apply a small band of thread tight to the lower threads of the 4 sensor screws. He will then place the mounting C clamp over the MEMS, insert and loosely thread the 4 sensor screws and washers until almost flush. With his free hand, he will hold the sensors flat edge flush with the flat edge of the socket. With a torque wrench, he will then alternately tighten each screw to a torque value of 1.4 in-lbs. He will then record the SN# of the QRS-11 on the Y face SN# line below. The technician will then repeat these steps for the –X and –Z faces.

-X Face SN#: _____
Y Face SN#: _____
-Z Face SN#: _____

T _____
Engineer_____

2-2 The technician will begin by placing a small band of thread tight onto the lower threads of the 3 bracket screws. He will then place the housing base plate on the work table. He will place the tri-axis mount in its position on top of the base plate. *Note: The tri-axis mounting bracket will only mount in a single orientation.* He will then insert and loosely thread the 3 bracket screws and washers through the tri-axis mounting bracket into the housing base plate until almost flush. With his free hand, he will hold the brackets flat edges flush with the base plate raised alignment surface. With a torque wrench he will tighten each screw to a torque value of 1.4 in-lbs.

T _____
Engineer_____

ITEM 3 PCB PREP AND WIRING

Reference drawings for Item 3 are the QRS11 PCB Schematic, the QRS11 PCB Diagram, the MEMS Wiring Diagram, and the QRS-11 Users Guide.

3-1 Using a magnifying glass, the technician will visually inspect each of the 3 PCB boards for proper build with reference to the QRS11 PCB Schematic. With a calibrated multi-meter and power supply, he will perform a quick verification sequence. First, he will verify that the PCBs are properly stepping down the voltage from +/- 6V to +/- 5V, by testing Pins 5 (+5V) and Pin 6 (-5V). He will then GND each Rate, Temp, and BIT Pin, and verify that the output lead output goes to zero for each. He will then take a small permanent marker and mark each of the 3 PCB boards with a –X, Y, and –Z, just below the QRS11 stamp

T _____

Engineer_____

3-2 The technician will now take the roll of 24 gauge flight wire, and using a pair of wire cutters, he will cut twenty one 5" lengths of wire. Using the thermal strippers, he will strip 1/16" off one end of each of the wires, and 1/8" off the other end.

T _____

Engineer_____

3-3 The technician will now take the -X PCB, and mount it into a desk clamp and place it on the work table in front of him. He will insure that the soldering gun is ready, properly set to 700˚F, and that the solder, damp sponge, and lengths of wire are easily reachable. The technician will take a piece of wire, and carefully insert it into the center most +6 VDC hole as seen in the figure below. With the soldering gun and solder, he will solder the wire into place, then visually inspect it for a clean and strong solder. He will repeat this step for the remaining 6 lengths of wire as follows: two wires into the center most GND holes; a wire into the center most -6 VDC hole; and the remaining 3 lengths of wire will be inserted and soldered as before into the BIT, RATE, and TEMP holes. The technician and engineer will each do a final visual inspection of the PCB soldering to insure everything is done to standard, and then set the PCB to the side.

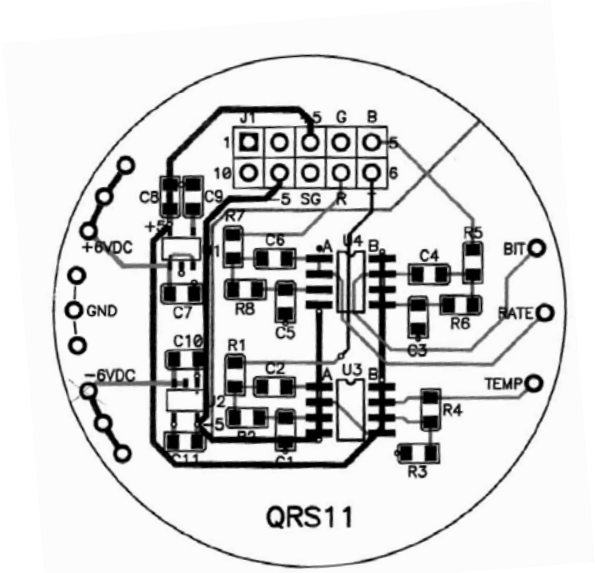

Figure 3: PCB Diagram

T _____
Engineer_____

3-4 The technician will now take the Y PCB, and mount it into a desk clamp and place it on the work table in front of him. He will insure that the soldering gun is ready, properly set to 700˚F, and that the solder, damp sponge, and lengths of wire are easily reachable. The technician will take a piece of wire, and carefully insert it into the center most +6 VDC hole. With the soldering gun and solder, he will solder the wire into place, then visually inspect it for a clean and strong solder. He will repeat this step for the remaining 6 lengths of wire as follows: two wires into the center most GND holes; a wire into the center most -6 VDC hole; and the remaining 3 lengths of wire will be inserted and soldered as before into the BIT, RATE, and TEMP holes. The technician and engineer will each do a final visual inspection of the PCB soldering to insure everything is done to standard, and then set the PCB to the side.

T _____
Engineer_____

3-5 The technician will now take the -Z PCB, and mount it into a desk clamp and place it on the work table in front of him. He will insure that the soldering gun is ready, properly set to 700˚F, and that the solder, damp sponge, and lengths of wire are easily reachable. The technician will take a piece of wire, and carefully insert it into the center most +6 VDC hole. With the soldering gun and solder, he will solder the wire into place, then visually inspect it for a clean and strong solder. He will repeat this step for the remaining 6 lengths of wire as follows: two wires into the center most GND holes; a wire into the center most -6 VDC hole; and the remaining 3 lengths of wire will be inserted and soldered as before into the BIT, RATE, and TEMP holes. The technician and engineer will each do a final visual

inspection of the PCB soldering to insure everything is done to standard, and then set the PCB to the side.

T _____
Engineer_____

3-6 The technician will set up a calibrated power supply to feed each PCB +6 VDC, -6 VDC, and a common GND. Using the table below, he will conduct a full electrical check of the PCBs much like step 3-1, recording all results in the table. With a calibrated multi-meter and power supply, he will first verify that each PCB is correctly step-down filtering the power from +/- 6 V to +/- 5 V (Pin 3 and Pin 9). Next, he will ground the BIT (Pin 5), Rate (Pin 7), and Temp (Pin 6) in turn, and verify that the output leads of each show 0V. Next, he will supply each of the 3 MEMS Rate holes (Pin 7) with 2.5 V, and insure that the output from the each RATE wire is 2.5 V. Next, he will supply each of the 3 MEMS BIT holes (Pin 5) with 2.5 V, and insure that the output from each BIT wire is 2.5 V. Finally, he will supply each of the 3 MEMS Temp holes (Pin 6) with 0.2 V, and insure that the output from each TEMP wire is about 2.6 V, depending on the exact Gain factor from the QRS-11 Board Build Data Sheet.

Test	Input	-X	Y	-Z	P/F
Voltage Step Down Test: 6.00 V to 5.00 V					
Voltage Step Down Test: -6.00V to -5.00 V					
BIT GND Test (0 V Nominal)	N/A				
Rate GND Test (0 V Nominal)	N/A				
Temp GND Test (0 V Nominal)	N/A				
Rate Output Test: 2.5 V to 2.5 V					
BIT Output Test: 2.5 V to 2.5 V					
Temp Output Test: 0.2 V to 2.6 V					

Table 1: PCB Build Verification Test Record

T _____
Engineer_____

3-7 The technician will now take each PCB and file down any long or large solder spots on the back side, making them as flush as possible while maintaining a solid solder. He will then place strips of capton tape over the open holes on the top side of each of the 3 PCBs, as well as a 10-Pin MEMS connection port, to insure that no conformal coating will get into any of the open holes. The technician will then place the three PCBs face up on a clean stick free surface. With a brush, he will lightly coat the top of each PCB with conformal coating, insuring an even coating on each PCB. He will set these aside slightly raised to allow any excess material to run off, and allow them to air dry for 24 hrs.

T _____
Engineer_____

3-8 The technician will inspect each PCB to insure the conformal coating has had enough time to adequately dry. If so, he will take an Exacto Knife and carefully score around the embedded capton tape. He will then gently remove the capton tape covers, and clean up any excess conformal coating material around these boarders. The technician will then place the three PCBs face down on a clean stick free surface. With a brush, he will lightly coat the back of each PCB spacer with conformal coating, insuring an even coating on each PCB spacer. Using the reference diagram below, he will then apply the PCB spacers to the back of each PCB in the location shown in the diagram below, using the conformal coating as an adhesive to secure the spacer in place. He will set these aside and allow them to air dry for 24 hrs.

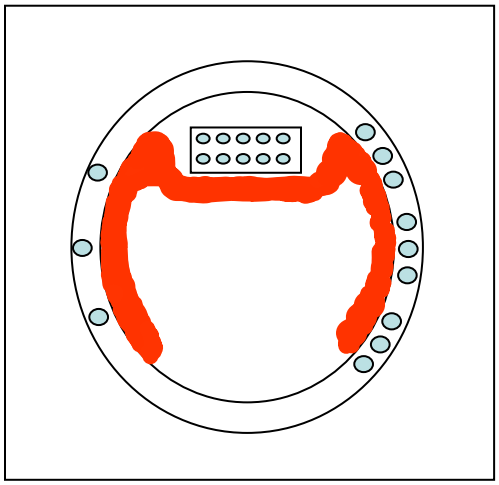

Figure 4: PCB Spacer Diagram

T _____
Engineer_____

3-9 The technician will inspect each PCB to insure the conformal coating has had enough time to adequately dry. If so, he will clean up any excess conformal coating material around these boarders. The engineer will inspect all 3 PCBs to insure that they are clean, properly constructed, and ready for the next step of assembly.

T _____
Engineer_____

ITEM 4 PCB MOUNTING AND CONNECTION

Reference drawings for Item 4 are the 13-Pin connector Diagram, the ACS wiring diagram, the QRS11 Users Guide, the QRS11 PCB Schematic, the QRS11 PCB Diagram, and the MEMS Wiring Diagram.

4-1 The technician will place the MEMS assembly on the work table in front of him, with the –X face up. With a brush, he will then apply a 5mm dab of RTV to the back center of the –X PCB, as shown in the below diagram. Carefully, he will align the –X PCB over the –X QRS-11 sensor, then gently press the PCB down into position, insuring to press down evenly until the PCB is mounted flush on the QRS-11. He will then visually verify that the PCB is securely mounted and centered on the QRS-11, and that all 10 Pins are properly aligned.

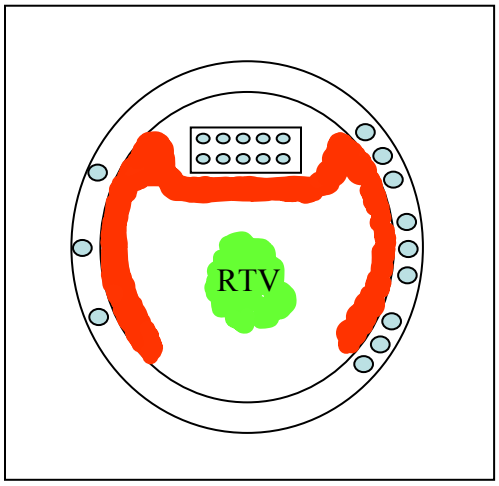

Figure 5: PCB RTV Diagram

T _____
Engineer_____

4-2 The technician will insure that the soldering gun is ready, properly set to 700˚F, and that the solder and damp sponge are easily reachable. He will then carefully solder all 10 pins of the –X QRS-11 sensor to the 10-Pin connector of the –X PCB. The technician will visually inspect the solders with a magnifying glass, insuring strong solders and good electrical connectivity. He will repair solders as needed, and clean the PCB when complete, insuring that no FOD is present. The engineer will inspect the work, and set it to the side when complete.

T _____
Engineer_____

4-3 The technician will repeat steps 4-1 through 4-2 for the remaining two sensors and PCBs (Y and –Z). He will then set the MEMS assembly aside for 24hrs, allowing the RTV to properly set.

T _____

Engineer_____

4-4 The technician will set the MEMS assembly on the work table in front of him, base plate down. He will insure that the soldering gun is ready, properly set to 700˚F, and that the solder and damp sponge are easily reachable. He will now take the –X +6 VDC wire, and run it into the centermost +6 VDC hole of the –Z sensor, trimming any excess wire and stripping it for insertion into the next board. With the soldering gun and solder, he will solder the wire into place, then visually inspect it for a clean and strong solder. Next, he will take the free +6 VDC wire of the –Z sensor, and run it into the center most +6 VDC hole of the Y sensor, trimming and stripping the wire as before. With the soldering gun and solder, he will solder the wire into place, then visually inspect it for a clean and strong solder. *Note: This will leave a single +6 VDC wire (Y PCB) for connection to the 13-Pin connector.*

T _____
Engineer_____

4-5 The technician will now take the –X -6 VDC wire, and run it into the centermost -6 VDC hole of the –Z sensor, trimming any excess wire and stripping it for insertion into the next board. With the soldering gun and solder, he will solder the wire into place, then visually inspect it for a clean and strong solder. Next, he will take the free -6 VDC wire of the –Z sensor, and run it into the center most -6 VDC hole of the Y sensor, trimming and stripping the wire as before. With the soldering gun and solder, he will solder the wire into place, then visually inspect it for a clean and strong solder. *Note: This will leave a single -6 VDC wire (Y PCB) for connection to the 13-Pin connector.*

T _____
Engineer_____

4-6 The technician will take the MEMS assembly, and place it flat on the table in front of him, with the Y face pointing away from him. Next, he will take the 13-Pin connector and secure it in a table clamp, just above the center of the MEMS assembly. He will rotate the clamp such that the 13-Pin connector is oriented 90deg with reference to the MEMS assembly as it would be in flight. He will insure that the soldering gun is ready, properly set to 700˚F, and that the solder and damp sponge are easily reachable.

T _____
Engineer_____

4-7 The technician will take the first of the two GND wires from each PCB, and bring them together as close as possible to the top center of the MEMS assembly. He will then trim the excess wire, and strip these three wires. With a solder gun, he will solder these three GND wires together. Using one of the clipped wires, he will measure out the distance from the 3 wire solder to the solder cup of its corresponding pin on the 13-Pin connector (Pin 10) as seen in the figure below. He will then trim this wire, and solder it to the 3 wire solder. Finally, he will

solder the single wire lead to the solder cup of Pin 10. Note: A serving sleeve may be used to accomplish the same thing if there is room to work with and if no components will be put at risk from the high temperatures of the heat gun. He will then visually inspect the pin 10 solders for clean and strong solders, insuring that no material touches or comes close to adjacent pins.

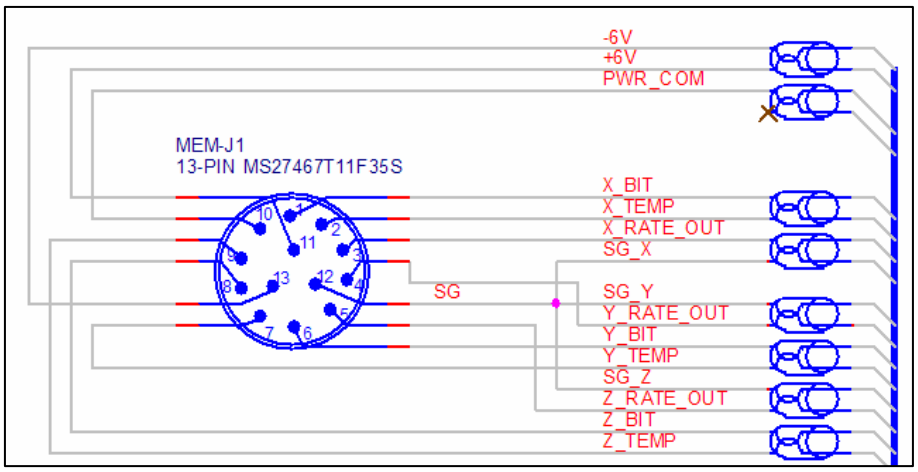

Figure 6: 13-Pin Connector

T _____
Engineer_____

4-8 With the soldering gun and solder, the technician will repeat step 4-8 for the remaining free GND wires from each of the three PCBs. He will solder the single wire lead into the solder cup of its corresponding pin (SG) on the 13-Pin connector (Pin 12) as seen in the above figure. He will then visually inspect the pin 12 solders for clean and strong solders, insuring that no material touches or comes close to adjacent pins.

T _____
Engineer_____

4-9 With the soldering gun and solder, the technician will now solder the remaining 11 single wires to there respective 13-Pin connector solder cups in the following order, insuring to visually inspect each solder before moving to the next:

- The free +6 VDC wire (Y PCB) to Pin 11
- The free -6 VDC wire (Y PCB) to Pin 13
- The Y BIT wire to Pin 6
- The Y Temp wire to Pin 7
- The –Z Temp wire to Pin 9
- The –Z BIT wire to Pin 8
- The -Z Rate Out wire to Pin 5
- The Y Rate Out wire to Pin 4

- The –X Rate Out wire to Pin 3
- The –X Temp wire to Pin 2
- The –X BIT wire to Pin 1

T _____
Engineer_____

4-10 The technician will do a final visual inspection of the 13-Pin connector solders, as well as the PCB solders. He will insure that no unwanted contacts or circuit shorts are present, and that no sharp solder edges are present, removing the potential for wire wear. He will visually inspect the cleanliness of the MEMS assembly, and use canned air to remove any FOD. Using a mulitimeter, he will verify connectivity between the PCB solder points and the outside pins of the 13-Pin connector.

T _____
Engineer_____

ITEM 5 MEMS HOUSING BUILD

Reference drawings for Item 5 are the MEMS Housing Base Plate Schematic, the MEMS Housing Schematic, and the 13-Pin connector Diagram.

5-1 The technician will start by removing the 13-Pin connector from the clamp that has been supporting it next to the MEMS assembly. He will now insure that the housing cover O ring is firmly in place on the cover. *Note: A small amount of adhesive may be necessary to insure the O ring stays in position while lowering the* cover. He will then carefully lower the MEMS housing down over the MEMS assembly, insuring not to crimp any wires or damage any of the PCBs. He will insure the 13-Pin connector is properly aligned with its access hole in the housing cover, and then lower the housing cover down until flush with the base plate, insuring the O ring is seated properly. He will slowly rotate the cover until the 10 housing mounting holes are aligned. He will then place a small amount of thread tight compound on the lower end of each of the 10 housing screws. He will then insert and loosely thread them and the washers until almost flush. With a torque wrench, he will then alternately tighten each screw to a torque value of 1.7 in-lbs in a criss-crossing pattern.

T _____
Engineer_____

5-2 The technician will begin by applying a small band of thread tight to the lower threads of the 13-Pin connector. Then, with his free hand, the technician will hold the 13-Pin connector tight in position in the housing cover. He will then insert the 0.0255" connector shim into the small void between the flat edge of the 13-Pin connector, and the flat edge of the MEMS housing cover access hole. Continuing to hold the connector in place, he will then insert the 13-Pin connector locking nut onto the 13-Pin connector. He will thread the nut down until it is flush with the top surface of the MEMS housing cover. With a Torque wrench, he will tighten the nut to a torque value of 1.4 in-lbs.

T _____
Engineer_____

5-3 The technician will wrap the two MEMS purge plugs with 3 layers of Teflon tape. He will then insert the nitrogen feed tube into one of the MEMS housing cover purge ports. He will turn on the nitrogen, purging the inside of the MEMS for 2 minuets. Continuing to feed nitrogen into the MEMS, he will insert the first MEMS purge plug into the open purge port. He will tighten the plug down into the housing cover until flush with the purge port surface. He will then remove the nitrogen feed tube, and quickly insert the second MEMS purge plug as he did the first.

T _____
Engineer_____

5-4 The technician will inspect the MEMS Flight Subsystem, insuring that all seals are tight, and that nothing "Rattles" when shaken. He will then place the 13-Pin connector cover over the connector to protect it from FOD.

T _____

Engineer_____

ITEM 6 TESTING AND VERIFICATION

Reference drawings for Item 6 are the NPSAT1 ACS wiring diagram, MEMs connector diagram, 13-Pin connector Diagram, and 15-Pin connector diagram.

6-1 The technician will mount the MEMS subsystem to the two-axis rotation table, insuring to align the sensor sense axis (curved edge) to the alignment markings of the rotation table. He will then connect the 13-Pin side of the flight wiring harness to the MEMS subsystem, insuring that the connector is firmly seated and locked. He will then connect the 15-Pin side of the flight harness to the testing bracket of the work bench (with flight test connector attached). Using a calibrated mulitimeter, the technician will verify that the power supply is set to +/- 6.00 VDC. He will then power off the power supply, and attach the +6 V, -6 V, and COMM GND leads to the respective test connector leads as seen in the figure below. He will then set the WEBDAQ test interface box next to the power supply. With it powered off, he will attach the remaining 12 leads (red) to the WEBDAQ wire ports as seen below. He will then attach the jumpers (blue).

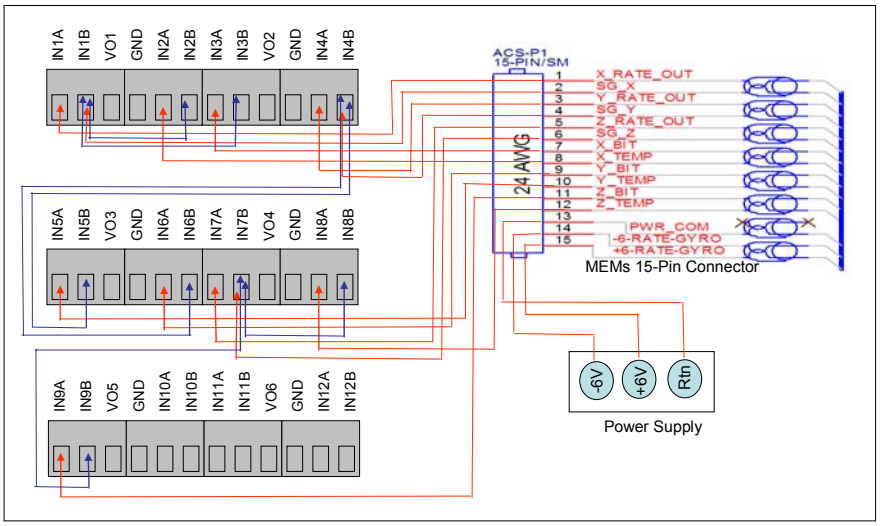

Figure 7: WebDAQ Wiring Diagram (Harness)

T _____
Engineer_____

6-2 The technician will power on the WEBDAQ, and load the WEBDAQ website, insuring connectivity. He will then set the WEBDAQ to display results every second, and to sample at 200 Hz (200 samples averaged every sec). He will verify that the channel settings match the ports shown in the figure above. If they do not, he will make these updates, and make the same changes to the python interface program. *Note: Failure to do this will result in results being displayed in the wrong order, location, or not at all.*

T _____
Engineer_____

6-3 The technician will set up a python acquisition program to acquire, display, and save data every 1 second for 3 min. He will start the program, after 30 sec he will turn on the power supply, and observe the results. The technician should observe the BIT values for all 3 sensors jump from below 0.8 V (logical 0) to above 2.4 V (logical 1), typically around 4.2 V. Also, he should observe a power up spike in Rate and Temp outputs for the first few seconds, then leveling off between 25 to 40 mV of noise for each sensor. At the end of the test he will record the results in the table below. He will power off the power supply, wait 1 min, then repeat this test 2 more times, recording the results below. The technician will compare the results, and verify that there results match what is known of the sensor performance characteristics from previous testing.

Observation/Results (X/Y/Z)	Test 1	Test 2	Test 3
Was the first 30 sec typical?	/ /	/ /	/ /
BIT prior to powering on?	/ /	/ /	/ /
Rate prior to powering on?	/ /	/ /	/ /
Temp prior to powering on?	/ /	/ /	/ /
BIT at the end of test?	/ /	/ /	/ /
Rate at test end?	/ /	/ /	/ /
Temp at test end?	/ /	/ /	/ /
How long for BIT transition?	/ /	/ /	/ /
Was Rate start up normal?	/ /	/ /	/ /
Exceptions (Notes):			

Table 2: MEMS Start Up and Operations Test Record

T _____

Engineer_____

6-4 The technician will now attach the Agilent scope and low noise probes to the 3 rate output leads. He will power on the MEMS, and allow it to warm up for 5 min. He will insure to unplug the power to the WEBDAQ, leaving the power on will induce large noise spikes into the agilent rate data. He will set the scope to a sampling rate of 5 Ksamples/sec, or about 18 sec of data, then start an acquisition cycle. Once the test is complete, he will save the Rate data and corresponding FFT for each sensor, and print them off for comparison. He will conduct this test 2 more times. Once complete, the technician will compare the results for all 3 tests for each sensor to insure consistency. He will then compare the results of each sensor. Both graphs should look similar to the figures below. He will note any discrepancies in the space provided below.

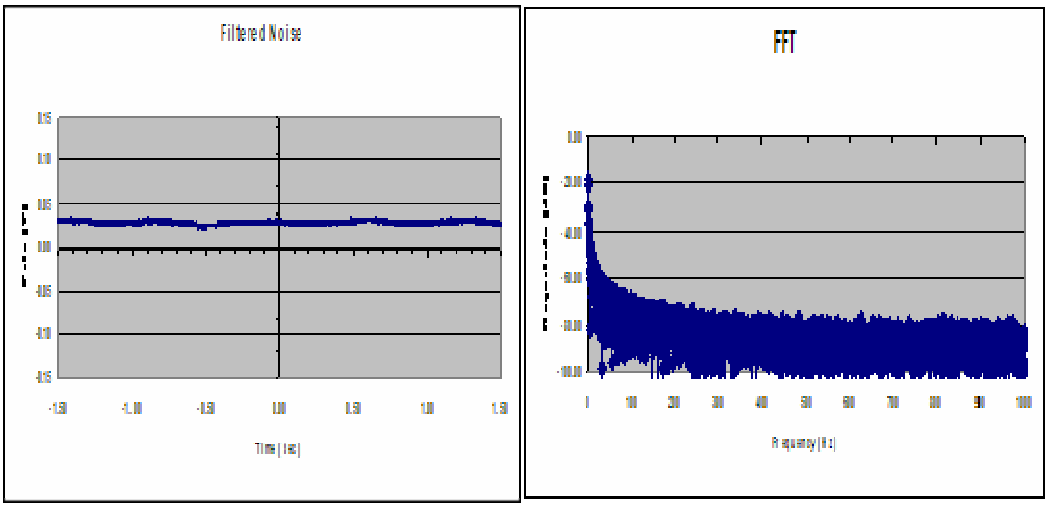

Figure 8: Nominal Rate Noise / FFT

Discrepancies (Notes):

T _____
Engineer_____

6-5 The technician will set the python acquisition program to acquire, display, and save data every 1 second for 1 min, at 1000Hz. He will turn on the HAAS 2-Axis Rotational Table, and program it in preparation for the next test using the following procedures:

1	Power on the HAAS 2-Axis Rotation Table.
2	Press the start button 1 time.
3	Insure proper table alignment, then press and hold the CLR button for 3 sec.
4	Press the right arrow button, then press and hold the CLR button for 3 sec.
5	Press the mode button, verify or enter 91, then press the right arrow button.
6	Enter the tilt angle, and then press the right arrow.
7	Enter the rotation angle, and then press the right arrow.
8	Enter the rate, and then press the right arrow.
9	Press the mode button to finish the program.

Table 3: HAAS Controller Setup Procedures

T _____
Engineer_____

6-6 The technician will verify the –Z axis. From the table below, the technician will enter the first program using the steps 5-9 from the procedures from Figure 4. Once ready, he will start the python acquisition program, and then quickly start the HAAS program. He will repeat the controller programming procedures (step 5-9) for each of the 10 rates, recording the results in the table below. Results should be the average voltage output from each of the 3 Rate axis sensors over the 60 sec of testing. The technician will compare the results to the expected values, and make note of any irregularities in the provided notes block.

Tilt (deg)	Rot (deg)	Rate (deg/s)	-Z (V)	Y (V)	-X (V)
0	250	5.0	/ 2.5	/ 0	/ 0
0	-250	5.0	/ -2.5	/ 0	/ 0
0	125	2.5	/ 1.25	/ 0	/ 0
0	-125	2.5	/ -1.25	/ 0	/ 0
0	50	1.0	/ 0.5	/ 0	/ 0
0	-50	1.0	/ -0.5	/ 0	/ 0
0	25	0.5	/ 0.25	/ 0	/ 0
0	-25	0.5	/ -0.25	/ 0	/ 0
0	5	0.1	/ 0.05	/ 0	/ 0
0	-5	0.1	/ -0.05	/ 0	/ 0
Notes:					

Table 4: -Z Axis Sensor Verification Record

T _____

Engineer_____

6-7 The technician will now repeat the previous test for the Y axis sensor. Before beginning, he will first need to re-align the rotational table to put the Y sense axis in plane with the rotational table. From the start position, the technician will rotate the rotational table 90 deg, and the tilt table -80 deg. This will put the tilt axis in the same plane as the Y sensor axis, as well as maximize the amount of travel angle available to the tilt axis. This is the new start position. *Note: The tilt axis of the table is limited to +/- 80 deg, thus a full minute of data will not be possible for the higher rate tests, and data will need to be adjusted before averaging.* Once this is complete, the technician will continue as before, using both figure 4 from above, as well as the table below. Once ready, he will start the python acquisition program, and then quickly start the HAAS program. He will repeat the controller programming procedures (step 5-9) for each of the 10 rates, recording the results in the table below. Results should be the average voltage output from each of the 3 Rate axis sensors. The technician will compare the results to the expected values, and make note of any irregularities in the provided notes block.

Tilt (deg)	Rot (deg)	Rate (deg/s)	-Z (V)	Y (V)	-X (V)
160	0	5.0	/ 0	/ 2.5	/ 0
-160	0	5.0	/ 0	/ -2.5	/ 0
125	0	2.5	/ 0	/ 1.25	/ 0
-125	0	2.5	/ 0	/ -1.25	/ 0
50	0	1.0	/ 0	/ 0.5	/ 0
-50	0	1.0	/ 0	/ -0.5	/ 0
25	0	0.5	/ 0	/ 0.25	/ 0
-25	0	0.5	/ 0	/ -0.25	/ 0
5	0	0.1	/ 0	/ 0.05	/ 0
-5	0	0.1	/ 0	/ -0.05	/ 0
Notes:					

Table 5: Y Axis Sensor Verification Record

T _____
Engineer_____

6-8 The technician will now repeat the previous test for the -X axis sensor. Before beginning, he will first need to re-align the rotational table to put the X sense axis in plane with the rotational table. From the current start position, the technician will rotate the rotational table another 90 deg. This will put the tilt axis in the same plane as the -X sensor axis, as well as maximize the amount of travel angle available to the tilt axis. This is the new start position. *Note: The tilt axis of the table is limited to +/- 80 deg, thus a full minute of data will not be possible for the higher rate tests, and data will need to be adjusted before averaging.* Once this is complete, the technician will continue as before, using both figure 4 from above, as well as the table below. Once ready, he will start the python acquisition program, and then quickly start the HAAS program. He will repeat the controller programming procedures (step 5-9) for each of the 10 rates, recording the results in the table below. Results should be the average voltage output from each of the 3 Rate axis sensors. The technician will compare the results to the expected values, and make note of any irregularities in the provided notes block.

Tilt (deg)	Rot (deg)	Rate (deg/s)	-Z (V)	Y (V)	-X (V)
160	0	5.0	/ 0	/ 0	/ 2.5
-160	0	5.0	/ 0	/ 0	/ -2.5
125	0	2.5	/ 0	/ 0	/ 1.25
-125	0	2.5	/ 0	/ 0	/ -1.25
50	0	1.0	/ 0	/ 0	/ 0.5
-50	0	1.0	/ 0	/ 0	/ -0.5
25	0	0.5	/ 0	/ 0	/ 0.25
-25	0	0.5	/ 0	/ 0	/ -0.25
5	0	0.1	/ 0	/ 0	/ 0.05
-5	0	0.1	/ 0	/ 0	/ -0.05
Notes:					

Table 6: -X Axis Sensor Verification Record

T _____
Engineer_____

7 TASK COMPLETION REVIEW

7.1 ENGINEER REVIEW OF PROCEDURE TASK COMPLETION

The signature below indicates that the undersigned engineer has reviewed the completed work copy of this procedure, and the hardware affected, and is satisfied that the work is correct and complete.

Engineer Signature Date

Engineer Printed Name

7.2 DOCUMENT CONTROL REVIEW OF PROCEDURE COMPLETION

The signature below indicates that the undersigned document control representative has reviewed the completed work copy of this procedure, is satisfied that the document is complete, and will store this document in the document control center.

Document Control Representative Date

Document Control Representative Printed Name

APPENDIX C

PYTHON CODE

```
import string
import sys
import time
import WebDAQ

last_read = -1

def mems_read():
        global last_read
        now = time.time()
        s = WebDAQ.read("MEMS2", "MEMS_Interval")
        webdaq_s = s

        if (s == -1):
                print "Error reading from WebDAQ"
                return ()

        try:
                s = string.split(s, "\n")[1]
        except:
                print "Error reading from WebDAQ"
                return ()

        try:
                ss = string.split(s, ",")[0:9]
        except:
                print "Error reading from WebDAQ"
                print "WebDAQ.read() = <%s>" %(webdaq_s)
                return ()

        last_read = now
        return (now, float(ss[0]), float(ss[1]), float(ss[2]), float(ss[3]),
                float(ss[4]), float(ss[5]), float(ss[6]), float(ss[7]), float(ss[8]))
```

```
def mems_read_interval(delta_time = 2.0):
        global last_read
        if (last_read != -1):
                while ((time.time() - last_read) < delta_time):
                        time.sleep(0.05)

        return mems_read()

def save_data(filename, data):
        try:
                fp = open(filename, "a")
                fp.write("%1.2f, " %(data[0]))
                print "%1.2f," %(data[0]),
                for d in data[1:]:
                        fp.write("%1.4f, " %(d))
                        print "%1.4f, " %(d),
                fp.write("\n")
                print
                fp.close()
        except:
                try:
                        fp.close()
                except:
                        pass

if __name__ == "__main__":
        if (len(sys.argv) != 4):
                print "mems_data.py <output filename> <save interval [secs]> <duration [mins]>"
                sys.exit()

        outfile = sys.argv[1]
        interval = float(sys.argv[2])
        duration = float(sys.argv[3])

        if (WebDAQ.open("172.20.72.43", 0) == -1):
                print "Cannot open WebDAQ"
                sys.exit()

        start_time = time.time()

        while (time.time() - start_time < duration*60):
                data = mems_read_interval(interval)
                save_data(outfile, data)

        WebDAQ.close()
```

INITIAL DISTRIBUTION LIST

1. Defense Technical Information Center
   Ft. Belvoir, VA

2. Dudley Knox Library
   Naval Postgraduate School
   Monterey, CA

3. Mr. Daniel J. Sakoda
   Code SP/SD
   Naval Postgraduate School
   Monterey, CA

4. Dr. Jim Newman
   Code SP/SD
   Naval Postgraduate School
   Monterey, CA

5. MAJ Thomas S. Pugsley
   Monterey, CA

6. Ron Phelps
   Code SP/SD
   Naval Postgraduate School
   Monterey, CA